DEVELOPMENT OF A FATIGUE-COMPATIBLE COHESIVE ZONE METHOD FOR A COPPER-EPOXY MOLDING COMPOUND BIMATERIAL INTERFACE

A Dissertation
Presented to
The Academic Faculty

by

David Steven Samet

In Partial Fulfillment
of the Requirements for the Degree
Doctor of Philosophy in the
George W. Woodruff School of Mechanical Engineering

Georgia Institute of Technology
August 2018

COPYRIGHT © 2018 BY DAVID STEVEN SAMET

DEVELOPMENT OF A FATIGUE-COMPATIBLE COHESIVE ZONE METHOD FOR A COPPER-EPOXY MOLDING COMPOUND BIMATERIAL INTERFACE

Approved by:

Dr. Suresh K. Sitaraman, Advisor
School of Mechanical Engineering
Georgia Institute of Technology

Dr. C. P. Wong
School of Materials Science and Engineering
Georgia Institute of Technology

Dr. Samuel Graham
School of Mechanical Engineering
Georgia Institute of Technology

Dr. Jianmin Qu
School of Engineering
Tufts University

Dr. Olivier Pierron
School of Mechanical Engineering
Georgia Institute of Technology

Date Approved: July 18, 2018

For Veronica

ACKNOWLEDGEMENTS

First, I would like to thank my advisor, Dr. Suresh Sitaraman for his advice and mentorship during my studies. Beyond his intellectual guidance he has benefitted me with tireless backing and support through significant life challenges. I would like to express my immense appreciation to him for his caring through these times.

I thank Dr. Samuel Graham, Dr. Olivier Pierron, Dr. C.P. Wong and Dr. Jianmin Qu for serving on my committee. Their insight was invaluable towards the quality of my work. Additionally I would like to thank Dr. Graham for access to his lab and use of equipment in support of this work.

I would like to thank both the Semiconductor Research Corporation and NXP for their financial support toward this research. In particular, Torsten Hauck, Ilko Schmadlak, Nishant Lakera, and Sandeep Shantaram have all contributed to the overall qualkity of the thesis as industrial liasons. Without their support this research would not have existed.

I thank all of my labmates for their insight, especially Scott McCann, Christine Taylor, Justin Chow, Trilochan Rambhatla, Casey Woodrum, and Abhishek Kwatra. Innumerable conversations and debates have been both enjoyable and essential in helping me navigate my studies.

I would very much like to thank my parents Dr. Laurence Samet and Mrs. Deborah Samet for their love, support, and relentless confidence in me throughout my life.

Most importantly I would like to thank my fiancée Dr. Veronica Novosad. I cannot fully describe the depth of my appreciation for having her as my partner and co-pilot throughout life.

TABLE OF CONTENTS

LIST OF TABLES

LIST OF FIGURES

LIST OF SYMBOLS AND ABBREVIATIONS

Nomenclature	
a	Crack length (mm)
α	Displacement Jump Ratio (δ^*/δ^c)
A_{cu}	Cross sectional area of Copper (mm^2)
A_{emc}	Cross sectional area of Epoxy Molding Compound (mm^2)
b	DCB interface specimen width (mm)
b_{cu}	Width of Copper (mm)
b_{emc}	Width of Epoxy Molding Compound (mm)
b_p	DMMB Loading Configuration Parameter
β	Non-Dimensional Shear / Normal Weighting Parameter
β_E	Modulus ratio
β_H	Thickness ratio
c	DMMB Loading Configuration Parameter
C	Paris-Erdogan Law Coefficient
C_{sys}	Compliance of the DCB specimen (mm/N)
D_m	Mixed Mode Bilinear Damage Parameter
D_n	Mode I Damage Parameter
δ	Displacement (μm)
δ_n^*	Normal Displacement Jump at Maximum Normal Cohesive Traction
δ_t^*	Shear Displacement Jump at Maximum Shear Cohesive Traction
δ_n^c	Normal Displacement Jump at Completion of Debonding
δ_t^c	Shear Displacement Jump at Completion of Debonding
δ_n^{max}	Maximum Normal Displacement Jump Attained
δ_t^{max}	Maximum Shear Displacement Jump Attained
E_i	Elastic Modulus of the i-th layer
E_{Cu}	Modulus of Elasticity of Copper (GPa)
E_{EMC}	Modulus of Elasticity of Epoxy Molding Compound (GPa)
$E_{f,cu}$	Flexural Modulus of Copper (GPa) = E_{Cu} from elasticity assumption
$E_{f,emc}$	Flexural Modulus of Epoxy Molding Compound (GPa) = E_{Cu} from elasticity assumption
E_{Lost}	Energy Lost in CZM to Propagate Crack
$E_{CZM,Element}$	Energy Required to Debond a CZM Element
$E_{Lost,Cycle}$	Energy Lost in a Loading Cycle
$E_{Before\ Cycle}$	Total Energy in Loaded CZM Elements Before a Load Cycle
$E_{After\ Cycle}$	Total Energy in Loaded CZM Elements After a Load Cycle
η	Dimensionless CZM Displacement Parameter
h_i	Thickness of the i-th layer
G	Strain Energy Release Rate (SERR) (J/m^2)
G_I	Mode I SERR
G_{IC}	Critical Mode I SERR
G_{II}	Mode II SERR
G_{IIC}	Critical Mode II SERR

G_c	Critical Strain Energy Release Rate (J/m^2)
G_R	Resistance Curve SERR (J/m^2) = Critical Value as a Function of Length
$\mu_{13,cu}$	In-plane shear modus of Copper (GPa)
$\mu_{13,emc}$	In-plane shear modus of Epoxy Molding Compound (GPa)
I_{cu}	Moment of Inertia of Copper Cantilever Beam (mm^4)
I_{emc}	Moment of Inertia of Epoxy Molding Compound Cantilever Beam (mm^4)
K_n	Normal Cohesive Stiffness (T_n^{max} / δ_n^*),
K_t	Shear Cohesive Stiffness (T_t^{max} / δ_t^*),
λ	Non-Dimensional Mixed Mode Displacement Jump
λ_{cr}	Critical Non-Dimensional Mixed Mode Displacement Jump
λ_{HS}	Hutchinson and Suo Shaping Parameter
$l_{element}$	Length of CZM Element
L	Length of the Specimen
m	Paris-Erdogan Law Exponent
N	Number of Load Cycles
P	Mode I opening load for the DCB specimen (N)
Ψ	Nodal Displacement Based Mode-Mixity
Ψ_G	SERR Based Mode-Mixity
t_{cu}	Thickness of Copper (mm)
t_{emc}	Thickness of EMC (mm)
T_n^{max}	Maximum Normal Cohesive Traction
T_t^{max}	Maximum Shear Cohesive Traction
U_e	Elastic Strain Energy
U_p	Plastic Work
U_f	Energy of Fracture
U_d	All Other Non-Conservative Energy Losses (dissipated)
$w_{element}$	Width of CZM Element
W	Applied External Work
Acronyms	
4PB	Four-Point Bend
CZM	Cohesive Zone Model
DCB	Double Cantilever Beam
EMC	Epoxy Molding Compound
FEA	Finite Element Analysis
LEFM	Linear-Elastic Fracture Mechanics
SEM	Scanning Electron Microscope
SERR	Strain Energy Release Rate
VCCT	Virtual Crack Closure Technique
XPS	X-Ray Photoelectron Spectroscopy
XFEM	Extended Finite Element Method

SUMMARY

Interfacial delamination is a prevalent failure mechanism in microelectronic packages. While much work has been performed towards understanding fracture of bimaterial interfaces under monotonic loading, investigation focused on the impact of fatigue loading on such structures is still evolving. Microelectronic packaging interfaces experience cyclic loads, and thus may eventually debond during operation. In addition to such fatigue characterization of packaging interfaces, the development of a computationally affordable modeling methodology with predictive capability towards fatigue crack propagation and failure is needed. This work focuses on copper/epoxy mold compound (EMC) interfacial delamination under fatigue loading through experiments as well as computational modeling. The performed characterization relies primarily on double cantilever beam tests but also other test configurations such as four-point bend. Finite element models for both traditional fracture mechanics and cohesive-zone modeling (CZM) have been used for interfacial fracture parameter extraction and analysis. Using fatigue interfacial fracture experiments, an innovative fatigue-compatible CZM modeling framework has been developed. The developed fatigue CZM model has been validated against other experimental data. Also, interfacial fracture failure locus is examined under the context of multiple interfacial fracture tests. Additionally, the dependency of fatigue crack propagation trends on mode-mixity is examined.

CHAPTER 1. INTRODUCTION

The microelectronics industry is governed by the same drivers as any other industry; maximizing performance while minimizing cost. For decades the dominant driver of device performance was the transistor density of the integrated circuits (ICs). Transistor density was primarily limited by the capabilities of the fabrication process, in particular, lithographic resolution. As IC miniaturization progressed however, non-uniform scaling impacts for various physics resulted in signal routing becoming a source of performance bottlenecks as device reliability could be hindered by thermal, mechanical, electrical or chemical failures. While many of the electrical requirements were satisfied with the introduction of various materials such as insulating low-k dielectrics and various metallization layer schemes, these solutions raised the threat of thermo-mechanical device failure. As a result of the ubiquitous presence of dissimilar materials in IC and microelectromechanical systems (MEMS), interfacial delamination of such bonded structures is a common failure mechanism which must be addressed.

Characterization and understanding of the failure of bimaterial interfaces is key to minimize delamination and improve device reliability. Historically, device design was conducted through a combination of lessons learned / industrial knowledge and trial and error. Reliability tests were established and subsequently followed by various manufacturers based upon their experiences. This resulted in non-uniform methodology across the field though there has been a major effort at standardization in recent years through organizations such as The International Organization for Standardization (ISO) and Joint Electron Device Engineering Council (JEDEC).

To date, the majority of metal-polymer interfacial design and testing has been either for monotonic failure or based upon simple time at temperature and/or moisture exposure survivability. Monotonic failure characterization can provide insight towards fabrication failure but survivability testing only provides qualitative insight towards failure specific towards the specific design in question rather than quantitative predictive value. Quantitative fatigue characterization, supportive towards modeling and simulation of these interfaces in finite element analysis (FEA) packages, will both provide this predictive capability and improve efficiency when designing for reliability.

This work characterizes and models bimaterial interfacial delamination under monotonic and fatigue loading conditions. To this end, a bimaterial copper/epoxy molding compound has been selected for study due to the ubiquity of metal-polymer interfaces in microelectronic package design. Samples have been tested primarily for double cantilever beam (DCB) but also four-point bend (4PB) configurations. The end goal of the fatigue characterization is in use towards predictive FEA models. Both traditional fracture mechanics models and cohesive-zone models (CZM) have been developed. CZMs have demonstrated the desired predictive capability at an affordable computational cost for monotonic interfacial fracture. Existing CZM does not incorporate fatigue effects. The result of this work establishes a fatigue-compatible CZM which can predict interfacial delamination for both monotonic and cyclic loading conditions. These additional modeling capabilities, provided at affordable computational cost, will improve design reliability methods by modeling the limiting failure phenomena.

This thesis is organized into four main chapters (3-6) containing the content of this work. Each chapter corresponds to a published or currently being published manuscript and is distinct in its premise.

Chapter 3 outlines the exploration of the interfacial failure mode-mixity dependency monotonically, both experimentally and mathematically with respect to possible failure loci. Additionally the bounds of experimentally valid mode-mixities via various test geometries are explored.

Chapter 4 outlines the development of a compliance-based experimental method for the establishment of fatigue crack propagation relationships.

Chapter 5 uses the methodology described in Chapter 4 towards samples with multiple different mode-mixites to establish any correlations. Additionally SEM studies were performed in pursuit of any relatable observations of the underlying micromechanics for different mode-mixities.

Chapter 6 describes the development of a new numerical modeling technique, the so called "Energy Decrement Method," which incorporates the fatigue laws as determined in Chapters 4-5 into an ANSYS CZM model.

Combined these four chapters establish both a novel new method of incorporating fatigue crack propagation into a traditional CZM model and the verification of the validity of the behavior of that model establishing predictive capability at affordable computational cost.

1.1 Strain Energy Release Rate

Evaluating failure in fracture mechanics requires the comparison of a loading condition to a known critical value at which fracture will occur. Stress intensity factor (SIF) approaches are the most simple but are only applicable within sets of limitations. The constraints on sample size, geometry, and constitutive behavior, make SIF approaches ill-suited towards the evaluation of interfacial delamination. For problems involving interfacial fracture, energy-based methods demonstrated greater utility.

The energy balance for systems undergoing steady state delamination is shown in Equation 1.

$$dW = dU_e + dU_p + dU_f + dU_d, \quad \textbf{1)}$$

Where W is the applied external work, U_e is the elastic strain energy, U_p is the plastic work, U_f is the energy of fracture and U_d is all other non-conservative energy losses. When linear-elastic fracture mechanics (LEFM) is applicable and a small scale yielding assumptions applies, dU_p and dU_d are negligible and the energy of fracture can be relabeled G and determined from the external loading and strain energy alone:

$$G = \frac{dU_f}{\partial A} = \frac{dW - dU_e}{\partial A} = \frac{\partial (W - U_e)}{\partial A} \quad \textbf{2)}$$

Equation 2 applies for both steady state delamination and static load conditions. In Equation 2, G is the strain energy release rate (SERR). When the available SERR exceeds some critical value G_c, the crack will grow. Additional assumptions are implicit in this derivation however, for example that of a quasi-static system [1], and the reader

should be cognizant of them even if though they are out of scope of this work. It is also important to point out that although effectively utilized as a material property, G_c is a not solely a function of the constituent materials defining the interface but of loading conditions, sample geometry and the fabrication process as well. As a result G_c is a failure criterion rather than a material property [2] and is usually represented as a failure curve as a function of mode-mixity.

Numerous techniques exist to calculate the critical SERR including analytical and numerical methods. For relatively simple geometries such as symmetric DCBs analytical forms can be accurately determined [3, 4]. Most real engineering applications however involve complex geometries requiring numerical solutions such as the virtual crack extension technique [5], the virtual crack closure technique [6], and domain integral techniques such as J-integral [7-9] for evaluation.

1.1. Cohesive-Zone Modeling

Cohesive-zone modeling is an FEA method which simulates both crack initiation and crack growth without requiring re-meshing as the crack propagates. The basis for CZM was developed by Dugdale [10] and Barenblatt [11] in the early 60's but has experienced increasing popularity with the increase in cheap computing power. Cohesive-zone models use interfacial elements governed by traction-separation relationships which simulate crack growth in an energy conservative manner. The transition of CZM elements from undamaged to fully fractured is managed by a damage parameter. When complete damage occurs, the stiffness of the CZM element is zero allowing the effective

simulation of crack growth and the creation of new surfaces without requiring model re-meshing.

The area under a traction-separation law has units of J/m^2 meaning that as a traction-separation law is traversed energy is consumed. By setting the area under the curve of the CZM traction separation relationship to the critical SERR, delamination is simulated in an energy-equivalent manner. With appropriate meshing this energy equivalency is only ensured from a global perspective however. For example, the load-displacement curves of experimental data should match those predicted by the model. For CZM, the stress/strain behavior from a local perspective will not be the same as that in reality or predicted by traditional LEFM theory of models. This is by design as CZMs alleviate the stress singularity which exists at the crack tip, distributing the energy across a wider area and allowing the simulation of delamination in an energy equivalent, and computationally affordable way. As a result, proper design and implementation of CZMs is a compromise between the utility of a simplified model, and the accurate matching of expected stress fields. For this reason CZM should not be used in place of traditional LEFM analyses but in conjunction with them. A schematic representation of the process zone of a CZM model, and the bilinear traction-separation relationship, is shown in Figure 1.

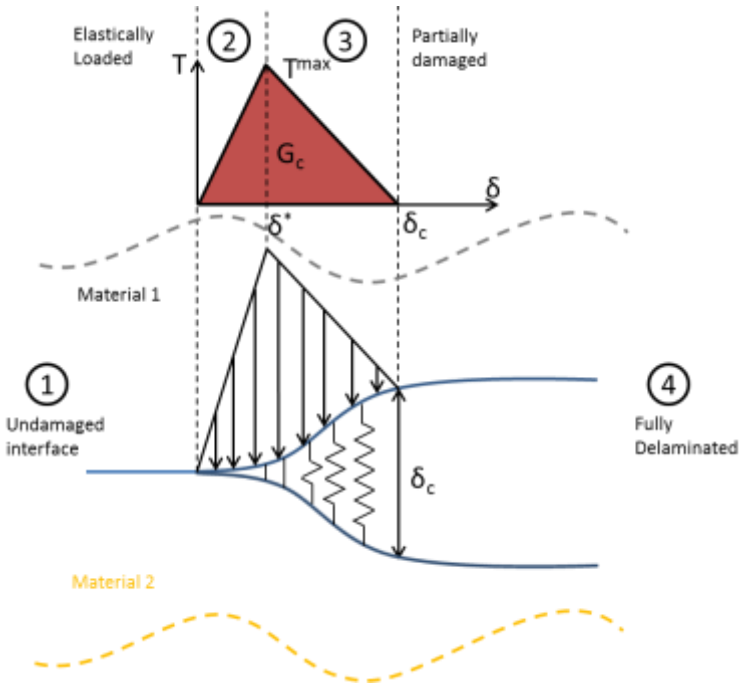

Figure 1 - CohesiveZone Modeling

1.1.1 Traction Separation Laws

Numerous forms of traction-separation relationships have been established such as exponential [12], bilinear [13, 14], trilinear [15] and trapezoidal [16] laws. As is typical in the study of mechanics analyses employ simplifying assumptions to facilitate the analysis while taking care not to incur significant error in the process. While the various traction-separation laws are derived from mathematical foundations, or constructed with the intent to replicate observed behaviors, they do not directly model the underlying physics at the micro/nano scale and should only be used within the scope for which they have demonstrated agreement with data. Various relationships, rather than a single uniform shape exist, as different interfaces do not act the same and a brittle interface for example may be better represented by a different law than a ductile one.

Mesh-traction-separation relationship agreement notwithstanding, as long as energy equivalency is maintained any law can be used though practically the relationships have preferable applications. The formulation presented by Alfano and Crisfield [14] has demonstrated good utility for the delamination of laminated composites and will be used in this work.

1.1.2 Bilinear CZ Model

This work utilizes the bilinear traction-separation law proposed by Alfano and Crisfield [14]. The bilinear law is capable of simulating mixed-mode interfacial delamination in the Mode I (normal dominated) Mode II (in-plane shear dominated) plane. In actuality most interfaces are subjected to mixed-mode loading conditions. As a result, tests at multiple mode-mixities are required to establish a G_c to mode-mixity relationship which can be implemented at any mode-mixity.

1.1.3 Mode I Damage Model

$$dT_n = K_n \delta_n (1 - D_n) \quad \textbf{3)}$$

$$D_n = \begin{cases} 0 & , \quad \delta_n^{max} \leq \delta_n^* \\ \left(\frac{\delta_n^{max} - \delta_n^*}{\delta_n^{max}}\right)\left(\frac{\delta_n^c}{\delta_n^c - \delta_n^*}\right) & , \quad \delta_n^* \leq \delta_n^{max} \leq \delta_n^c \\ 1 & , \quad \delta_n^{max} \geq \delta_n^c \end{cases} \quad \textbf{4)}$$

where K_n is the normal cohesive stiffness (T_n^{max} / δ_n^*), T_n^{max} is the maximum normal cohesive traction, δ_n^* is the normal displacement jump at maximum normal cohesive traction, δ_n^c is the normal displacement jump at completion of debonding. δ_n^{max} is the maximum normal displacement jump attained during the deformation history. For in-

plane shear dominated fracture, Mode II damage can be similarly obtained by substituting 'n' for 't' in the subscripts of the above equations.

1.1.4 Mixed Mode Damage Model

Under mixed-mode loading conditions both Mode I and Mode II contribute towards delamination. A non-dimensional mixed-mode displacement jump λ can be defined below:

$$\lambda = \sqrt{\left(\frac{\delta_n}{\delta_n^c}\right)^2 + \beta^2\left(\frac{\delta_t}{\delta_t^c}\right)^2} \quad \textbf{5)}$$

$$T_n = K_n\delta_n(1 - D_m) \quad \textbf{6)}$$

$$T_t = K_t\delta_t(1 - D_m) \quad \textbf{7)}$$

The mixed mode bilinear damage parameter D_m is defined as,

$$D_m = \begin{cases} 0 & \lambda^{max} \leq \lambda_{cr} \\ \min(1, d_m) & \lambda^{max} > \lambda_{cr} \end{cases} \quad \textbf{8)}$$

where,

$$\lambda_{cr} = \frac{\delta_n^*}{\delta_n^c} = \beta\left(\frac{\delta_t^*}{\delta_t^c}\right) \quad \textbf{9)}$$

$$d_m = \eta\left(\frac{\lambda - \lambda_{cr}}{\lambda}\right) \quad \textbf{10)}$$

$$\eta = \sqrt{\left(\frac{\delta_n^c}{\delta_n^c - \delta_n^*}\right)^2 + \beta^2\left(\frac{\delta_t^c}{\delta_t^c - \delta_t^*}\right)^2} \quad \textbf{11)}$$

Similarly to single mode debonding, when D_m reaches 1 the interface is fully damaged and the crack has propagated.

1.1. Fatigue-Induced Fracture

1.1.1. Fatigue Crack Growth

Strain energy release rate and cohesive-zone modeling can be used towards the evaluation and simulation of interfacial fracture for monotonic loading. Study of monotonic load conditions, such as the thermomechanical loads incurred during the device fabrication process, can be used to ensure the successful manufacturing of these devices. The actual reliability of such fielded devices however is often limited by the performance under fatigue conditions. While originally observed for metal fatigue, Paris-Erdogan relationships have shown good empirical matching for metal-polymer interfaces as well [17, 18]. For fatigue crack growth the Paris-Erdogan law can be represented as follows,

$$D_m = \begin{cases} 0 & \lambda^{max} \leq \lambda_{cr} \\ \min(1, d_m) & \lambda^{max} > \lambda_{cr} \end{cases} \quad \textbf{12)}$$

Where a is the crack length, N is the number of cycles, ΔG is the SERR loading amplitude, and C and m are constants.

1.1.1. Cohesive-Zone Modeling For Cyclic Loading

The standard CZM formulation is unable to predict crack propagation for fatigue conditions. As a result, a method is needed to incorporate fatigue mechanics into CZM to model fatigue crack propagation. Previous efforts from de Moura and Goncalves [19, 20] and Roe and Siegmund [21] utilize a modified damage parameter based on a known Paris-Erdogan relationship, or another damage mechanism such as void nucleation [22].

All of these existing methods also have notable downsides. The damage parameter has a high degree of mathematical abstraction as it cannot be directly related to any underlying physic. High quality CZM models have simply been shown to be consistent with the empirical observations and well behaved within the demonstrated scope of applicability. Any expansion out of the established monotonic realm must be validated and higher degrees of mathematical abstraction reduce the confidence of any validation. Additionally, as the damage parameter has no physical meaning, the choice of CZM traction-separation law will interact with the accuracy of the modified damage parameter. Finally fatigue is one of a variety of possible phenomena which might be desirable to add to the CZM framework. Reducing the degree of mathematical abstraction would increase the flexibility of the CZM framework and enable the potential incorporation of other such mechanisms. The creation and demonstration of such a theoretical framework, at acceptable computational cost, is one of the main interests of this work.

CHAPTER 2. OBJECTIVES

Interfacial delamination of bimaterial interfaces is a prominent failure mechanism for microelectronic packages. Existing literature however, has not sufficiently explored the impact of mixed-mode loading on interfacial fracture, particularly under fatigue for bimaterial interfaces. Once characterized, the behavior of mixed-mode interfacial fracture must also be incorporated into design tools to provide utility towards design reliability. This work seeks to address these needs through four main objectives.

1. To study interfacial fracture under monotonic loading conditions using a wide range of experimental techniques and associated numerical and analytical models, and to develop a failure locus that is consistent with available cohesive-zone models.
2. To study interfacial crack propagation under fatigue cycling for a given mode-mixity condition.
3. To study interfacial fracture under fatigue loading conditions and to develop a model for interfacial crack propagation under fatigue loading conditions at different mode-mixities.
4. To develop a modified cohesive-zone model to address interfacial fracture under fatigue loading conditions.

Approach for Objective 1

1. Conduct DCB and 4PB, and variations on them, with different sample dimensions.

2. Determine G_C for these testing variations using analytical models and numerical models. Energy allocation such as that for plastic work will also be accounted for.
3. Determine mode-mixity values for the conducted experiments and identify how displacement-based vs. energy-based approaches differ in mode-mixity computations.
4. Explore possible failure criteria existing in both the GI/GII plane and the Gc/mode-mixity plane. Derive mathematical conversions between the different curves where possible. Compare the accuracy and quality of the fit to experimental data for both a Hutchinson and Suo style relationship and an elliptical failure criterion.

The above items are discussed in detail in Chapter 3.

Approach for Objective 2

1. Perform fatigue-loading experiments and determine interfacial crack growth as a function of applied loading parameters
2. Employ compliance changes to determine how crack length changes with load cycling.
3. Derive Paris law relationships from the crack propagation and ΔG data. Normalize the Paris law data by the critical adhesion strength, if a rising R-curve is observed, normalize the results by the shape of the R-curve.

The above items are discussed in detail in Chapter 4.

Approach for Objective 3

1. Perform fatigue-loading experiments and determine interfacial crack growth as a function of applied loading parameters for DCB samples of different thicknesses to explore behavior at different mode-mixites
2. Employ compliance changes to determine crack length with load cycling.
3. Explore if a unified interfacial fatigue fracture model is feasible

The above items are discussed in detail in Chapter 5.

Approach for Objective 4

1. Determine monotonic CZM parameters for mode I and mode II
2. Determine how the cohesive-zone models need to be modified to account for fatigue crack propagation.
3. Develop energy decrement method to establish a crack growth model as a function of calculated applied strain energy magnitude.
4. Use the modified cohesive-zone model to predict crack length with fatigue loading cycles.
5. Evaluate how the fatigue CZM predictions compare against experimental observations.

The above items are discussed in detail in Chapter 6.

CHAPTER 3. ON THE MATHEMATICAL FORM OF THE INTERFACIAL STRENGTH VS. MODE-MIXITY RELATIONSHIP

***Abstract* —** Interfacial fracture energy versus mode-mixity curves have been generated by researchers for various polymer / metal interfaces. The shapes of these relationships are normally reported through empirical fits. In this work an epoxy molding compound / copper interface has been characterized through a wide range of experiments and associated mode-mixities. In the current work, fracture energy test data is obtained through double-cantilever beam (DCB), four-point bend (4PB) and a dissimilar mixed mode bend (DMMB) test. Some of the commonly used mathematical forms of fracture energy vs. mode-mixity have been evaluated in the context of obtained test data. Additionally the appropriateness of linear-elastic fracture mechanics assumptions was evaluated. The mathematical form used to characterize the dependency on strain energy release rate and mode-mixity incorporates a failure criterion. Mathematical forms of the equations used to characterize the critical strain energy release rate and mode-mixity relationship are presented and linked to the options available in the ANSYS finite element cohesive-zone modeling functionality. The consequences of an inappropriate choice of mathematical form have also been considered.

3.1 Contextualization Notes Regarding Fit into the Overall Work

Prior to study of interfacial delamination under fatigue it is essential to conduct monotonic studies for three primary reasons. The first need for monotonic characterization is that every sample tested under fatigue must be first pre-characterized monotonically so that G_c magnitudes are available to use for normalization of the fatigue loading levels. The second driver for monotonic characterization is that it is well established that interfacial adhesion strength is a function of mode-mixity. Exploration of this dependency, and characterization of its shape, is needed so that when the mode-mixity dependency under fatigue is explored any correlations between monotonic and fatigue behavior, if existent, can be noted. Finally, given the intended incorporation of the mode-mixity relationships for interfacial failure under both monotonic and fatigue conditions, consistency between the mathematical forms used to capture the mode-mixity dependency and those used to establish numerical models, must be verified.

At the time of this writing the work contained in this chapter was being submitted for publication in the International Journal of Fracture.

3.2 Background / Intro

Significant study has been focused on interfacial fracture as a failure mechanism for microelectronic packages. Bimaterial interfaces are nearly ubiquitous in modern microelectronics and are subjected to thermal stresses resulting from the mismatch of thermal expansion coefficients of the incorporated materials. The impact on interfacial delamination for bimaterials for various both monotonic [4, 23, 24] and fatigue [17, 25-30] loading conditions has been studied. Degradation mechanisms such as thermal and

moisture exposure [31, 32] have also been explored. The desired outcome of many studies is a defined relationship between the particular phenomena under study and the interfacial adhesion strength.

It is of particular note that interfacial adhesion strength has been observed to be a function of the load orientation conditions as captured by the relative in-plane shear (mode II) and tensile (mode I) loading magnitudes, otherwise known as mode-mixity or ψ. To fully describe the adhesion strength for a bimaterial specimen, regardless of the additional phenomena under study, requires the determination of an interfacial strength to mode-mixity relationship. Hutchinson and Suo [33] among others [34] have described various forms which can be used to characterize the mode-mixity dependency.

An interfacial strength to mode-mixity relationship, once obtained, can be incorporated into the finite element models used as part of package design. Also the creation of modeling simulations which can incorporate additional functionality such as thermal degradation and fatigue has been the focus of numerous investigators [21, 22, 35].

It is generally accepted that both the studies pursued by experimentalists and theorists behind the creation of new numerical simulations are integral parts of any robust engineering sub discipline. In the case of cohesive-zone modeling however, it has been observed that additional focus is warranted regarding the incorporation of the relationships determined by the experimentalists and the models created by the theorists. [36] Specifically the mathematical form of the derived adhesion strength to mode-mixity relationship must match that utilized in any model which attempts to utilize that data.

The mathematical forms presented by Hutchinson and Suo [33] are almost universally referenced, to the point of being accepted on premise, despite the fact that Hutchinson and Suo stated in the referenced work that the forms offer no fundamental correctness beyond that they seem to fit most experimental data well. By relying on empirically fit curves, the mathematical forms of the interfacial strength to mode-mixity relationship risk being inconsistent with those incorporated into commercial FEA packages unless care is taken to ensure the modeling implementation matches the most commonly referenced form used by most experimentalists.

This work focuses on the establishment of an interfacial strength to mode-mixity relationship for a copper-epoxy molding compound bimaterial through the use of Double Cantilever Beam (DCB), Four-Point Bend (4PB) and Dissimilar Mixed Mode Bending (DMMB) tests. The potential impact of the choice of mathematical form used to capture this relationship will then be discussed, specifically with reference to available choices in ANSYS.

3.3 Experimental

Interfacial adhesion testing can be performed through various methods. The required data obtained for such tests include applied loads, displacements and sometimes sample crack length. Mixed-mode fracture requires loading in both the normal and in plane directions with respect to the plane of the crack front. Such mixed mode loadings can be induced through one of two means: through multi-axial load application or through uniaxial testing for samples with some kind of asymmetry. The moment-free global loadings in DCB testing will apply pure mode I local loads at the crack tip for

samples which are perfectly symmetric for both geometry and material properties. In the case of DCB samples this would mean a geometrically symmetric sandwich specimen. If the sample is geometrically asymmetric and/or possesses asymmetry due to different materials; the globally applied mode I loading condition will be rotationally transformed into a mixed mode condition. The degree of this rotation being a function of the asymmetries involved. This study utilizes both multiple test configurations such as DCB, 4PB and DMMB and sample processing which results in multiple mode-mixites for the same test DCB test stand. Schematics for each test are shown in Figure 2

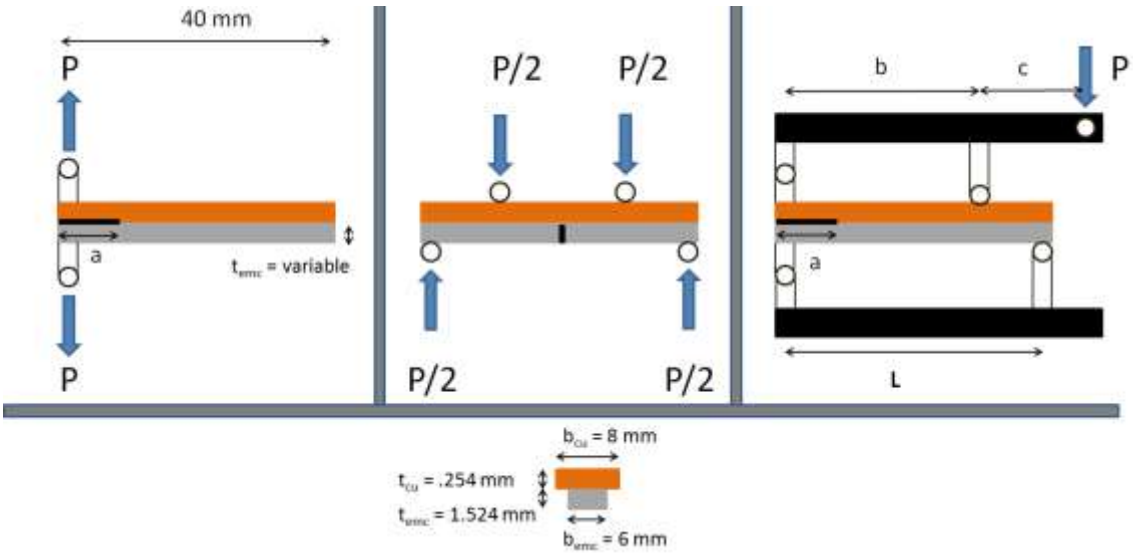

Figure 2 - Test Configuration Schematics: DCB, 4PB, DMMB

3.3.1 Double-Cantilever Beam

Double cantilever beam bimaterial samples were fabricated by curing flown epoxy molding compound over copper lead-frame. Pre-cracks are created manually by pressing down on the free copper end to separate it from the epoxy molding compound (EMC) while holding or fixing the other end of the specimen. DCB test fixtures are

made of aluminum and bonded to the bimaterial specimens with an epoxy adhesive. The sample fabrication and pre-crack creation methods are the same as those reported by the others previously.

Double cantilever beam tests were conducted on a *DTS Delaminator* as shown in Figure 3. Testing is conducted with samples of multiple thicknesses to obtain results at several mode-mixites. Different thicknesses are obtained by thinning the EMC side of the specimen with an end mill. Double sided tape is used to immobilize the samples for the milling process. This step is performed prior to the creation of the pre-crack for the specimens which are thinned.

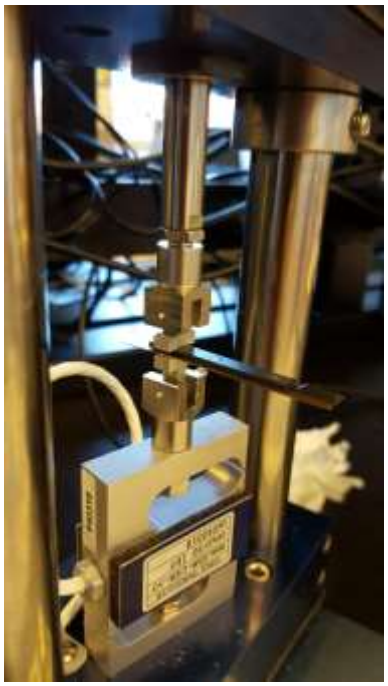

Figure 3 - DTS Delaminator

As seen in Figure 4, the crack propagates at the interface between the epoxy molding compound and the copper. The rightmost sample from set C shown in Figure 4c experienced bulk fracture as the crack kinked through the thinned epoxy molding

compound. All liberated copper surfaces are visibly clean as the epoxy molding compound has delaminated from the copper. The liberated copper surfaces formerly under the epoxy molding compound are different in color since they did not endure the oxidation experienced by the rest of the copper.

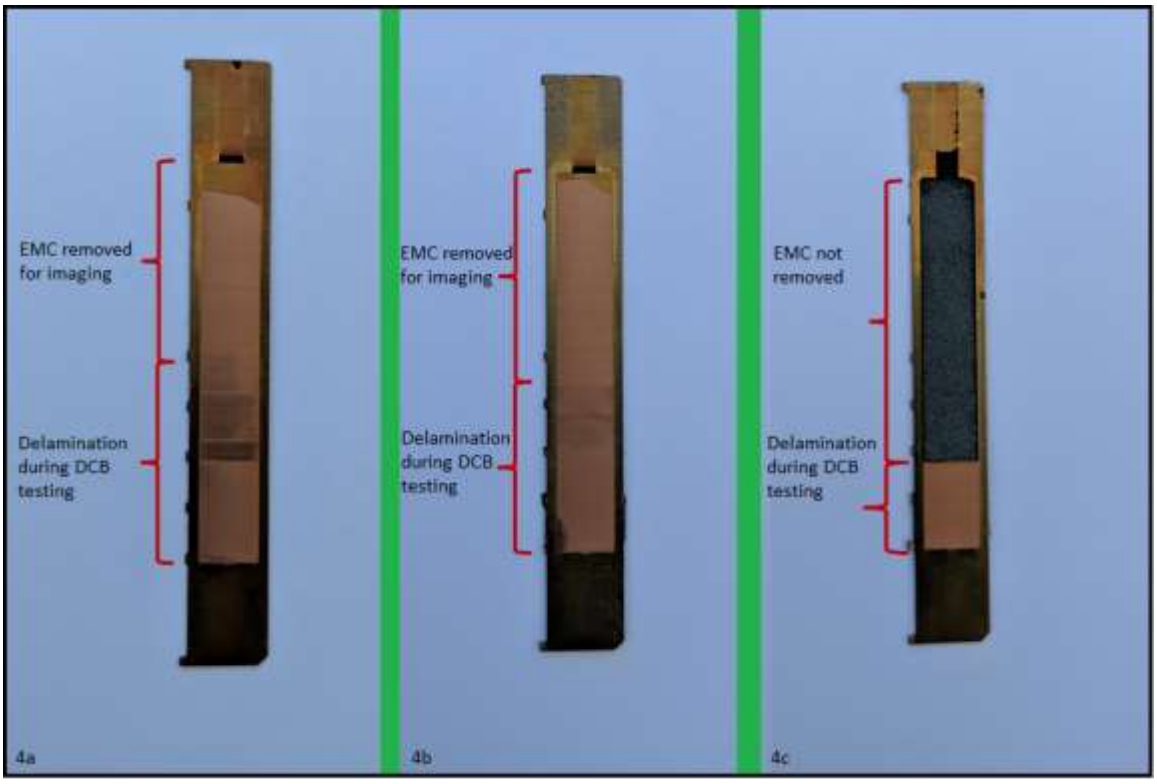

Figure 4 - Delaminated Copper Surfaces From Sample Sets A,B,C Left to Right

3.3.2 Four-Point Bend

Four-point bend samples are created by using the same cured samples as for the double cantilever beam tests by dicing a 50 μm wide line in the middle of the sample instead of attaching the fixtures used for the DCB tests. The cut is made in the mold compound to a depth of 150 μm above the mold compound and copper the interface so that the interface is not damaged. The remaining 150 μm is broken at the beginning of

the test during loading when the crack fractures this residual epoxy molding compound and then delaminates along the bimaterial interface. Four-point bend tests were performed as outlined by Krieger [37] on a *Test Resources* uniaxial test stand as shown in Figure 5.

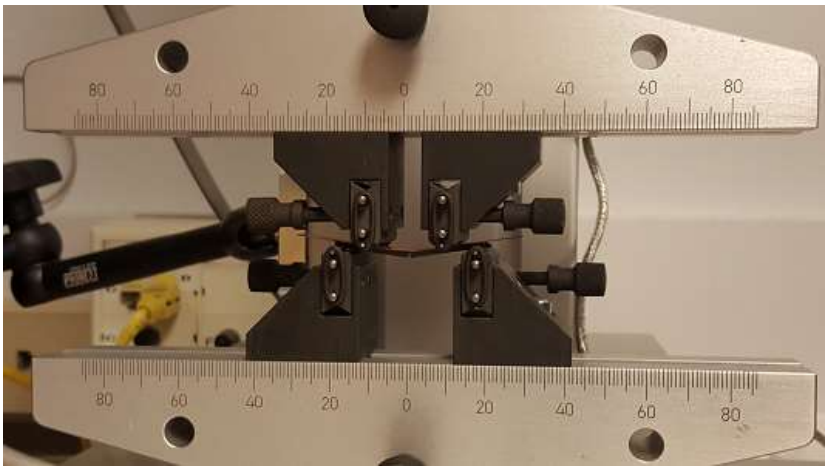

Figure 5 - Test Resources Uniaxial Test Stand

3.3.3 Dissimilar Mixed-Mode Bend

The mixed mode bend test is a configurable test outlined by Soboyejo [4] which combines tensile loading similar to that applied to DCB samples and the shear loading similar to an end notch flexure test. As the test setup is unsuited for compliance based crack length measurements, DMMB samples first are tested under DCB conditions on the *DTS Delaminator*. The final crack length for each sample calculated during this DCB pre-test is used for the DMMB experimental analysis. The DMMB setup is specifically designed to be run on the *Test Resources* stand such that standard DCB samples can be tested without requiring any changes to the sample bonded fixtures. The DMMB setup is shown in Figure 6.

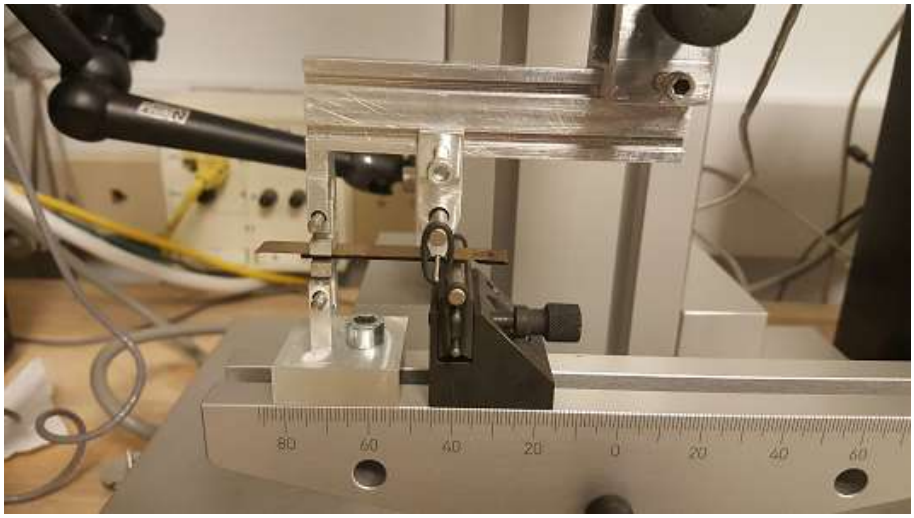

Figure 6 - Dissimilar Mixed-Mode Bend Test

3.4 Analytical Models

3.4.1 Double-Cantilever Beam

In previous work [38] the authors evaluated three different analytical formulations for calculating G_c. Equations by Soboyejo [4], Irwin [39] and equations resulting from the approach suggested by De Gracia [3] were compared and are shown in Equations 13-17. From these formulations it was found that the De Gracia adapted equations performed best. The complexities of the sample geometries involved make it such that in general mode-mixity will be determined numerically.

Soboyejo (1999):

$$G = \frac{6P^2a^2}{E_{EMC}b^2t_{EMC}^3}\left(1+\frac{1}{\beta_E\beta_H^3}\right); \qquad \beta_E = \frac{E_{Cu}}{E_{EMC}} \qquad \beta_H = \frac{t_{Cu}}{t_{EMC}} \tag{13}$$

Irwin (1954):

$$G = \frac{P^2}{2b}\frac{dC_{sys}}{da} \tag{14}$$

De Gracia (2015)

$$\delta = \frac{Pa^3}{3E_{f,cu}I_{cu}} + \frac{6Pa}{5\mu_{13,cu}A_{cu}} + \frac{Pa^3}{3E_{f,emc}I_{emc}} + \frac{6Pa}{5\mu_{13,emc}A_{emc}} \quad \textbf{15)}$$

$$C_{sys} = \frac{\delta}{P} = \frac{a^3}{3E_{f,cu}I_{cu}} + \frac{6a}{5\mu_{13,cu}A_{cu}} + \frac{a^3}{3E_{f,emc}I_{emc}} + \frac{6a}{5\mu_{13,emc}A_{emc}} \quad \textbf{16)}$$

$$G = \frac{P^2}{2b}\frac{dC_{sys}}{da} = \frac{P^2}{2b}\left(\frac{a^2}{E_{f,cu}I_{cu}} + \frac{6}{5\mu_{13,cu}A_{cu}} + \frac{a^2}{E_{f,emc}I_{emc}} + \frac{6}{5\mu_{13,emc}A_{emc}}\right) \quad \textbf{17)}$$

3.4.2 Four-Point Bend

The analytical forms used to calculate G_c for 4PB tests were those presented by Charalambides [40] as seen in Equation 18. Due to the complexities involved, the determination of mode-mixity is often limited to the use of numerical models as it was by Charalambides. For this reason no analytical form of mode-mixity for 4PB is presented here.

$$G = \frac{(1-\nu_{Cu}^2)P^2L^2}{8E_{Cu}b^2}\left(\frac{1}{I_{Cu}} - \frac{1}{I_C}\right); \quad I_{Cu} = \frac{t_{Cu}^3}{12}; \qquad \lambda = \frac{E_{Cu}(1-\nu_{EMC}^2)}{E_{EMC}(1-\nu_{Cu}^2)}; \quad \textbf{18)}$$

$$\mathrm{I_C} = \lambda \mathrm{I_{Cu}} + \frac{\mathrm{t_{EMC}^3}}{12} + \frac{\lambda \mathrm{t_{Cu}} \mathrm{t_{EMC}} (\mathrm{t_{Cu}} + \mathrm{t_{EMC}})^2}{4(\lambda \mathrm{t_{Cu}} + \mathrm{t_{EMC}})}$$

3.4.3 Dissimilar Mixed-Mode Bend

Analytical forms for both G_c and ψ were used presented by Soboyejo as shown in Equations 19 and 20 . It should be noted that for this work energy based mode-mixity is calculated using Equation 21 instead of that presented by Soboyejo in Equation 20. This is done to be consistent with a definition of $G_c = G_I + G_{II}$. This mode-mixity definition in Equation 21 also results in consistency with stress intensity based mode-mixity definitions shown in Equation 22.

$$G = G_I + G_{II}; \qquad \beta_E = \frac{E_{Cu}}{E_{EMC}}; \qquad \beta_H = \frac{t_{Cu}}{t_{EMC}}; \tag{19}$$

$$G_I = \frac{3P^2a^2}{2E_1B^2h_1^3}\left(1+\frac{1}{\beta_E\beta_H^3}\right)\left[\frac{c}{b_P}-\left(1-\frac{b_P+c}{L}\right)\right]^2;$$

$$G_{II} = \frac{3P^2a^2}{2E_2B^2h_2^3}\left\{\left(1+\frac{1}{\beta_E\beta_H^3}\right) - \frac{4\left[1+\beta_E\beta_H^3+\frac{3\beta_H(1+\beta_H)^2(\beta_E^2\beta_H+1)}{1+\beta_E{\beta_H}^2}\right]}{\left[1+\beta_E\beta_H^3+\frac{3\beta_E\beta_H(1+\beta_H)^2}{1+\beta_E\beta_H}\right]^2}\right\}\left[\frac{c}{b_P}+\left(1-\frac{b_P+c}{L}\right)\right]^2;$$

$$\psi = \tan^{-1}\frac{G_{II}}{G_I}; \tag{20}$$

3.5 Numerical Models

Numerical models were created for the calculation of G_c and ψ; for each two different methods were explored. All numerical models were elastic-plastic 3D models

with modeled loading pins with contact surfaces to apply the loads. In all cases the geometry was faithfully recreated such that minimal assumptions were made though symmetry was exploited wherever appropriate. 3D models were necessary due to the poor accuracy of 2D models, which likely stemmed from the atypically small fracture samples utilized and lack of a uniform cross section due to the difference in thickness between copper and the epoxy molding compound. Mesh density was refined to an element size of 50 μm around the crack front while coarse away from the region of interest to reduce computation time. Symmetry was exploited where available resulting in half-symmetric models for DCB and DMMB and a quarter-symmetric model for 4PB. Examples of the numerical models are illustrated in Figure 7.

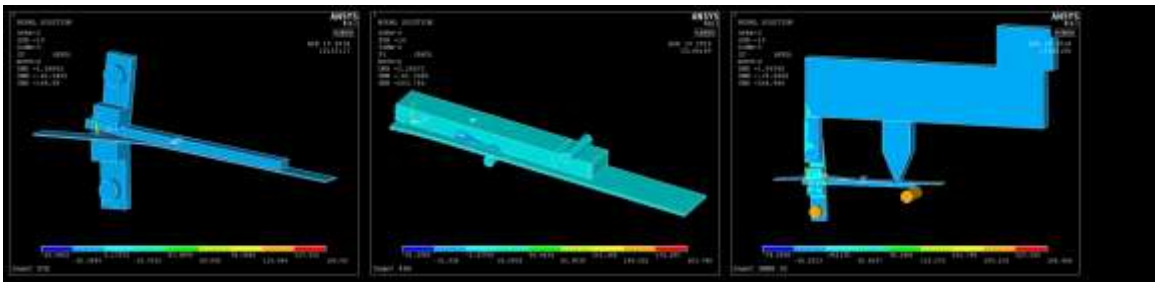

Figure 7 - Numerical Models - DCB, 4PB and DMMB

3.5.1 Critical SERR

ANSYS provides two different numerical methods for the calculation of G_c: the Virtual Crack Closure Technique (VCCT) and the J-Integral. The VCCT routine established by Rybicki and Kanninen [6] assumes self-similar crack growth and uses crack tip opening displacements to calculate the energy required to close the crack which for LEFM is the same as the critical SERR. The J-Integral technique originally proposed by Rice [41] uses a contour integral to calculate the energy of fracture. Unlike VCCT, J-

Integral incorporates nonlinear effects and in certain cases can be used to analyze the cracking of elastic plastic materials. Care must be exercised in these cases however, as the path independence of the integral is not guaranteed for these cases, even more so when homogeneity is violated as for bimaterial interfaces.

3.5.2 Mode-Mixity

ANSYS does not provide any automatic calculation of mode-mixity. Processing of available data can provide two methods for calculating ψ. Both a displacement or stress based (ψ) and an energy based (ψ_G) formulation of mode-mixity can be established. It is important to distinguish between the two forms as they are phase offset from one another. Displacement-based ψ can be calculated by utilizing the crack surface displacement method presented by Matos et al. [42]. The SERR-based ψ_G can be determined by taking the arctangent of the square root of the ratio of shear to tensile strain energies as shown in Equation 21. It has been shown by Schlottig [43] and confirmed by the authors that this formulation of ψ_G is phase offset from ψ. This is the form favored by the current authors as it removes the need for abstracted references lengths. It also establishes a zero degree mode-mixity as being coincidental with the minimum critical SERR. This minimum location is fundamentally favorable due to the assumption that the minimum fracture energy should occur when the crack tip is under pure tensile loading only.

$$\psi_G = \tan^{-1}\sqrt{\frac{G_{II}}{G_I}}; \qquad \textbf{21)}$$

$$\psi = \tan^{-1}\frac{K_{II}}{K_I}; \quad \textbf{22)}$$

3.6 Test Results

Analytical SERR values were computed using the De Gracia [3] based, Charalambides [40], and Soboyejo [4] relationships. Reported numerical SERR values were calculated using the ANSYS VCCT routine for the associated geometries and test cases. J-Integral was also performed and compared against as a check for consistency which can speak to the correctness of the underlying LEFM assumptions. J-Integral also assists in confirming the appropriateness of the chosen mesh since as a domain calculation J-Integral is less susceptible to influences of the crack front singularity.

3.6.1 Double-Cantilever Beam

DCB samples of three different thicknesses were tested for an identical copper / epoxy molding compound interface. Sample EMC thicknesses were assumed for FEA purposes to be 1.524 mm (as received), 0.774 mm (0.75 mm of EMC removed), and 0.556 mm (roughly 1 mm of EMC removed). The copper thickness was 0.254 mm. The different EMC thickness sample sets will be referred to as A, B, and C respectively. For the reported sample sets the actual thicknesses as measured by calipers ranged from 0.746 – 0.786 mm for sample set B and 0.536-0.576 mm for sample set C. Sample set A was consistent to specification as it was unmodified after the molding process.

3.6.2 Nominal Sample Set A

Several load-delaminate-unload cycles were performed for each sample. For each of these cycles, the displacement-controlled sample is moved at a rate of 5 μm/sec until delamination occurs as reflected by the load level plateauing and eventually decreasing. After some the desired extent of delamination has occurred the movement is reversed and the sample fully unloaded. These steps are repeated as necessary. Results for an illustrative test are shown in Figure 8 for sample A2. The reported SERR values are for the final load/unload cycle for each sample. It was previously noted that the nominal samples demonstrated a rising R-curve. Due to the rising R-curve the last peak was chosen such that the reported SERR values are for after the R-curve has plateaued at a constant G_c value. The average SERR for these samples was 54.6 J/m^2 analytically and J/m^2 numerically. Results for sample set A are shown in Table 1.

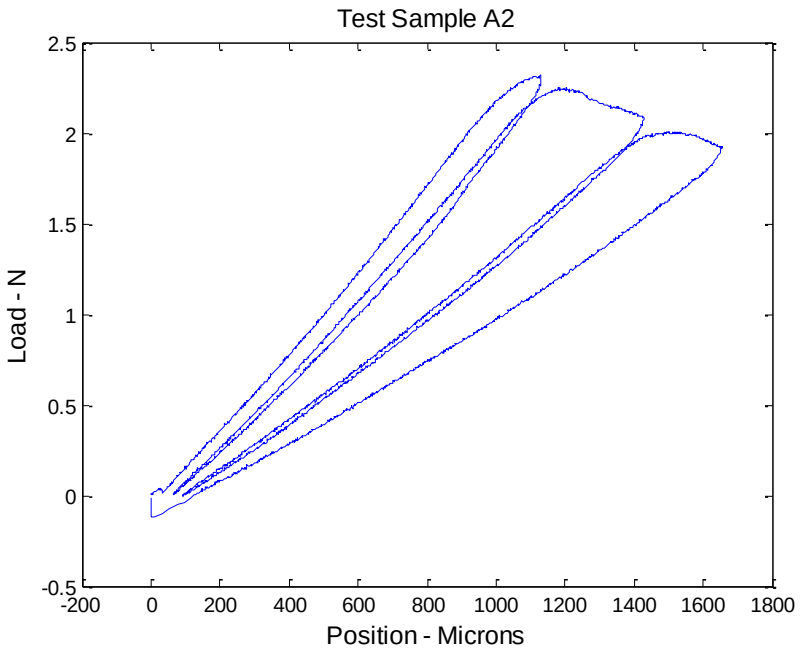

Figure 8 - Load-Displacement Data Sample A2

Table 1 - DCB Set A Results

Nominal 1.524 mm thick EMC	Analytical SERR (J/m^2)	Numerical SERR (J/m^2)
A1	60.8	53.1
A2	54.6	48.0
A3	59.3	52.2
A4	42.1	39.5
A5	57.9	50.3
A6	49.4	43.3
Average	**54.0**	**47.7**

3.6.3 Thinned Sample Set B

Unlike the nominal samples in set A, the thinned samples in set B did not demonstrate any rising R-curve behavior. This is likely a result of the sample's higher aspect ratio (from reduced thickness) making the samples more accurately modeled as a cantilever beam under a pure bending moment load. The De Gracia inspired analytical form needed to incorporate shear loading effects to attain accuracy. This is supported by the fact that for these samples there was nearly no difference between the analytical results for the De Gracia form or an Irwin based calculation. For the nominal samples the equations diverge for very short crack lengths during when the rising R-curve is in effect. The average SERR for these samples was 36.9 J/m^2 analytically and 33.4 J/m^2 numerically. An example of the load-displacement test data is shown for sample B1 in Figure 8. Results for set B are reported in Table 2

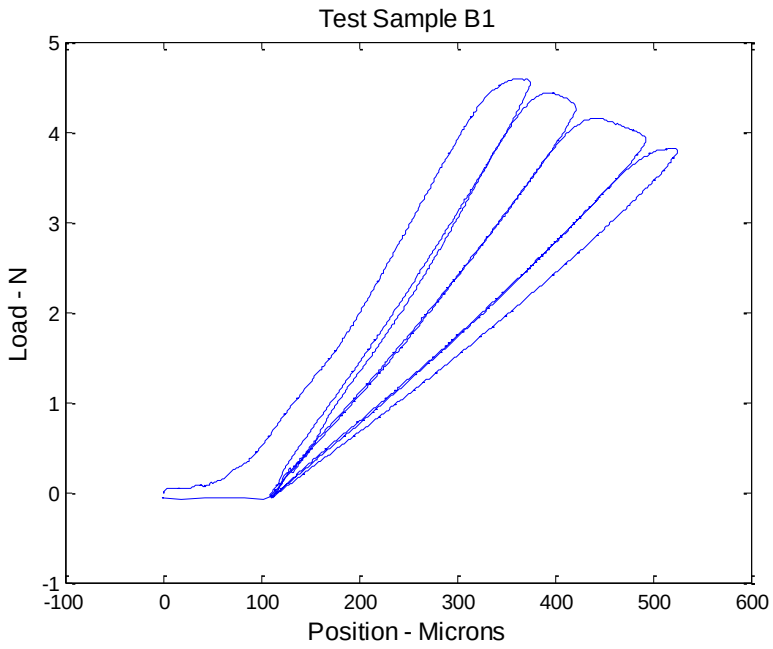

Figure 9 - Load-Displacement Data Sample B1

Table 2 - DCB Set B Results

Thinned 0.774 mm thick EMC	Analytical SERR (J/m^2)	Numerical SERR (J/m^2)
B1	33.6	30.5
B2	36.0	32.1
B3	38.2	35.1
B4	36.7	32.7
B5	40.0	36.5
B6	37.1	33.7
Average	**36.9**	**33.4**

3.6.4 Thinned Sample Set C

Sample set C, similar to sample set B, did not demonstrate any rising R curve behavior. The average SERR for these samples was 52.5 J/m^2 analytically and 48.5 J/m^2 numerically. These values are higher than those for sample B and more similar to those

of the nominal sample set A. The results for sample C3 are show in Figure 10. Sample set C results are shown in Table 3.

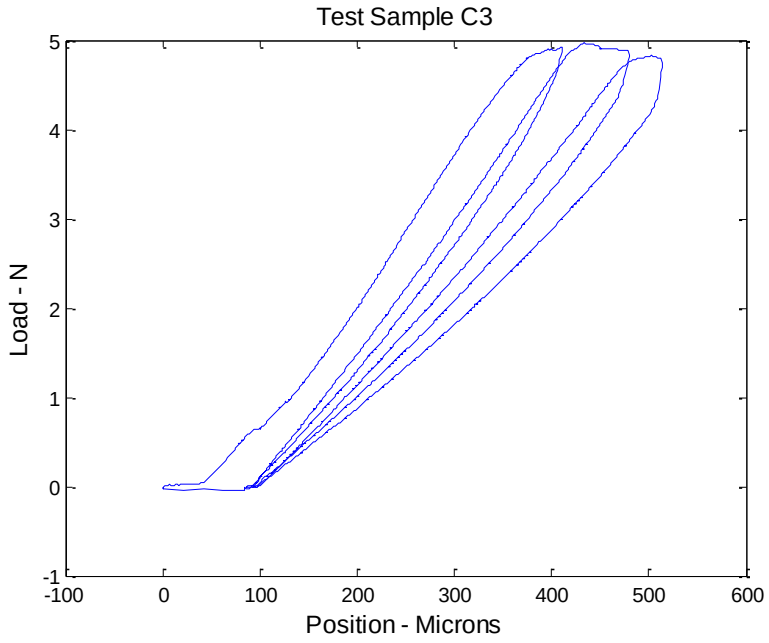

Figure 10 - Load-Displacement Data Sample C3

Table 3 - DCB Set C Results

Thinned 0.554 mm thick EMC	Analytical SERR (J/m^2)	Numerical SERR (J/m^2)
C1	47.5	41.2
C2	53.2	51.6
C3	58.2	53.3
C4	52.0	46.5
C5	49.2	43.6
C6	54.6	48.7
Average	**52.5**	**47.5**

3.6.5 Four-Point Bend

Unlike double cantilever beam testing, four-point bend fracture tests do not require crack length to be known to calculate G_c. Only sample geometry and the critical

load are required to determine the critical SERR. Results for an illustrative test are shown in Figure 11 for sample D2. The values for four tested 4PB samples are given in Table 4. Analytical SERR was calculated per the equations provided by Charalambides [40].

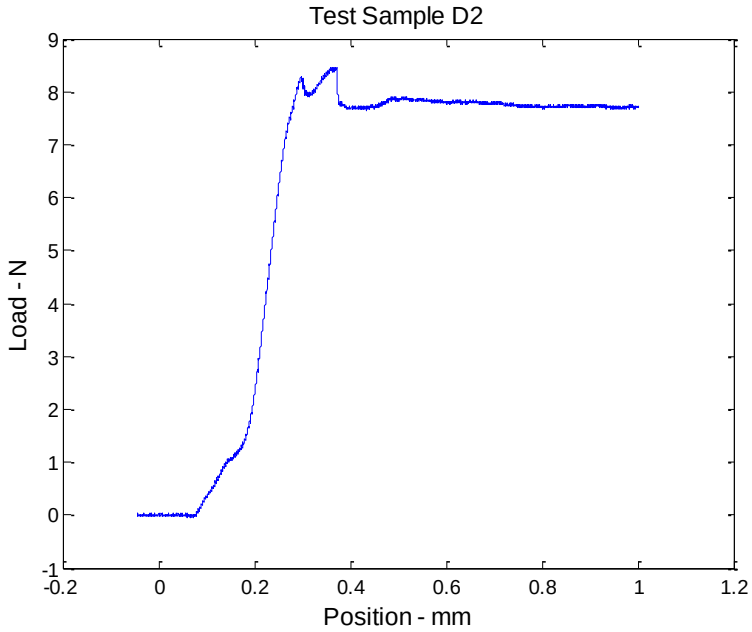

Figure 11 - Load-Displacement Data Sample D2

Table 4 - Four-Point Bend Results

Sample	P_{crit} (N)	Analytical SERR (J/m^2)	Numerical SERR (J/m^2)
D1	7.43	65.6	47.6
D2	7.73	71.0	50.7
D3	8.05	77.0	55.3
D4	7.46	66.2	48.0
Average	**7.67**	**70.0**	**50.4**

The invariance of crack length on G_c was explored with modeled crack lengths of 2 mm, 4 mm, 6 mm, and 8 mm. The mesh density required for G_c convergence varied for differing crack lengths but once mesh convergence was attained as evaluated by G_c no

crack length dependency on G_c was observed. Reported numerical G_c values for 4PB tests were calculated assuming a crack length of 6 mm.

3.6.6 Dissimilar Mixed-Mode Bending

Dissimilar mixed-mode bend test results are shown in Table 5 and Figure 11. Four samples were tested but testing difficulties such as bulk fracture rather than interfacial delamination invalidated results for three of the samples. For the fourth sample, subsequent analysis determined that for the copper / EMC bimaterial interface under study, the test itself violates the requirements of LEFM and as such is invalid. This will be discussed in greater detail in section regarding small-scale yielding.

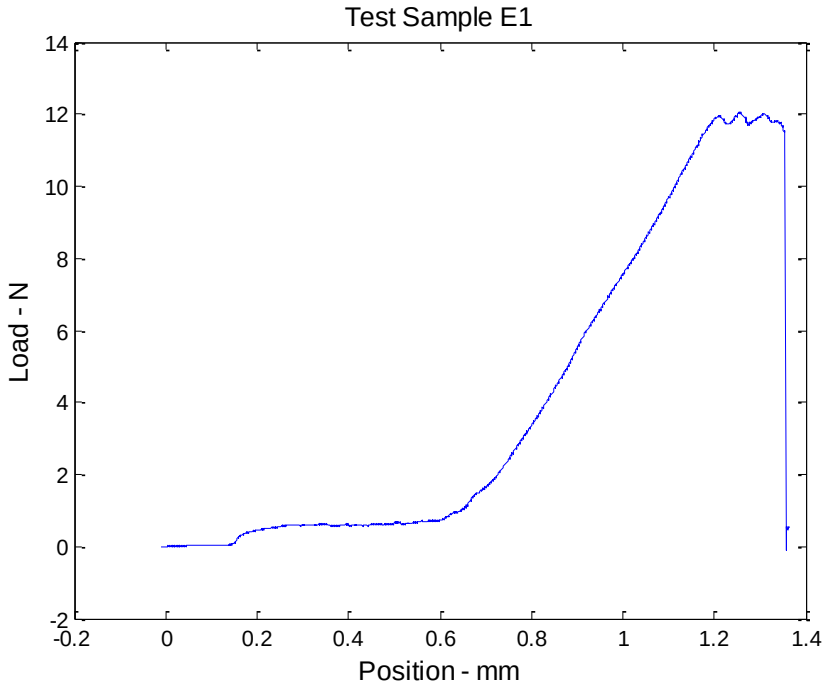

Figure 12 - Load-Displacement Data Sample E1

Table 5 - DMMB Results

Sample	P_{crit} (N)	Analytical SERR (J/m^2)	Numerical SERR (J/m^2)
E1	11.7	185.6	73.7

3.6.7 Mode-Mixity

The mode-mixity for the nominal samples is shown in Table 6. In general, mode-mixity values are extremely consistent between different test samples and data points with no significant dependency on crack length as long as the crack is not so long as to incur edge effects from the end of the beam. This is expected as mode-mixity should be a function of geometry, material properties and loading geometry all of which are invariant for a given DCB bimaterial sample geometry. For DCB samples there is also negligible variation in ψ or ψ_G with respect to widthwise location and the reported values were evaluated at the center of the sample. For the displacement-based calculations, per Matos these values are determined from representative test cases. Averaging was not done for the displacement-based mode-mixity calculations as it was for the SERR-based mode-mixity as the numerical computation of mode-mixity for the Matos method is labor intensive and unnecessary due to the observed consistency.

A special note regarding the mode-mixity of sample set C is warranted. As the quantities G_I and G_{II} are energy densities, the values used to calculate ψ_G are always positive. Displacement-based ψ values can directional orientation information through the sign of the displacements. Variations in the sample asymmetry by changing the thickness of the EMC can rotate the orientation of the crack tip stress field. The orientation of the stress field is in turn characterized by mode-mixity. In the case of

sample set C, these changes resulted in a direction change with respect to the coordinate system assumed, in this case a zero angle defined by pure mode I loading. As a result the magnitude of ψ_G is correct but a negative sign must be added to distinguish the different orientation. In other words, if described by a standard Cartesian coordinate system, the shear energies in sets A and B reside in quadrant one while those in set C lie in quadrant two.

For 4PB tests the average SERR mode-mixity across the entire crack front was similarly constant for the various tests though there was a slight variation in the magnitude of the edge effects for different crack lengths

Table 6 - Analytical and Numerical Mode-Mixity

Test geometry	Analytical ψ	Numerical ψ (Matos)	ψ_G (SERR-based)	Average Numerical SERR
DCB set A (A2)	NA	31.0	17.3	47.7
DCB set B (B4)	NA	15.8	2.54	33.4
DCB set C (C5)	NA	4.78	(-) 7.93	47.5
4PB (D4)	NA	37.3	21.1	50.4
DMMB (E1)	37.36	4.84	0.816	73.7

3.7 Small-Scale Yielding

Since cohesive-zone modeling simulates crack propagation in an energy conservative fashion by reducing the element stiffness once the traction-separation law is traversed, an underlying assumption of LEFM is incorporated. As a result, the fracture test data to be used to build the CZM model, in the forms of the DCB, 4PB and potentially DMMB tests must be appropriately well characterized through LEFM.

Due to the presence of the crack tip singularity VCCT and J-Integral account for the impact of localized plasticity differently but must agree with each other. For VCCT, while stresses are non-convergent at the crack tip for mesh refinement, energy will be convergent. J-Integral on the other hand, as a domain integral method, is less susceptible to the issues presented by the singularity. The contour integrals however must be performed sufficiently close to the crack tip such that the contours are fully within the plastic zone. As such for both cases, while plasticity is always present due to the singularity, the appropriateness of a small-scale yielding assumption is determined by the intensity of the localized plasticity around the crack tip and the size of the region where plasticity is present.

Figure 13 shows only the copper near the crack tip for a nominal DCB test sample from set A. The copper demonstrates a small localized area of plasticity at the crack front. The VCCT and J-Integral results for DCB samples were all in agreement, which combined with the plastic zone being only 1 element in size confirms the applicability of small-scale yielding assumptions. ANSYS simulations for sets B and C did not exhibit any plastic strain energy.

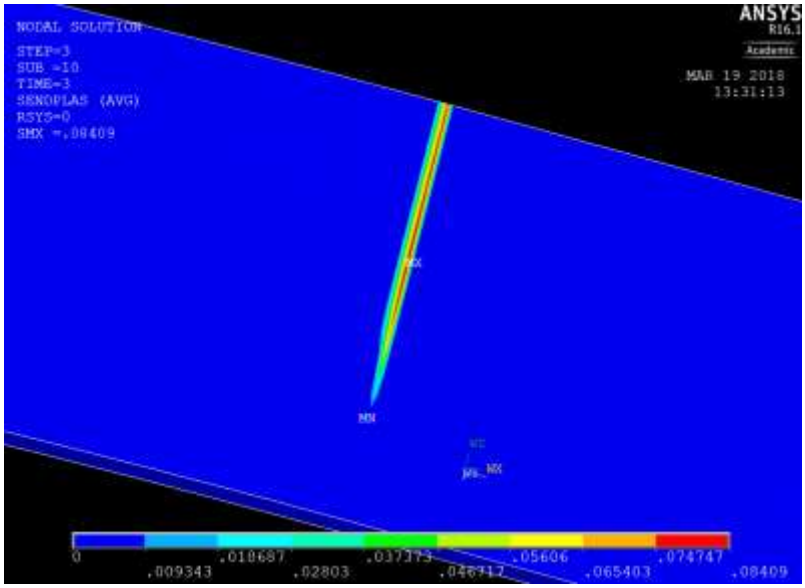

Figure 13 - Sample A3: Plastic Strain Energy (Half Symmetric Model)

As shown in Figure 14, 4PB shows higher magnitude of plastic strain energy for the copper near the crack tip than for the DCB test specimens. While the error between analytical and numerical SERR is larger for 4PB, the plastic strain energy is localized to the same region as DCB and the appropriateness of small-scale yielding assumptions is still supported as the plastic strain energy is negligible compared to the fracture energy of the system. It is worth noting that similar to DCB, the assumptions in the Charalambides 4PB SERR equation, such as 2D plane strain result in non-negligible errors in value as compared to the numerical results for the smaller samples used in this study. The increase in plasticity shows that while still valid, the higher mode-mixity tested in 4PB is nearing the boundary at which LEFM will no longer be appropriate.

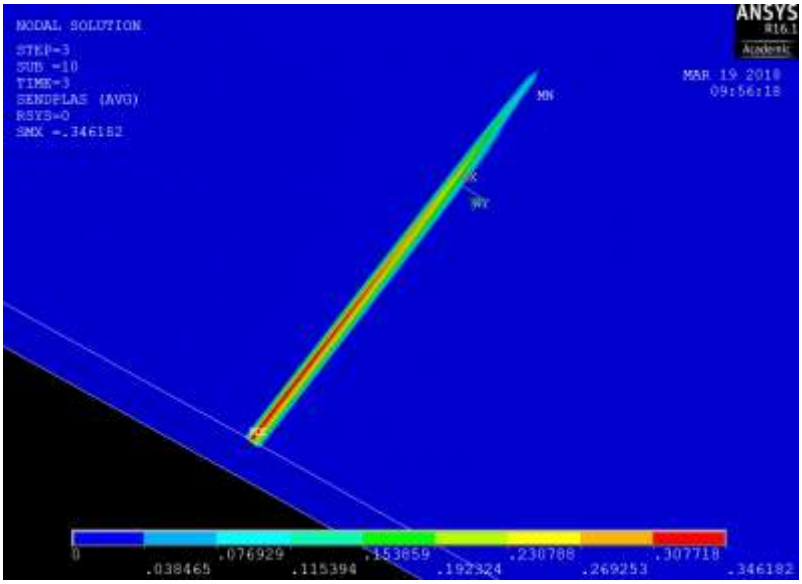

Figure 14 - Sample D1: Plastic Strain Energy (Half Symmetric Model)

The results for the DMMB tests clearly show violation of small-scale yielding. While the analytical forms in Soboyejo would imply a very high mode-mixity with high critical SERR of 37° and 160 J/m^2 respectively, the numerical results clearly show significant plasticity in a region much greater in size than that for the other test geometries. The larger zone of plasticity is shown in Figure 15. In addition to the significant plastic yielding occurring near the crack tip itself plasticity also starts to develop near one of the loading pins. These results indicate that for the copper / epoxy molding compound bimaterial interface under study, DMMB does not provide valid results as the plasticity incurred dominates the crack's behavior. The plastic behavior can also be seen to cause shear stress alleviation. As a result the local mode-mixity in the DMMB test is nearly pure mode I at 0.816 degrees. This is due to the global loading being pure mode I due to the uniaxial test stand used, and stress alleviation in plasticity being preferential to mode I due to the applied global load geometry.

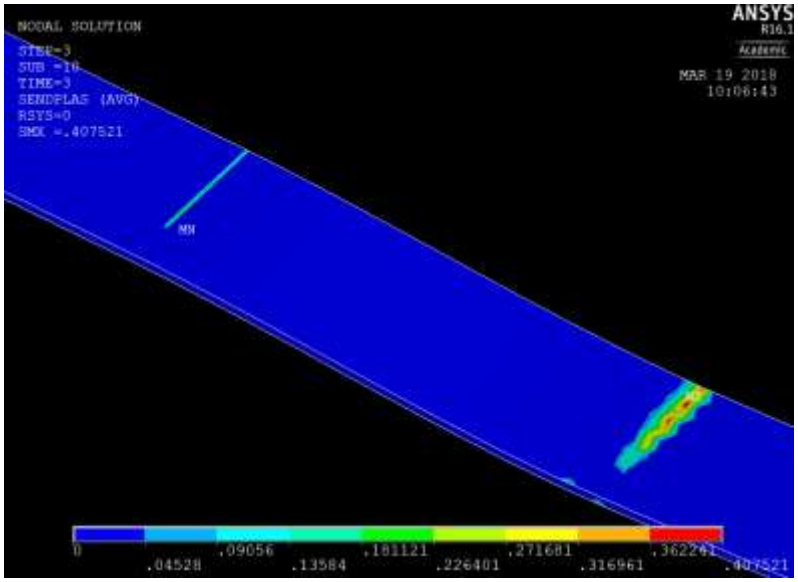

Figure 15 - DMMB Plastic Strain Energy (Half Symmetric Model)

3.8 Mathematical Forms of ψ vs. Gc

In discussing mixed mode fracture, the delamination condition can be represented in two equivalent but distinct ways. The first as seen in numerous studies [34, 44], represent the G_I and G_{II} conditions when delamination occurs and plots them in this space, defining a failure locus. 3D models are evaluated consistent with this distinction evaluating behavior between within the shear plane and normal to it. ANSYS interface material models for exponential and bilinear CZM test for complete delamination of the element based upon failure loci in this mixed mode space. The exponential CZM used in ANSYS is based on the work of Xu and Needleman [12], while both interface and contact element bilinear CZMs are based on the work of Alfano and Crisfield [14]. An example of an elliptical failure criterion as described by Alfano and Crisfield is shown in Figure 16. For this criterion failure occurs when the loading condition is located on our outside the boundary defined by the elliptical curve.

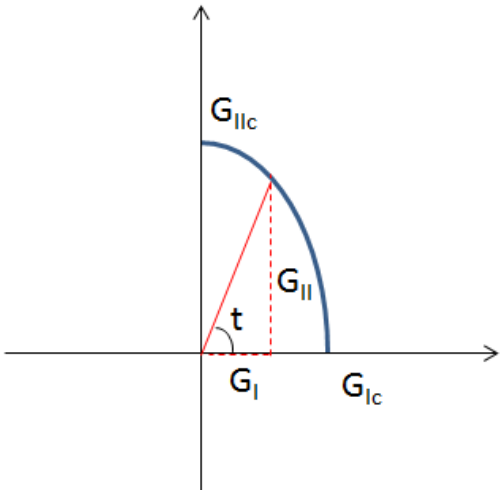

Figure 16 - Elliptical Failure Criterion

Practically speaking however, experimentalists often favor a second mathematical space, that defined by the total energy at fracture, the previously mentioned G_c and the mode-mixity ψ_G. This preference is often a practical one as many tests naturally report total G rather than mode separated G values. It is then a matter of calculating mode-mixity to fully define the mixed mode fracture condition. In particular one of the most cited works on mixed mode fracture, by Hutchinson and Suo, operates in this space. While in many ways more convenient and intuitive, this perspective has several conceptual risks which must be considered. An example of a Hutchinson and Suo curve is shown in Figure 17. For this case, failure occurs when the loading condition resides above the line defined by the criterion's trigonometric function.

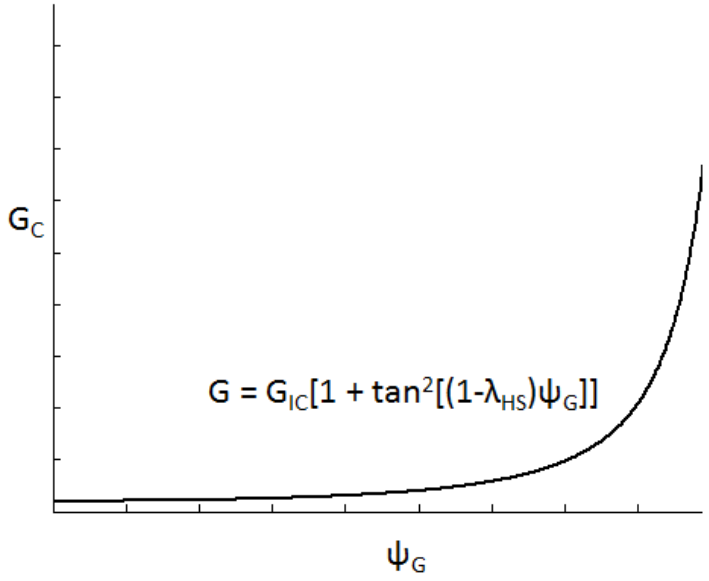

Figure 17 - Hutchinson and Suo Failure Criterion

In studying bimaterial fracture it is desirable to be able to interrogate the data in either the G_I and G_{II} space or the G_c vs. ψ_G pairing. For an elliptical failure criterion equivalent representations are possible.

$$\left(\frac{G_I}{G_{IC}}\right) + \left(\frac{G_{II}}{G_{IIC}}\right) = 1 \quad \textbf{23)}$$

$$\left(\frac{G_I}{G_{IC}}\right)^2 + \left(\frac{G_{II}}{G_{IIC}}\right)^2 = 1 \quad \textbf{24)}$$

$$G_C = G_{IC}\left[1 + tan^2\left((1 - \lambda_{HS})\psi_G\right)\right] \quad \textbf{25)}$$

Equation 23 describes a linear failure criterion while Equation 24 describes the elliptical criterion. The Hutchinson and Suo equation which has been observed to best fit the behavior of bimaterial interfaces is shown in Equation 25. G_{IC} is the energy of fracture for pure mode I loading, G_{IIC} is the energy of fracture for pure mode II loading. G_c is the

total critical fracture energy. λ_{HS} is an empirical shaping parameter which varies the mode II contribution towards fracture. Per Hutchinson and Suo, $\lambda_{HS} = 1$ can be considered "ideally brittle" while for $\lambda_{HS} = 0$ fracture depends only on the mode I contribution.

By energy conservation it can be stated that:

$$G_{total} = G_I + G_{II} \quad \textbf{26)}$$

This is consistent with the definition of mode-mixity angle as defined by Equation 21. The equation for an ellipse can be parameterized and subsequently G_I and G_{II} represented as functions of G_{IC} and G_{IIC} along with the parameter "t" as shown in Equations 27 and 28.

$$G_I = G_{Ic} \cos t \quad \textbf{27)}$$

$$G_{II} = G_{IIc} \sin t \quad \textbf{28)}$$

In order to represent the elliptical failure criterion in terms of G_c and ψ_G rather than G_{IC} and G_{IIC} we need to relate ψ to the parameter t. Squaring both sides of Equation 21 yields equation 29.

$$tan^2(\psi_G) = \frac{G_{II}}{G_I} \quad \textbf{29)}$$

Noting Equations 27 and 28 and relating them to Equation 29 we can obtain the following:

$$tan^2(\psi_G) = \frac{G_{II}}{G_I} = \frac{G_{IIc}\sin t}{G_{Ic}\cos t} = \frac{G_{IIc}}{G_{Ic}} tan\, t \quad \textbf{30)}$$

$$t = \tan^{-1}\left(\frac{G_{Ic}}{G_{IIc}} tan^2(\psi_G)\right) \quad \textbf{31)}$$

With Equation 31 in hand we can now represent the total energy at fracture as defined by an elliptical failure criterion in Equation 32 and then eliminate the parameter t by substituting Equation 31 into 32 as shown in Equation 33.

$$G_{total} = G_{Ic}\cos t + G_{IIc}\sin t \quad \textbf{32)}$$

$$G_{total} = G_{Ic}\, cos\left(tan^{-1}\left(\frac{G_{Ic}}{G_{IIc}} tan^2(\psi_G)\right)\right) + G_{IIc}\, sin\left(tan^{-1}\left(\frac{G_{Ic}}{G_{IIc}} tan^2(\psi_G)\right)\right) \quad \textbf{33)}$$

We have now obtained a curve which can be fit to three parameters similar to the Hutchinson and Suo relationship. In Hutchinson and Suo the three parameters are G_{IC}, ψ_G, and λ_{HS}. λ_{HS} is defined as a fitting parameter to adjust the mode 2 contribution to fracture. The G_c to ψ_G relationship of Equation 33 requires G_{IC}, G_{IIC}, and ψ_G.

Both the Hutchinson and Suo and the elliptical failure criterion are capable of describing a failure locus for a collection of points but they may or may not result in similar values across all mode-mixites depending on the data used to generate the curves. Figure 18 shows the normalized G_C / G_{IC} values as a function of mode-mixity for different values of λ in the Hutchinson and Suo criterion. λ is defined between 0 and 1. As λ decreases, the maximum value of the G_C / G_{IC} ratio increases.

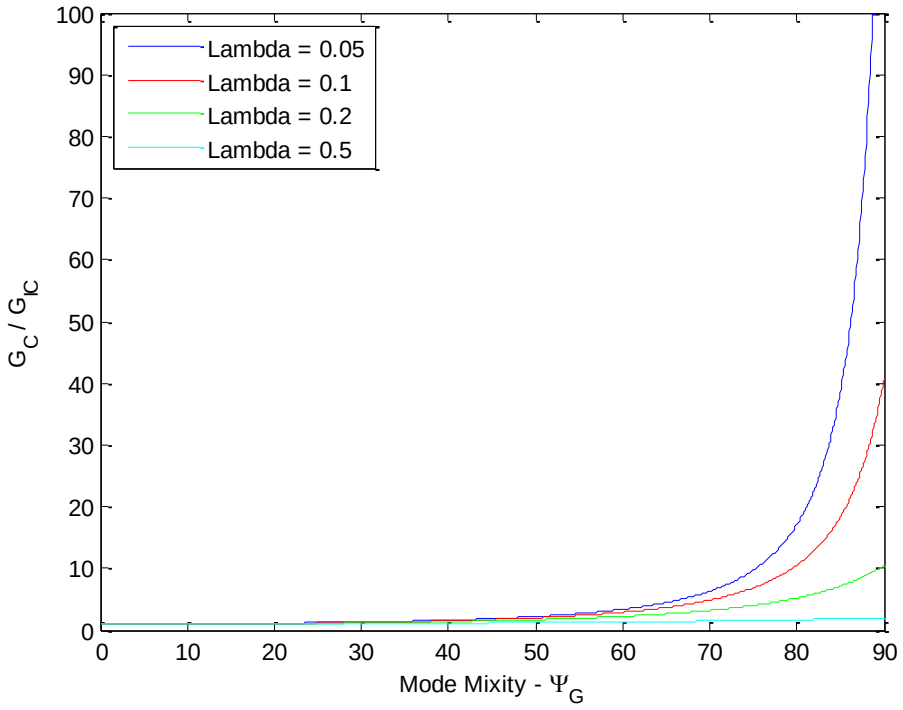

Figure 18 - Tan Square Variation Curves

Figure 19 shows the behavior of the G_C / G_{IC} ratio for different values of β for the elliptical failure criterion where β is defined as the ratio G_{IIC} / G_{IC}. Like the λ curves, the maximum value of the G_C / G_{IC} ratio can be modified through the β value with increasing values of β corresponding to larger ratios. An important difference between the curves generated for the Hutchinson and Suo criterion and those of the elliptical failure criterion is that changing the value of β also shifts the ψ_G location where the maximum G_C / G_{IC} ratio occurs. The Hutchinson and Suo criterion is always maximum at $\psi_G = 90°$.

Reviewing Figure 18 and Figure 19 it can be seen that certain combinations of λ and β values will result in similar curves. For values of λ=0.2 or lower, and values of β=10 or higher the difference in values along the Hutchinson and Suo and elliptical failure criterion curves will be minor through much of the range of mode-mixities. For

most of the polymer / metal interfaces, a ratio of β of 10 or greater is quite common. For l λ values above 0.2 and/or values of β below 10, the potential discrepancy between the two models may be meaningful and must be considered.

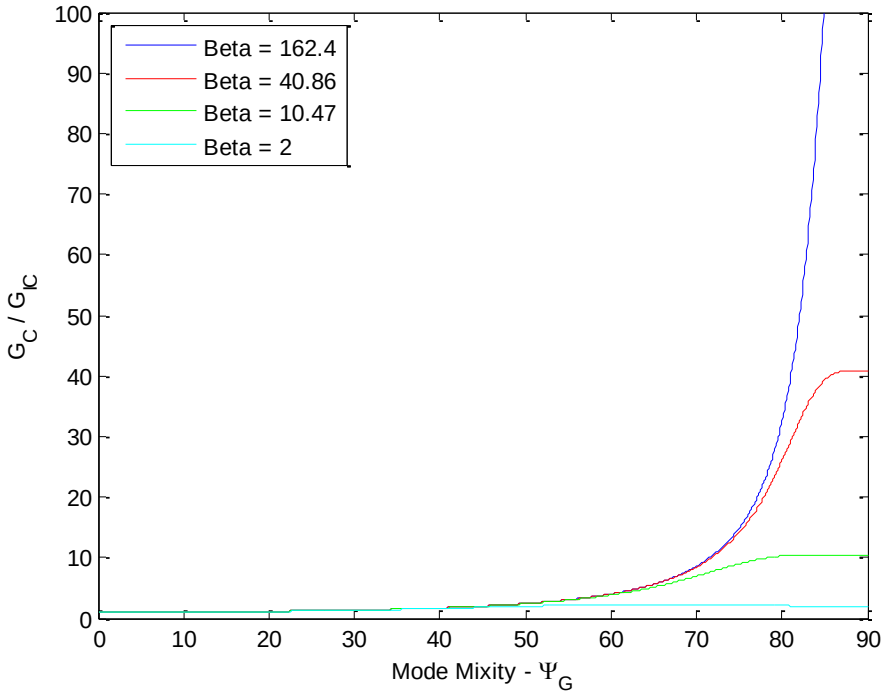

Figure 19 – G_C vs. ψ_G failure locus based on elliptical equation

Figure 20, Figure 21, and Figure 22 show the same normalized G_C / G_{IC} curves as in Figure 18 and Figure 19 but for single cases where the G_C / G_{IC} value at ψ_G = 0° and ψ_G = 90° are equivalent for both the elliptical and the Hutchinson and Suo models. As can be seen in Figure 21 and Figure 22 the error between the two models for the λ = 0.05, β = 162.4 case across the ψ_G range is minor as long as ψ_G < 60.° In comparison, for the λ = 0.5, β = 2 case, the error between the two models is significant across almost the entire range, only diminishing below ψ_G = 5.°

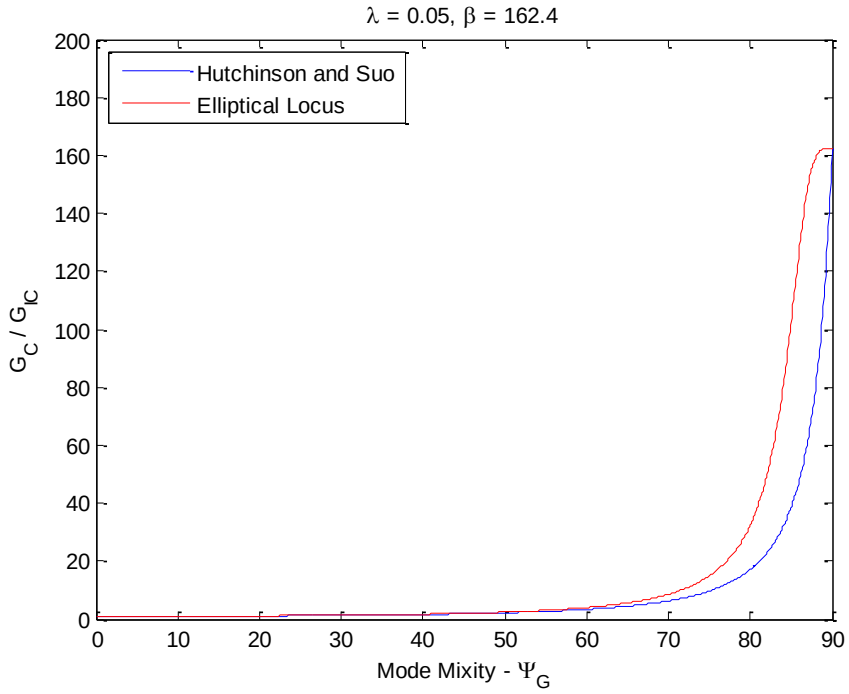

Figure 20 - Failure Locus Comparison: Low λ

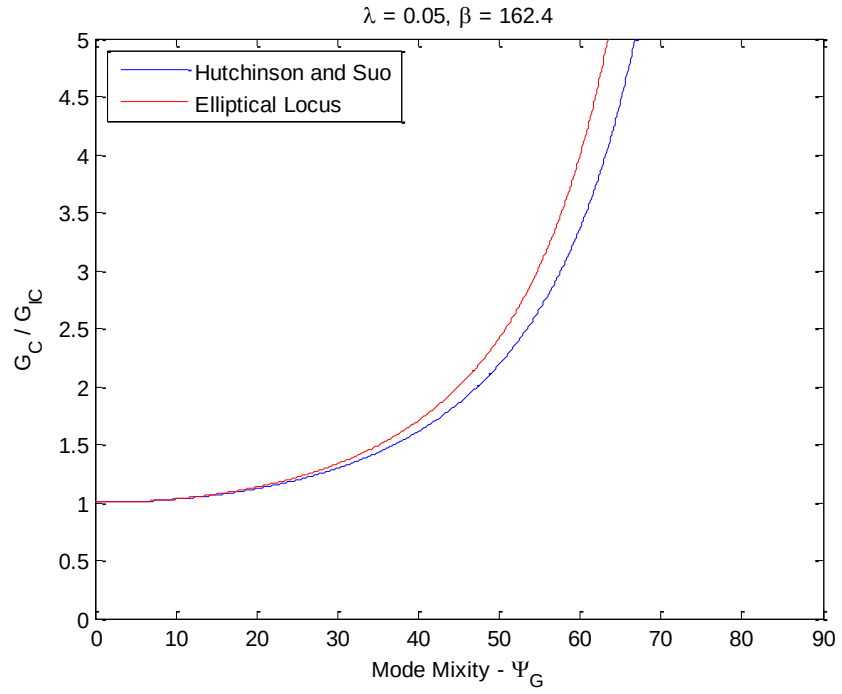

Figure 21 - Failure Locus Comparison: Low λ Zoomed

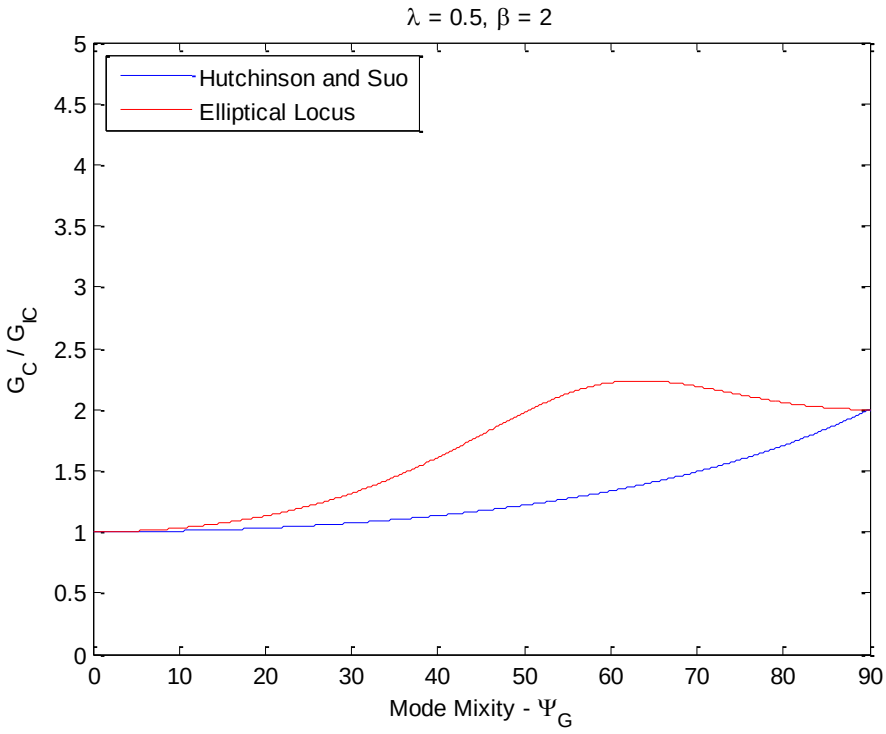

Figure 22 - Failure Locus Comparison: High λ

For the test data reported in this work a comparison of the elliptical and Hutchinson and Suo mathematical forms used to fit the parameters is shown in Figure 23.

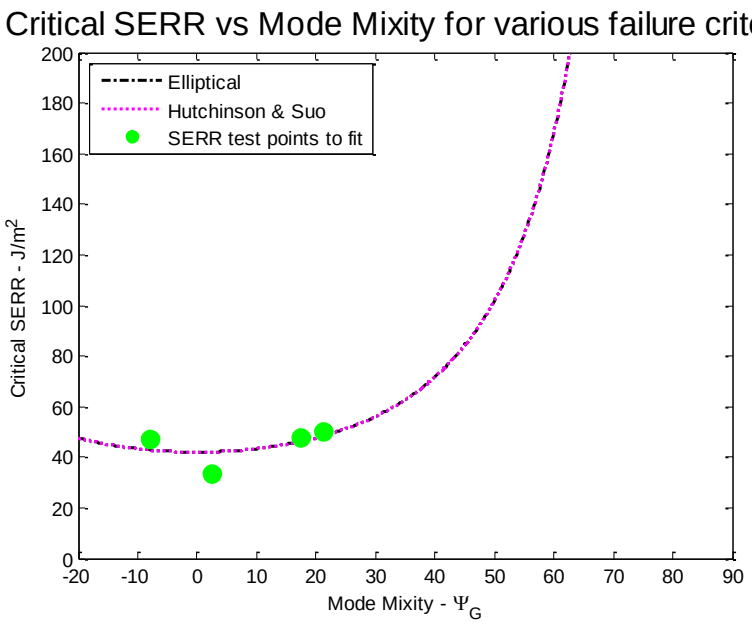

Figure 23 - Mathematical Forms of Mode-Mixity

As can be seen, the difference between the Hutchinson and Suo [33] equation, an elliptical energy failure locus are nearly negligible for our collected data. In this case the λ value is nearly zero while the β value was approximately 2000. The linear form (not shown) is also similarly indistinguishable. While these λ and β values are somewhat extreme they are the result of the limited range of mode-mixity datapoints used to generate the fits. Different values of λ and β would not result in appreciably worse fits within the region of experimental data due to the lower sensitivity of the curves at low mode mixities. The addition of a higher mode-mixity datapoint would introduce the potential for different behavior of the two models however.

It is also important to recall that the highest mode-mixity datapoint is limited to close to this presented range as a result of LEFM assumptions becoming invalid due to significant yielding at higher mode-mixites. In other cases such as for end notch flexure, the testing may fail with a crack kinking directly into the bulk material (EMC) and

inducing bulk fracture rather than delamination. As a result, for the bimaterial under study it may not be possible to achieve a high mixed mode delamination condition local to the crack tip in any case were LEFM applies. In addition to establishing a failure criterion for a bimaterial interface, it is also worth considering whether an additional parameter, the maximum feasible mode-mixity, should also be defined and reported. This consideration is of practical importance to investigators as it may better define the appropriate scope of tests to be performed when the characterization of an interface is desirable.

Another point worth noting is that Equation 13 forces $G_{IIC} > G_{IC}$. While this is an expected condition for most materials it is artificially forced by the form of the equation used. The elliptical failure criterion mathematically can be formulated where mode II fracture toughness is lower than that of mode I. This exotic case is supported by the form of equation 20. For copper / epoxy molding compound interfaces G_{IIC} / G_{IC} ratios have been reported to range from five [45] to around ten [4] with higher ratios typically expected. It is worth noting that some similar interfaces have been observed to be as low as two [34].

Whatever form used in the FEA cohesive-zone routines to establish a failure locus must be consistent with the equation used to fit the required parameters. Whether the existing FEA elliptical and linear failure criteria are accurate, or if a Hutchinson and Suo failure criterion needs to be utilized in FEA, is dependent on the real experimental results at higher mode mixites; conditions which may for the bimaterial under study be unreachable. Charalambides discusses some of the possible mathematical forms of these relationships at length [34]. The ANSYS mathematics from Alfano and Crisfield, which

agree with either a linear or elliptical energy failure criterion are distinct from the Hutchinson and Suo form. This results in a mathematical incompatibility and is fundamentally inconsistent.

It is worth noting that there has not been a deluge of inaccurate CZM models resulting from this inconsistency. The reason for this lack of observed error is that within the range of mode-mixites typically experienced, the difference in values between the various mathematical forms under use is relatively small. In order to maintain correctness and the potential for some level of extrapolative predictability, this inconsistency should not be overlooked.

3.9 Conclusions

The critical strain energy release rate of a copper / EMC bimaterial interface has been demonstrated to be a function of mode-mixity through DCB tests of different sample thicknesses and 4PB tests. An additional test, DMMB was attempted but produced invalid results due to significant plasticity. The ability to test the studied interface at higher mode-mixites through standard test geometries was further hindered by the tendency of the crack to kink into the bulk materials. A practical upper limit to mixed mode fracture may exist though this will dependent on the materials and process history of the interface itself.

The mathematical inconsistency between the typically reported Hutchinson and Suo forms and the relationships defined in ANSYS CZM routines has been determined unlikely to manifest as the dominant deleterious aspect of CZM modeling due to low error at low mode-mixity. Despite the relatively low error consistency between the

experimental datafit and CZM implementation should still be maintained. Without such consistency CZM can confidently be asserted only valid within ranges of demonstrated accuracy. Such accuracy must still be demonstrated when attempts are made to extrapolate outside of the confirmed correlated range but only with mathematical consistency maintained does the possibility exist for accuracy for extrapolated fits.

The question of what the mathematical form should be requires investigation of the failure surfaces themselves and a linkage between the underlying failure micromechanics and the derived mathematical forms.

CHAPTER 4. A FATIGUE CRACK PROPAGATION MODEL WITH RESISTANCE CURVE EFFECTS FOR AN EPOXY/COPPER INTERFACE

***Abstract* —** Fatigue crack propagation for copper/epoxy molding compound interfaces is modeled in this work by conducting cyclic loading on double cantilever beam test specimens. The continued increase in mechanical compliance of test specimens as the crack propagates through hundreds of cycles is used to determine the crack length and thus, the crack growth rate per cycle which is used to determine the Paris' law constants as a function of strain energy release rate range. When monotonic debonding testing is conducted, it is seen that the critical strain energy release rate initially increases with the crack length and then stabilizes demonstrating the increasing resistance for the epoxy/copper interface. When such an increasing R-curve is used to normalize the strain energy release rate range, it is observed that the Paris' law constants can be determined with good consistency for a wide range of specimens over different crack lengths.

4.1 Contextualization Notes Regarding Fit into the Overall Work

Chapter 3 reported on the results for interfacial adhesion strength testing of a bimaterial interface under several mode-mixity conditions. The monotonic test results of Chapter 3 are a required preliminary task in support of the study of interfacial fatigue but not however, the main focus. This chapter outlines the development of an experimental methodology to study bimaterial interfacial fatigue at the microelectronic packaging length scale and a convenient analytical model to be used to generate the affiliated Paris Laws. 3D traditional LEFM ANSYS simulations were used to validate the analytical form proposed.

The work contained in this chapter was published in Engineering Fracture Mechanics in July of 2017 [38].

4.2 Introduction

Interfacial fracture is a common failure mechanism for microelectronic packages. The mismatches of coefficients of thermal expansion of the constituent materials results in residual thermal stresses arising from temperature changes. Additionally, cyclic thermo-mechanical loads result from device operation and contribute fatigue loading conditions. As a driver of device reliability, interfacial delamination has been the focus of study for both monotonic [4, 23, 24] and fatigue [17, 25-28, 30] loadings for various material pairings. Characterization of the effects of both thermal and moisture exposure [31, 32] is also an area of interest but will not be considered within this work. Long-term

exposure under both thermal and moisture conditions typically results in a reduction of adhesion strength. Long-term exposure studies should also chemically inspect changes in the interfacial surfaces with methods such as X-Ray Photoelectron Spectroscopy (XPS) to correlate the changes induced by exposure to the adhesion mechanisms themselves and subsequently the associated adhesion strength. The push for higher performance at lower power requirement and cost ensures that further miniaturization of microelectronic packages remains an industry focus. Ever thinner layers and increasing numbers of material interfaces ensures that understanding these interfaces and accurate characterization of them remain of the utmost importance.

The double cantilever beam (DCB) test is extremely popular for the determination of interfacial fracture toughness. Linear-elastic fracture mechanics (LEFM) principles are applied and used to measure the energy dissipated per unit area of crack growth, otherwise known as the strain energy release rate (SERR) G. DCB testing is popular due to its relative simplicity. The force data which must be gathered is very simple to obtain but traditionally DCB tests require the observational measurement of the growing interfacial crack. Liberation from the requirement of observational measurements of crack length is needed to enable the reasonable characterization of smaller test samples. These smaller samples are closer in scale to the eventual design features where failures are expected and to be studied. This need has been noted by other researchers as well [12]. The ability to determine sub-micron incremental crack growth without the use of expensive microscopy methods is essential towards fatigue characterization of these interfaces at scales pertinent to microelectronics.

Whether for monotonic delamination or fatigue crack propagation, the following information is needed: force measurement data, sample crack length, and an analytical model to calculate the SERR. There has been much study towards establishment of accurate SERR analytical forms[3]. De Gracia, Williams [46, 47], Olsson [48], Shokrieh [49] and others have explored various theoretical formulations to account for numerous deviations from ideal beam theory in the calculation of G_c. Compliance-based methods can be used to calculate crack length [44, 50] however relating compliance to crack length simply by a cube root relationship will fail to capture any physics not represented within simple beam theory such as fixture effects. One option is to apply a third order polynomial to the gathered crack length and compliance data as done by Krieger [51]. Results determined from proposed analytical forms are commonly compared to those from finite element analysis (FEA) models for accuracy.

The aim of this work is to utilize compliance-based approaches for the determination of crack length towards the calculation of both monotonic fracture resistance curves and the establishment of normalized fatigue crack propagation Paris-Erdogan laws. Compliance-based approaches have been shown to agree well with measurements [18, 52] and unlike visual measurements are not susceptible to difficulties in determining the location of the crack tip at small scales.

Accuracy will be determined through the comparison of analytical results to a 3D double cantilever beam model in ANSYS. Although the crack front will be modeled as linear as opposed to crescent shaped [50, 53, 54]this should not present problematic errors in the determination of the Paris' law as the calculated crack lengths are equivalent lengths based upon a total compliance. The subsequent normalization of crack

propagation data by the critical SERR for the determination of collapsed Paris' law will offset any errors caused by the assumption of a straight crack front. Additionally, the existence of a copper flange for the test samples prevents the existence of a planar free surface at the edges of the crack front which greatly reduces the SERR widthwise variation.

4.3 Experimental Setup

Bimaterial double cantilever beam (DCB) samples are fabricated by flowing epoxy molding compound over copper leadframe. Prior to testing, the samples are pre-cracked by applying force on the free end of the copper to delaminate it from the epoxy molding compound (EMC). Clamping down on the specimen arrests the crack and prevents the sample from fully delaminating. Aluminum fixtures are subsequently bonded to the pre-cracked end of the sample with an epoxy adhesive. Figure 24 shows both a photo and a schematic of the test sample. Testing is performed both monotonically and cyclically on a Delaminator Adhesion Testing System as illustrated in Figure 25.

4.4 Monotonic Experimental Evaluation

Monotonic delamination tests and critical SERR characterization was performed. Samples were loaded until a maximum (critical) load was reached after which the load decreases as the interfacial crack propagates. Intermittently, the displacement controlled test was reversed which stopped the propagation of the crack and unloaded the sample. The sample was then re-loaded to a new critical load at a new crack length at which point the crack propagated again. Figure 30 shows monotonic testing load vs. position results for a sample analyzed for a wide range of crack lengths. Crack lengths are determined by

applying a compliance to crack length relationship, which has been established from numerical models. Per best practices, compliance is calculated from the unloading slope of the load vs. position graph. For a given test sample the critical SERR can be determined for any crack length and critical load pairing. The critical SERR results from the different numerical and analytical modeling approaches were compared to establish confidence, and the accuracy of the model to be chosen for subsequent fatigue analysis.

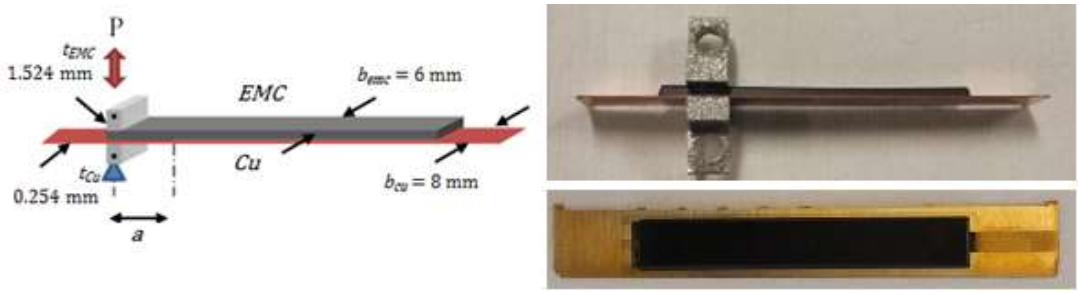

Figure 24 - Schematic and Images of DCB Sample

To test the effectiveness of the compliance based method for the determination of crack length, a DCB test was performed while taking side profile pictures with a Depstech™ borescope at the beginning of each unload transient. These images are shown in Figure 26. By using the fixture length dimension measured by calipers as a reference scale, the crack observed crack length can be measured. A comparison of compliance based crack lengths to these observed lengths is shown in Table 7. The differences between the two methods is less than 3% and demonstrates that compliance based crack lengths can be accurately utilized.

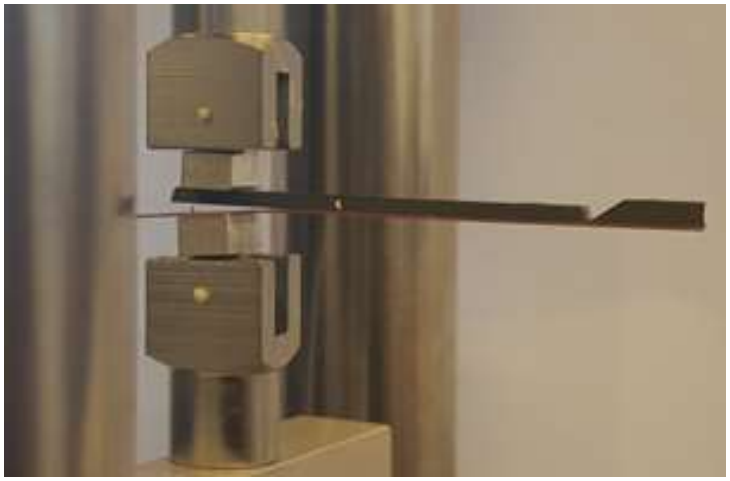

Figure 25 - Delaminator Adhesion Testing System

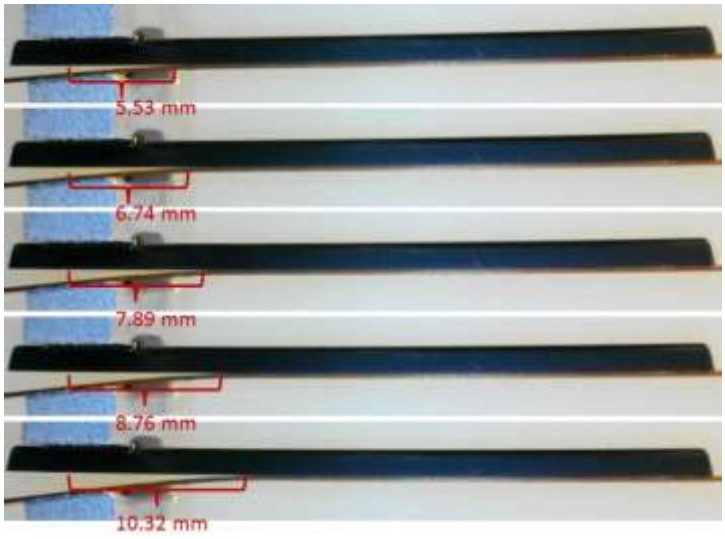

Figure 26 - Optically Measured Crack Growth

Table 7 - Observed vs. Compliance Based Crack Lengths

Unload Curve	Crack Length Measured Optically (mm)	Crack Length Determined from Compliance (mm)
1	**5.53**	**5.4**
2	**6.74**	**6.6**
3	**7.89**	**7.84**
4	**8.76**	**8.75**
5	**10.32**	**10.55**

4.4.1 Numerical Model

Under certain conditions and geometries, both analytical and numerical 2D methods for determining interfacial strength may yield accurate results. The bimaterial double cantilever beam test samples are composed of an epoxy compound molded upon copper leadframe. Unlike those of a typical DCB test, the samples lack a uniform cross section due to the leadframe width exceeding the epoxy molding compound (EMC) width. As a result the compliance behavior for any 2D model will differ from those of the 3D model and experimental results. Additionally the presence of the greater width of the copper flange prevents the existence of a planar free surface at edge of the crack

front. For these reasons a 3D FEA model with widthwise half symmetry was used. Figure 28 shows σ_z with and without the flange geometry / a planar free surface and Figure 27 shows the resulting impact on widthwise SERR variation for an indicative case. The flange geometry is illustrated schematically in Figure 24.

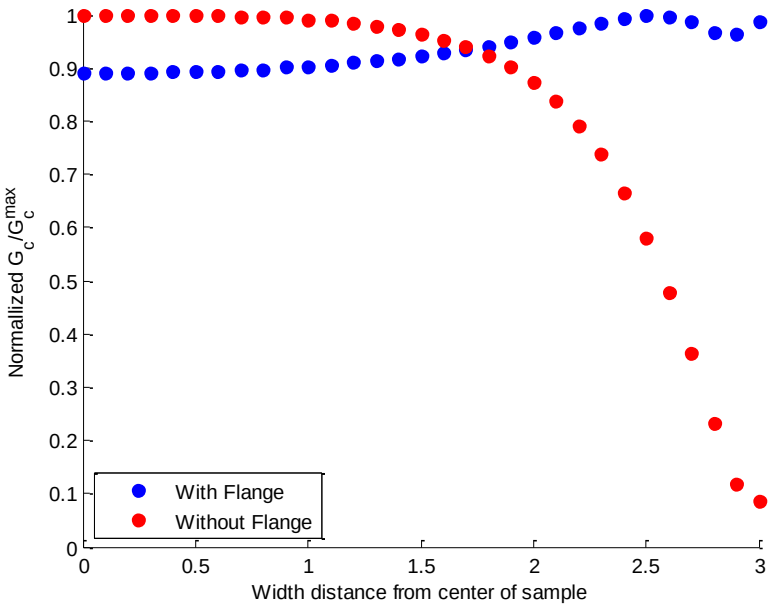

Figure 27 - Widthwise Variation of Normalized SERR (From the center of the sample to the edge of the EMC)

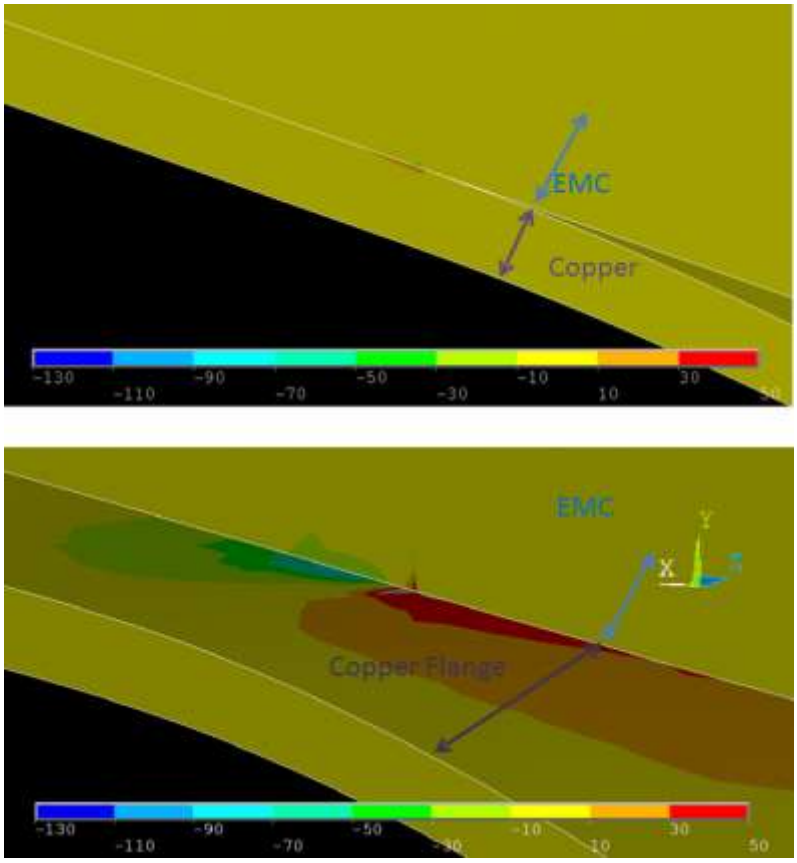

Figure 28 - Impact of Copper Flange

Given both the differing compliances and the flange effects, error is expected to exist for 2D models. To quantify the error simulations were run in both 2D and 3D comparing the resulting SERR values based upon the same experimental data. For the 2D model the sample width was assumed to be 6 mm, equal to the length of the bimateiral interface. For both the 2D and 3D simulations, compliance to crack length relationships specific to the modelled geometries were obtained from the models and used to calculate the crack length. Separate relationships are needed as the 2D and 3D models will not have the same compliance at a chosen crack length due to the absence of planar symmetry.

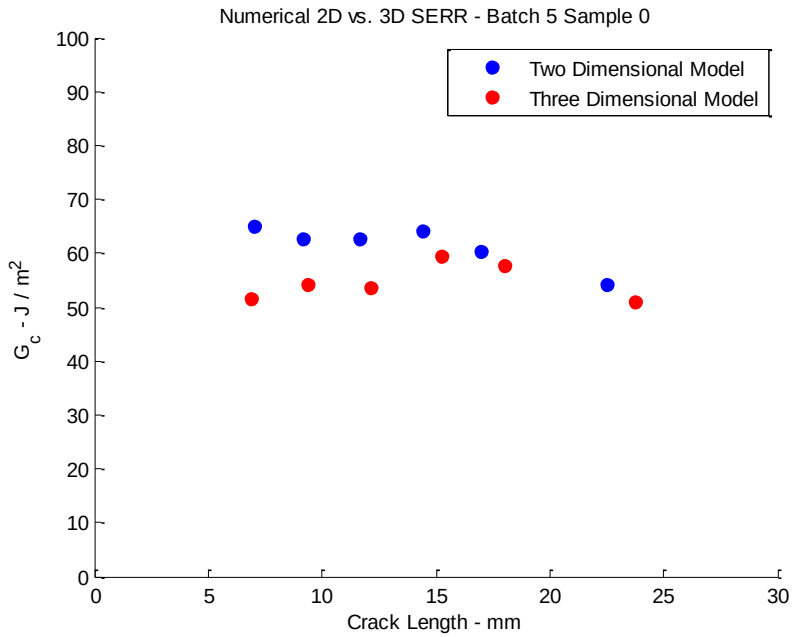

Figure 29 - 2D vs. 3D Numerical Model Comparison

For the purposes of comparison, the slight differences in calculated crack length can be ignored as any potential rising R-curve effects should be minimal for the differences in question. As shown in Figure 29 and Table 8 the difference between the 2D model and the 3D model can be over 25%. While the error decreases with increasing crack length, many of the applications of interest are for shorter crack length conditions. For this reason it was decided a 3D model was appropriate.

Table 8 - 2D vs. 3D Numerical Results

Load (N)	**4.01**	**3.04**	**2.37**	**1.97**	**1.63**	**1.17**
2D Crack Length (mm)	**7.01**	**9.14**	**11.62**	**14.44**	**16.94**	**2**
2D SERR (J/m^2)	**65.2**	**62.8**	**62.7**	**64.2**	**60.4**	**54.3**

3D Crack Length (mm)	**6.86**	**9.36**	**12.13**	**15.23**	**17.99**	**23.74**
3D SERR (J/m^2)	**51.7**	**54.1**	**53.6**	**59.6**	**57.7**	**51**
SERR Error (%)	**26.1**	**16.08**	**16.98**	**7.72**	**4.7**	**6.47**

Explanation of the 2D model results is as follows: The 2D model assumes a uniform cross section of 6 mm (the width of the EMC) and ignores the extra copper width (copper is 8 mm wide). This error results in an overestimation of the compliance of the overall structure and a resulting underestimation of the crack length compared to the true value. Alone this would cause the 2D model to underestimate G_c compared to the 3D model. In addition to the compliance versus crack length error, there is also an accompanying loading error. The dominant compliant structure carrying the displacement is the copper as the EMC is rigid in comparison. The unit width loading on the copper for each model is thus P/6 for the 2D model while P/8 for the 3D model. This means that the 2D model is loaded to a higher magnitude towards bending which results in an overestimation of G_c. When these two phenomena are combined the result is an initial overestimation of G_c at shorter crack lengths. This overestimation steadily decreases as the error caused by the higher effective load is counteracted by the increasing error caused by the difference in calculated crack lengths. This error cannot be corrected by changing the 2D model's load to P/8 as that would then imply the entire interface was 8mm thick inducing other similar errors.

Loading for the chosen 3D model, as for the experimental tests themselves, was applied to through aluminum pins which transfer loads to the sample through contact

surfaces. Figure 31 shows the ANSYS™ FEA model for an example loading condition. The FEA model crack length is determined using the inverse compliance method and set to the length corresponding to the known delamination max load measured during monotonic testing and loading the sample to that load value. Critical SERR is obtained from the built in ANSYS™ VCCT routine.

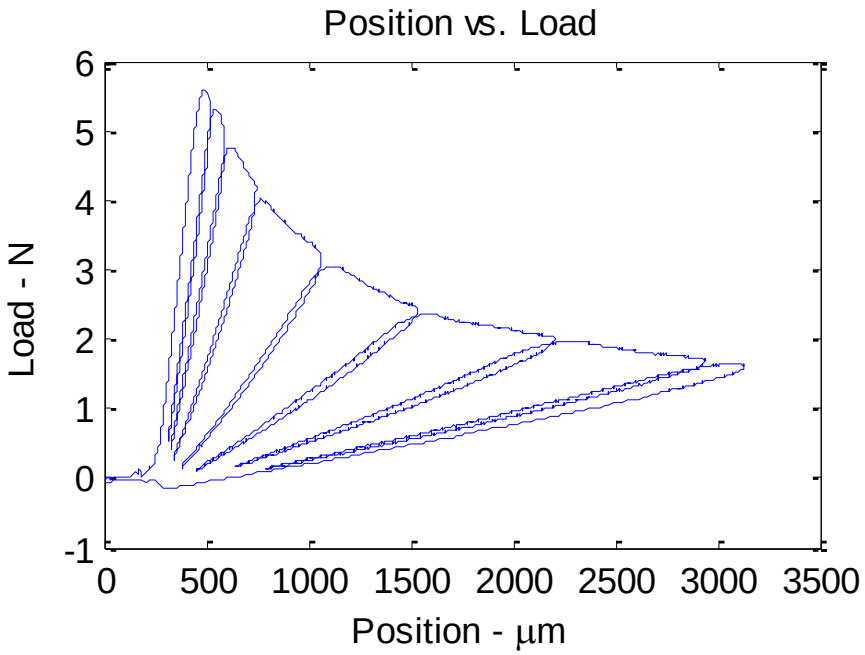

Figure 30 - DCB Load vs. Position

Figure 31 - Half Symmetric 3D DCB ANSYS Model

4.4.2 Analytical Model

Determination of Crack Length

For monotonic testing, both crack length and compliance can be calculated not only for the instances and crack lengths defined by the unloading slope compliances but during the delamination process as well through the following method:

1. Crack length is calculated based upon the unloading compliance for each unload cycle and defined as the distance from the crack front to the center of the loading fixture. Crack lengths determined at these points have been validated as accurate through comparison to optically determined lengths as described Table 7.

2. For each load, delamination, and unload series of monotonic testing, high order polynomials are fit to the data, twice differentiated and then used to establish the range active delamination. This is needed as the crack front geometry is non-linear and results in a transient establishment of a fully developed crack front which causes both the loading and the unloading lines to be slightly non-linear just prior and subsequent respective to delamination. These non-linearities reflect non-uniform crack growth which should be captured and incorporated into the effective length calculation.
3. The instantaneous displacement is calculated for every load / position point pairing. For the beginning and end of each delamination cycle, the unloading slopes can be extrapolated and used to determine the *x*-axis intercept and subsequently the position offset from the origin. The transition from the initial offset to the final offset defined by the starting and final crack lengths for each delamination event is fit to an interpolation function. The interpolation function used is the sum of a cubic term and a linear term to correspond to the modeled physics defining the problem, in this case beam bending with shear effects as reflected in Equation 4.
4. All data is then adjusted versus the calculated instantaneous offset from step 3 which results in the determination of displacement from the position data.
5. Instantaneous change in compliance is calculated from load and displacement data by taking the forward difference of the compliance data. Compliance data is defined as the instantaneous displacement divided by the current load since all data points are now defined with respect to a consistent origin.

6. The sample compliance value is updated by adding the dC_{sys} value to the previous compliance.
7. A new crack length is calculated from the updated compliance and the compliance to crack length relationship. This allows the determination of crack length during delamination between subsequent unloading events.

4.4.2.1 SERR Analytical Model 1

Three different analytical methods were compared for the determination of critical strain energy release rate and the generation of the R-curves for the DCB bimaterial specimens. Soboyejo et. al. [4] derived a relationship for SERR through the use of superposition principles. This approach however assumes that the mode-mixity is effectively in a pure mode I condition and that one of the constituent beams of the DCB sample is sufficiently stiff as to be negligible towards compliance. As a result the analysis can be assumed equivalent to a single cantilever beam. As a result this analytical approach over-predicts critical SERR values. The Soboyejo formulation is shown in Equation 34 and can be solved with the determined crack lengths and measured load data.

$$G = \frac{6P^2a^2}{E_{EMC}b^2t_{EMC}^3}\left(1+\frac{1}{\beta_E\beta_H^3}\right); \qquad \beta_E = \frac{E_{Cu}}{E_{EMC}} \qquad \beta_H = \frac{t_{Cu}}{t_{EMC}} \qquad \textbf{34)}$$

4.4.2.2 SERR Analytical Method 2

The formulation of SERR by Irwin calculates the strain energy release rate from the magnitude of the loading and the differentiation of sample compliance with respect to

crack length relationship as shown in Equation 35. To use this method, dC_{sys}/da can be determined by differentiating the crack length to compliance relationship calculated from numerical solutions and evaluated at the current crack length for the entire test.

$$G = \frac{P^2}{2b}\frac{dC_{sys}}{da} \quad \textbf{35)}$$

4.4.2.3 SERR Analytical Method 3

The third analytical method for determining crack length is through the application of LEFM beam theory. De Gracia et al. performed an in depth derivation towards the application of multi-layer composite beams. The bimaterial DCB structures studied in this work however, are sufficiently defined by accounting for the shear forces and bending moments of both the EMC and the copper beams which make up the DCB sample. The displacement of the DCB is defined by Equation 36. Substitution into the definition of compliance results in Equation 37. By differentiating this equation with respect to crack length we obtain Equation 38 to calculate G. Figure 32 shows a comparison for an indicative sample of the three analytical methods postulated or inspired by Soboyejo, Irwin and De Gracia and compares them to the results obtained from the 3D ANSYS™ FEA model. Moving forward, results determined from the Soboyejo relationship will be referred to as "Method 1," results determined from tracking the change in compliance throughout the test and then evaluated with the Irwin definition of SERR will be referred to as "Method 2," and the beam theory method inspired by De Gracia will be referred to as "Method 3."

$$\delta = \frac{Pa^3}{3E_{f,cu}I_{cu}} + \frac{6Pa}{5\mu_{13,cu}A_{cu}} + \frac{Pa^3}{3E_{f,emc}I_{emc}} + \frac{6Pa}{5\mu_{13,emc}A_{emc}} \quad \textbf{36)}$$

$$C_{sys} = \frac{\delta}{P} = \frac{a^3}{3E_{f,cu}I_{cu}} + \frac{6a}{5\mu_{13,cu}A_{cu}} + \frac{a^3}{3E_{f,emc}I_{emc}} + \frac{6a}{5\mu_{13,emc}A_{emc}} \quad \textbf{37)}$$

$$G = \frac{P^2}{2b}\frac{dC_{sys}}{da} = \frac{P^2}{2b}\left(\frac{a^2}{E_{f,cu}I_{cu}} + \frac{6}{5\mu_{13,cu}A_{cu}} + \frac{a^2}{E_{f,emc}I_{emc}} + \frac{6}{5\mu_{13,emc}A_{emc}}\right) \quad \textbf{38)}$$

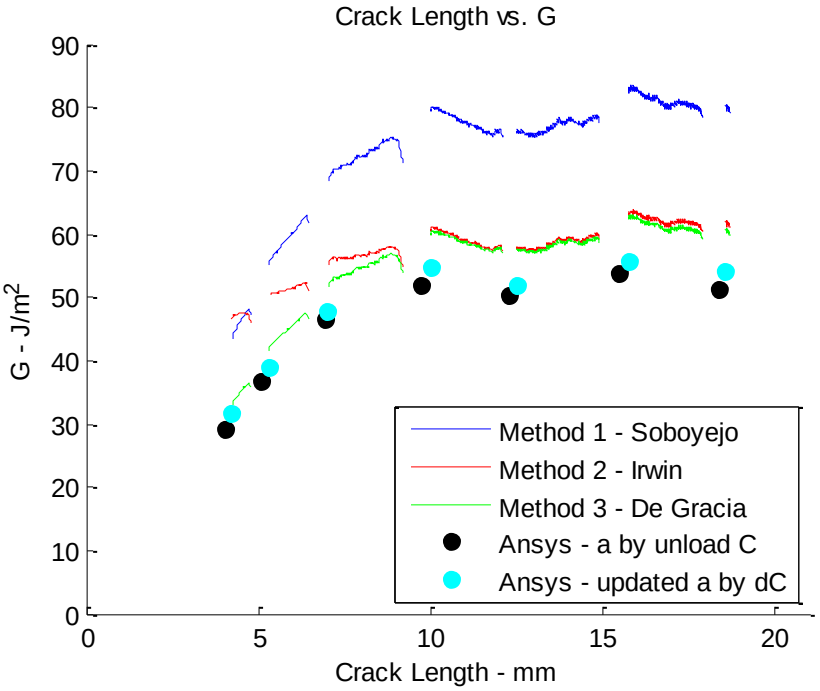

Figure 32 - Comparison of Analytical G Methods with 3D ANSYS FEA

Comparison of the methods

All three methods for determining G use the same crack length data as determined by the above algorithm. When compared to the ANSYS™ results, method 1 clearly overestimates G values and as such will not be used subsequently. Methods 2 and 3 are similar for most of the data but deviate from one another at shorter crack lengths. The

likely reason for this deviation is that pure beam bending is a poor assumption at extremely short crack lengths and that by modeling both the shear and the bending components as is done in method 3, much of the error associated with that poor assumption can be avoided.

It can be seen here that method 3 is most accurate and will be used in subsequent fatigue analysis. As shown in Figure 32 for an indicative test case, the error associated with method 3 is minimal at shorter crack lengths, increases with crack length before stabilizing. For Sample 0 the error associated with method 3 is approximately 10%. Discrepancy between the analytical forms described above and the 3D model are inevitable and unavoidable. Due to the lack of planar symmetry 2D analytical forms cannot capture all the effects present in the full 3D sample. In particular, while the interface being delaminated is 6 mm in width the dominantly compliant structure is the copper beam with a width of 8 mm due to its much smaller relative thickness to the EMC. As previously demonstrated such a structure cannot be modeled in 2D without error. The error in this case, however, is tolerable within the standards of fatigue as fatigue design principles routinely requires safety factors be considered by orders of magnitude rather than fractions due to the compounding effect of crack growth. Additionally, subsequent fatigue normalization methods will result in any errors associated with the analytical model choice being offset by the normalization factor which is determined from the same model.

Table 9 - Method 3 vs ANSYS SERR values

Pmax (N)	5.3	4.77	4.01	3.05	2.38	1.97	1.65
Crack Length (mm)	4.22	5.31	7.03	10	12.52	15.75	18.59
G ANSYS (J/m^2)	31.6	38.9	47.9	54.7	51.9	55.6	54.1
G Method 3 (J/m^2)	32.6	41.6	51.7	60.3	57.7	62.8	60.8
Error (%)	3.2	7	8	10.2	11.2	12.9	12.5

4.5 Determination of R-curves

Using analytical method 3, as described above, samples have been tested at various crack lengths to generate delamination resistance curves. These curves can be seen in Figure 33. The rising R-curve behavior observed for this data is common for DCB test specimens. The shape of the rising R-curve is determined by among other factors, the properties of the constituent materials and the size and geometry of the DCB test sample. Various mechanisms have been determined to be the cause of the rising R-curve behavior. For laminate composites, fiber bridging is a known cause of rising R-curve behavior [1, 50, 55, 56]. For ceramics and metals non-steady R-curves can result from numerous phenomena such as micro-cracking, stress shielding provided by the development of a steady crack tip wake of transformed material[57, 58]. Division of each sample's dataset by the steady state value allows the characterization of the R-curve shape free from the effects of sample to sample variation. Figure 34 shows normalized

R-curves for several samples. Both Figure 34 and Table 9 illustrate that the rising R-curve stabilizes and critical SERR values do not meaningfully change at crack lengths larger than 10 mm Fitting a polynomial to this data enables the determination of any sample's steady state G_C value without needing the sample's entire resistance curve, only its current length and that length's associated critical SERR. This capability is required for proper fatigue Paris' law normalization as the normalization factor which is set to the critical SERR G_C, is not constant.

4.6 Fatigue Testing

The Delaminator Adhesion Testing System is operated under displacement control. Samples are prepared per the same process as described for monotonic testing. Prior to cyclic loading, each sample is monotonically tested and the critical SERR calculated. This is done to capture the sample to sample variability in interfacial strength. Unloading of the final monotonic test point for each sample is done immediately upon reaching the maximum load to minimize any difference between the crack length for which the last monotonic critical SERR is known and the initial length for fatigue testing.

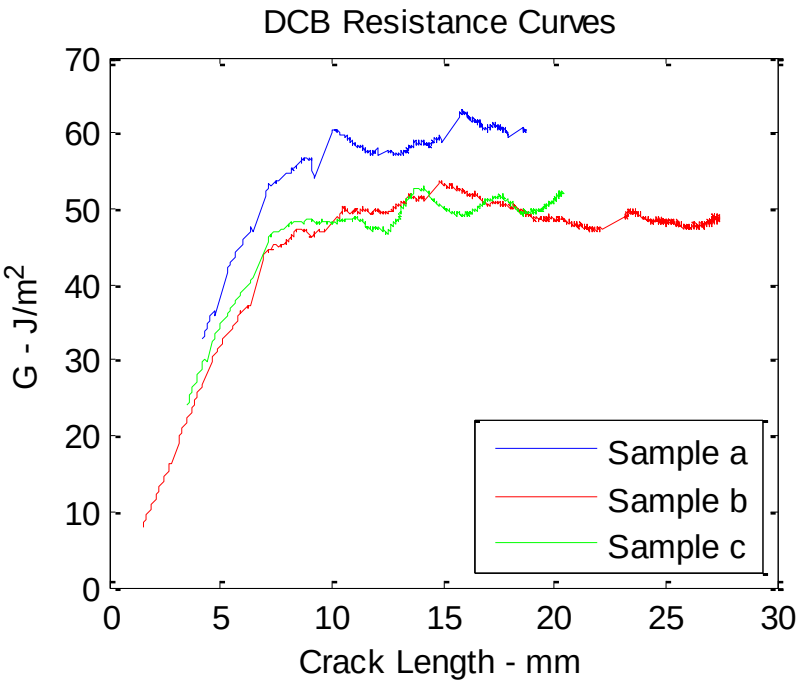

Figure 33 - DCB Resistance Curves

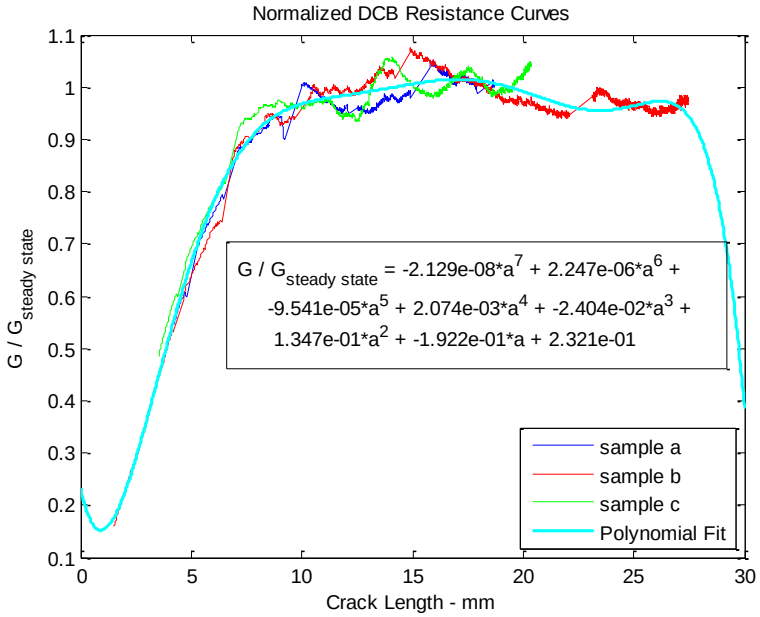

Figure 34 - Normalized DCB Resistance Curves

After completing the pre-fatigue critical SERR characterization, the test stand is re-homed to reduce any slack in the system. Samples are not removed from the test stand in between monotonic pre characterization and fatigue testing to ensure equivalence of results. The displacement is then chosen based upon the expected location where the critical SERR would be reached. The movement limits of the cyclic loading are then set to move from home (0) to a position corresponding to just below the initial expected critical load. Fatigue displacement control testing occurs at a rate of 5 μm/sec with dwell times of 3 seconds at maximum and minimum. The load ratio for this testing, R = 0. Over the duration of the test, the crack will incrementally propagate under fatigue and result in a corresponding decrease in the maximum load at the full extent of travel. As compliance increases with a cubic dependency vs. crack length, the reduction in maximum loads occurs at a greater rate than is needed to maintain a constant cyclic SERR (ΔG) throughout the test. For all tested samples, as the crack grows the maximum ΔG reached for each cycle decreases. As a result, displacement controlled testing allows the determination of crack propagation vs. ΔG load level across the entire range needed to generate a Paris' law relationship. An example of the load/position data unload paths is shown in Figure 35. For clarity, the data for each cycle in Figure 35 is assigned a unique color according to a color gradient progressing from red to blue. Tests are run for at least 2000 cycles for each sample. To ensure R-curve behavior has been successfully accounted for, samples are removed from the stand, monotonically delaminated further, re-characterized monotonically and tested cyclically for a second time.

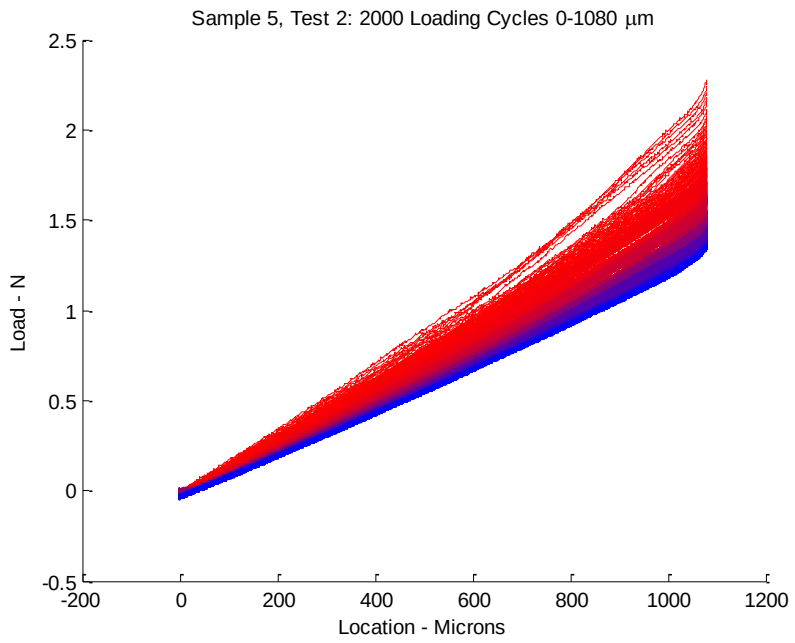

Figure 35 - Load vs. Position (Unloading Paths Only)

4.7 Determination of ΔG and Paris' Law

Load vs. Position data for all cycles is analyzed in Matlab®. Data is indexed cycle by cycle and only the data corresponding to the unload path near the end of each cycle's unloading step is used to determine sample compliance. From the compliance the crack length with then be determined. An example of the resulting crack length versus cycle is shown in Figure 36. With the crack length and maximum load for each cycle known, method 3 is used to calculate the applied SERR for each cycle as shown for the same sample used in Figure 35 in Figure 37. As can be seen in Figure 36 the experimental data is noisy and not ideally smooth. Taking the cycle to cycle data without additional consideration would imply there exist momentary events of crack length reduction rather than growth. As the crack is assumed to always increase in length, the data will be

subdivided into groups and averaged. The sizing of these groups will be chosen such that apparent momentary crack reduction is eliminated but the effective piecewise linear approximation does not fail to capture the overall curvature of the test data. Each grouping of data is then analyzed as follows: the ΔG values are averaged across the group and the fitted initial and final crack lengths are calculated. The crack propagation relationship data can be obtained by plotting ΔG vs da/dN in log-log space. The results are shown in Figure 38.

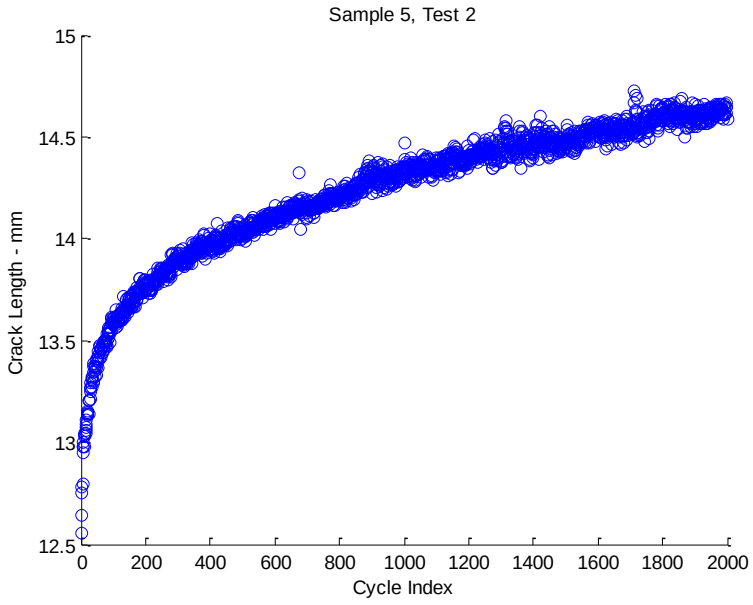

Figure 36 - Crack Length vs. Cycle Index

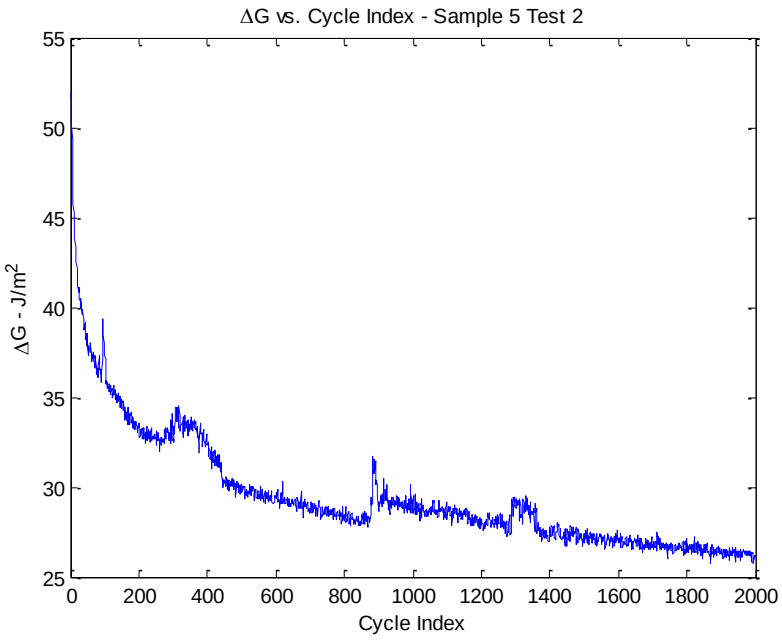

Figure 37 - ΔG vs. Cycle

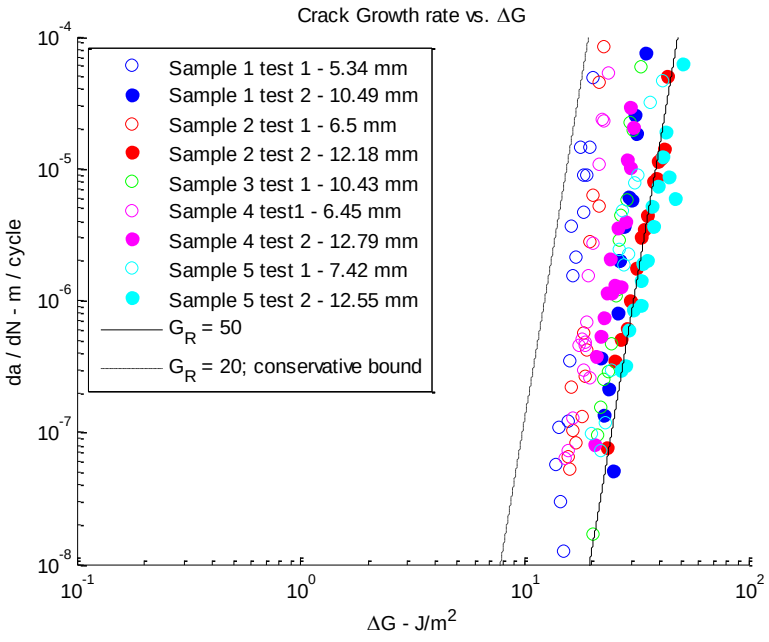

Figure 38 - Raw Paris' Law Data

Figure 38 presents the results for five samples tested at various lengths. Due to the impact of the rising R-curve on the raw data, Equation 39 does not result in a well-fit Paris' law.

$$da/_{dN} = C * \Delta G^m \quad \textbf{39)}$$

The sample and sample length dependency on the raw ΔG vs. da/dN relationships require a normalization method in order to collapse the data. By using the known pre-characterized critical SERR for each sample and the previously obtained R-curves, the data can be accurately normalized such that it collapses and is defined by a single law. Figure 39 shows the result of this normalization for all tests. It is worth noting that no outliers have been rejected in this analysis process despite indications from the test data that some tests resulted in superior data to others. The data and determined Paris' law presented here represent close to a "worst case" scenario for the used analysis method and is well within the expectations for the quality of fatigue test results. The normalized Paris-Erdogan law is listed in Equation 40. Normalizing the data by the R-curve increases the adjusted R^2 value for the fits of the entire datasets from 0.354 to 0.652 clearly indicating the superior of the fit.

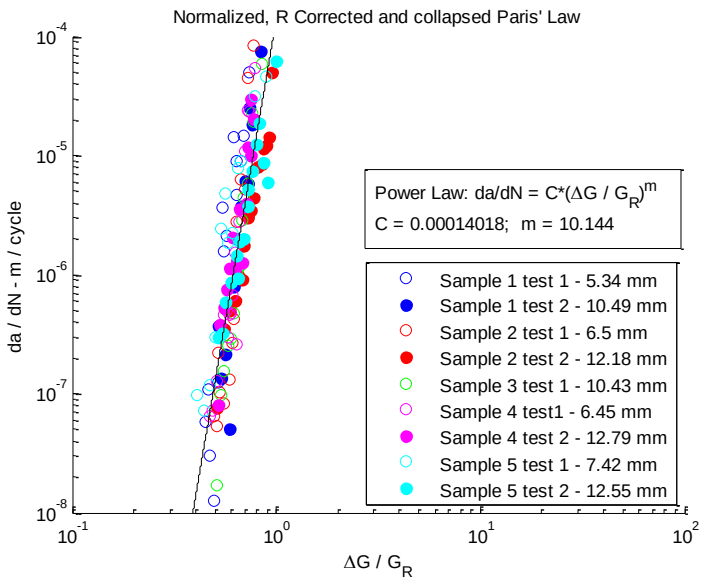

Figure 39 - Normalized and Collapsed Paris' Law Data

$$da/_{dN} = C * \left(\Delta G/_{G_R}\right)^m = 1.402 * 10^{-4} * \left(\Delta G/_{G_R}\right)^{10.144} \quad \textbf{40)}$$

If crack lengths are expected to be short enough for the rising R-curve behavior to be present, G_R can be evaluated as a function of the starting crack length and stabilized value per the polynomial shown in Figure 34. Including R-curve effects will decrease the critical SERR used for normalization and increase the degree of conservativeness of the model. If the preceding process yields a constant assumed G_R = 20 J/m^2 the model in Equation 40 can be represented in the form of Equation 39. This returns a conservative overestimation crack growth rates and encompass the data as shown in Equation 41 and illustrated in Figure 38.

For situations where the R-curve is expected to stabilize, a less conservative estimate can be obtained from the normalized law. For example, if the value for the

stabilized portion of the R-curve, G_R, is assumed to be 50 J/m^2 the typical Paris' law will be the one stated in Equation 42 below and illustrated in Figure 38.

$$da/_{dN} = C * \left(\Delta G/_{G_R}\right)^m = 8.89 * 10^{-18} * \Delta G^{10.144}\ Conservative\ Fit \quad \textbf{41)}$$

$$da/_{dN} = C * \left(\Delta G/_{G_R}\right)^m = 8.17 * 10^{-22} * \Delta G^{10.144}\ \text{R-curve stabilized fit} \quad \textbf{42)}$$

4.8 Summary and Conclusions

Asymmetric double cantilever beam testing has been performed on epoxy molding compound and copper leadframe bimaterial specimens. Testing was performed for smaller than usual samples which operate on the micron length scale similar to the design features the experimental results will be applied towards in design. As a result of the small size and non-uniform width of the specimens, assumptions such as the acceptability of 2D plain strain were inappropriate and led to the use of a full 3D FEA model for validation. Experimental and analytical approaches have been combined to allow the monitoring of crack growth without requiring observational measuring equipment with high financial and training barriers to entry. Monotonic testing has been performed and used to generate the resistance curves of the samples. The appropriateness and accuracy of various analytical forms were considered and the utilized analytical form was determined to be accurate to approximately 10%.

Cyclic fatigue tests were then performed and used to generate crack propagation data. Fatigue test data was used to generate Paris-Erdogan laws for each sample.

Monotonic pre-characterization test data was then used to normalize the Paris' laws and eliminate the influence of sample to sample variation. A collapsed, sample variation independent Paris' law was then determined from the entire dataset. The utility of such a law, through the R-curve and G_c normalization factors allows the determination of crack propagation properties for smaller structures where traditional sample size requirements are not applicable.

CHAPTER 5. FATIGUE CRACK PROPAGATION IN A COPPER/EPOXY MOLDING COMPOUND INTERFACE AS IMPACTED BY MODE-MIXITY

***Abstract* —** Microelectronic packages contain numerous bimaterial interfaces which influence both device design and reliability. The failure of these bimaterial interfaces have been observed to be a function of both the relative shear and tensile loads, otherwise referred to as "mode-mixity." While the failure of such bimaterial interfaces has been the focus of much study, their performance under fatigue, in particular with respect to mode-mixity, is underexplored. Double cantilever beam tests for a copper / epoxy molding compound interface have been performed for several different mode-mixity conditions, both monotonically and cyclically. The resulting Paris' laws are reported. In particular, the impact of mode-mixity on fatigue crack propagation is explored. The Paris' law coefficients and exponents have been seen to be dependent on mode-mixity. The mode-mixity dependency on fatigue behavior means that some of the properties of fatigue crack propagation can be determined from a bimaterial interfaces monotonic fracture behavior. Finally both numerical analysis in ANSYS and SEM surface characterization are performed to further the understanding of the mechanisms behind the observed trends in fatigue interfacial delamination propagation behavior as a function of mode-mixity.

5.1 Contextualization Notes Regarding Fit into the Overall Work

Chapter 3 explored monotonic critical SERR as a function of mode-mixity and further evaluated the appropriateness of different possible mathematical forms to fit the critical SERR to mode-mixity relationship. Chapter 4 built upon this monotonic work by further developing a methodology for the evaluation of fatigue crack growth. The methods outlined in chapter 4 however were performed under a single mode-mixity condition, that experienced by the nominal DCB bimaterial specimens. This chapter contains the work related to obtaining fatigue crack growth relationships, as characterized by the resulting Paris' laws for various mode-mixities. Furthermore, this chapter contains the exploration of possible inferable correlations between the mode-mixity and the fatigue crack growth behavior, and seeks to link these relationships with the underlying observed micromechanics as seen through SEM imaging.

At the time of this writing the work contained in this chapter was being submitted for publication in the Journal of Applied Physics D.

5.2 Background / Intro

Interfacial delamination is an important failure mechanism of study in order to support the design and manufacturing of microelectronic packages. Bimaterial interfaces are a near constant feature of modern microelectronics and have been the focus of significant interest. Much of the focus of these studies has been directed at monotonic failures [4, 23, 24, 51]. The reliability of these interfaces has also been studied under exposure to harsh conditions such as those provided by hot and humid environments. [31, 32] The failure of bimaterial interfaces under monotonic loads is reflective of possible

failures resulting from the thermal loads experienced during fabrication. The reliability of real devices however is influenced by the failure of these interfaces under fatigue loading conditions. Fatigue has been and continues to be an important area of focus for bimaterial interfaces. [17, 25-28, 30]

The experimental characterization of bimaterial interfaces such as the copper / epoxy molding compound interface, is necessary in order to create accurate and useful numerical models for use in microelectronic package design. To support improved design reliability of microelectronic packages containing bimaterial interfaces failure must be characterized across any experienced loading conditions, including both monotonic and especially fatigue. Incorporating fatigue results into a design tool such as a finite element analysis (FEA) simulation requires an understanding how fatigue failure behavior varies for different conditions. It has been well established that monotonic delamination of bimaterial interfaces is a function of the relative tensile and in plane shear loading conditions, or mode-mixity, local to the propagating crack tip. [33, 34, 59] Numerous modeling studies have explored how to best incorporate fatigue behavior into FEA models, in particular for models based on cohesive-zone model (CZM) [19, 21, 22, 60-64] and the extended finite element method (XFEM) [65, 66]. With regard to the dependency on mode-mixity, the existing experimental studies tend to focus on characterizing the threshold for which crack initiation occurs, rather than how the cracks propagate once initiated. [67-69]

The aim of this work is to explore the dependency of mode-mixity or ψ on fatigue crack propagation as reflected by the Paris' law constants. The interfacial strength will be determined experimentally through double cantilever beam (DCB) tests and calculated

both analytically and with numerical models. In order to vary the mode-mixity of the test, the DCB samples will be thinned to induce multiple different local mode-mixities resulting from the different geometric asymmetries. Additionally, the failure interface itself is explored through scanning electron microscopy (SEM) imaging.

5.3 Experimental

5.3.1 Double Cantilever Beam

Double cantilever beam test samples were fabricated for the copper / epoxy molding compound bimaterial interface by flowing the EMC onto a copper leadframe and then curing the bimaterial specimen. The copper width is 8 mm while the width of the EMC is 6 mm. The same sample production run was used to create test samples for three different mode-mixities. After sample production, the EMC layer was thinned from a nominal thickness of 1.524 mm to two additional different desired depths with a milling machine resulting in three different DCB test geometries for the same bimaterial interface. Sample pre-cracks are created by pressing downward on the free end of the copper to initiate delamination between the EMC and copper. The samples are clamped down upon to limit the extent of the pre-crack. Both monotonic pre-characterization of the interface and cyclic fatigue testing is performed on a Delaminator Adhesion Testing System as illustrated in Figure 40.

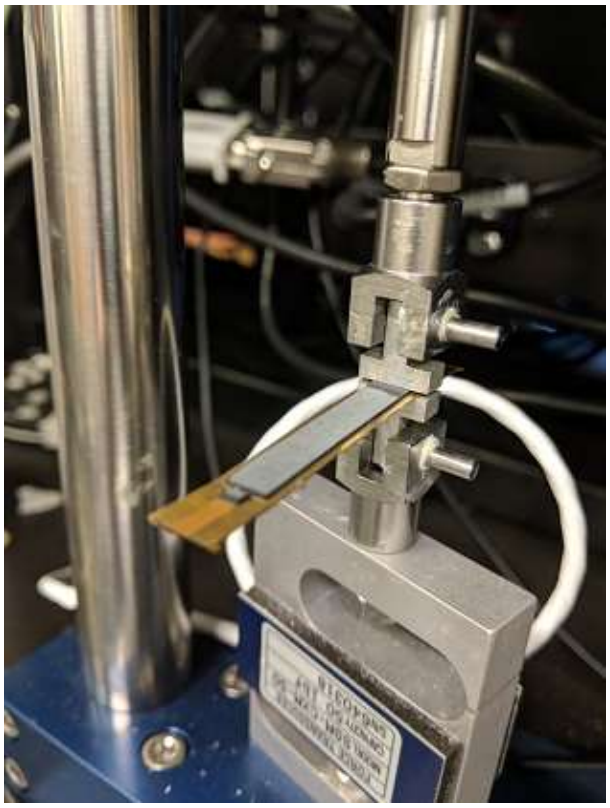

Figure 40 - Delaminator Adhesion Testing System

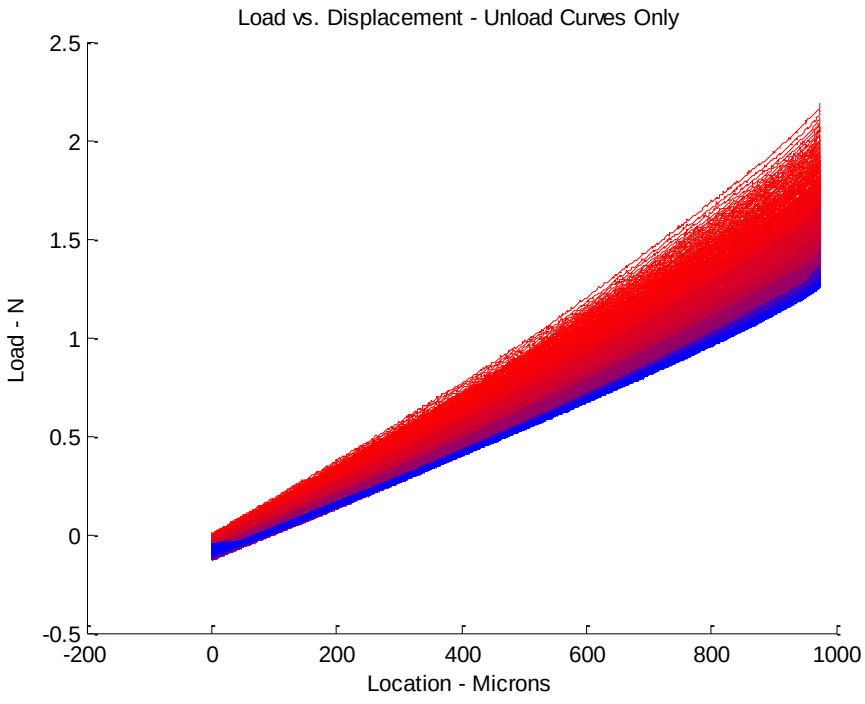

Figure 41 - Load vs. Displacement

Figure 41 shows the unload curves from an indicative fatigue crack propagation test. The unloading paths from thousands of load-unload cycles are plotted using a color gradient from red to blue. As the test progresses the compliance can be seen to increase as reflected by the changing slopes of the unload curves. The crack length can then subsequently be obtained from the measured compliances and incremental crack growth from the observed changes in compliance.

5.4 Analytical

5.4.1 Strain Energy Release Rate (SERR)

In work by De Gracia [3] formulations for the determination of bimaterial fracture resistance curves were presented with the capability of capturing rising R-curve behavior. The current authors have previously explored multiple different analytical formulations for determining the critical strain energy release rate, G_C. [38] Due to better accuracy when compared to 3D numerical models and the capability of capturing rising R-curve behavior, the formulations resulting from the approach suggested by De Gracia have been adapted towards the specifics of the tested specimens and are shown in Equations 43-45.

$$\delta = \frac{Pa^3}{3E_{f,cu}I_{cu}} + \frac{6Pa}{5\mu_{13,cu}A_{cu}} + \frac{Pa^3}{3E_{f,emc}I_{emc}} + \frac{6Pa}{5\mu_{13,emc}A_{emc}} \quad \textbf{43)}$$

$$C_{sys} = \frac{\delta}{P} = \frac{a^3}{3E_{f,cu}I_{cu}} + \frac{6a}{5\mu_{13,cu}A_{cu}} + \frac{a^3}{3E_{f,emc}I_{emc}} + \frac{6a}{5\mu_{13,emc}A_{emc}} \quad \textbf{44)}$$

$$G = \frac{P^2}{2b}\frac{dC_{sys}}{da} = \frac{P^2}{2b}\left(\frac{a^2}{E_{f,cu}I_{cu}} + \frac{6}{5\mu_{13,cu}A_{cu}} + \frac{a^2}{E_{f,emc}I_{emc}} + \frac{6}{5\mu_{13,emc}A_{emc}}\right) \quad \textbf{45)}$$

Due to the relative complexity of the test sample geometries local crack tip mode-mixity will only be determined numerically.

5.5 Numerical

Similar to previous work [38] numerical models were created in ANSYS to calculate both G_C and ψ. Similar to previous work, full 3D models were created. Copper was modeled with a bilinear kinematic hardening elastic-plastic material model and the epoxy molding compound was modeled as an elastic material. All materials were assumed isotropic. Process-induced thermo-mechanical stresses were determined by cooling the entire structure from the cure temperature to room temperature and accounting for the coefficient of thermal expansion (CTE) mismatch of Cu and mold compound. Additionally, cure shrinkage effects were incorporated by adjusting the stress free temperature of the molding compound. Symmetry was implemented to reduce computation time as appropriate. Loading was applied through contact surfaces which recreated the loading pins used during the actual experimental tests. A 50 μm element size was used near the crack tip and transitioned to a coarser mesh away from the regions of interest. For additional details on material properties as well as modeling details, the readers are referred to Samet et al. [38].

5.5.1 Critical SERR

Two different numerical methods are available in ANSYS for the calculation of SERR; the Virtual Crack Closure Technique (VCCT) and J-Integral. Rybicki and Kanninen [70] established the forms for VCCT which assumes self-similar crack growth. VCCT determines G_C by assuming that the energy required to close a crack is the same as that required to create it. With this assumption crack tip opening displacements are used to determine SERR. Rice proposed the J-Integral technique which uses a domain integral to calculate SERR.

5.5.2 Mode-Mixity

Mode-mixity must be calculated manually as ANSYS does not provide an automated routine to determine mode-mixity. Two methods to calculate mode-mixity are a displacement-based method, suggested by Matos et al. [42] and an SERR-based method. If implemented correctly, both methods yield equivalent but phase offset results. This shift in resulting dataset is due to the displacement based method utilizing an arbitrary reference length. In this paper, mode-mixity (ψ_G) will be reported using the SERR-based method. This is because the minimum SERR occurs when ψ_G is near 0°, which is consistent with the concept that cracks propagate most favorably under pure tensile loading conditions.

5.6 Results

As described in previous work by the authors, [38], a Paris law can be determined for the bimaterial interface through compliance-based analysis of displacement-controlled fatigue tests. Tests are conducted for fully unloaded (R=0) conditions. Normalization of the test results by each individual samples monotonic critical SERR collapses the

datasets. Tests for samples of three different thicknesses were conducted and both the monotonic and fatigue test results are presented. For each sample set of different EMC thickness, samples are tested at two different crack lengths where possible.

5.6.1 Monotonic

The monotonic test results shown in Table 10, Table 11, and Table 12 report the final critical SERR result determined before the sample was unloaded in preparation for the fatigue tests. Tests samples are labeled as sets S (standard), T (thinned), and V (very thin) which refer to the EMC sample thicknesses of the nominal 1.524 mm, thinned to 0.774 mm and thinned to 0.552 mm respectively. The pre-fatigue monotonic results will be used to normalize the fatigue test results and generate Paris' law curves.

Table 10 - Monotonic SERR Results: Nominal Samples

Nominal 1.524 mm thick EMC	Crack Length (mm)	Analytical Critical SERR (J/m^2)	Numerical Critical SERR (J/m^2)
S1	5.22	24.4	23.0
S1 test 2	10.5	47.7	37.3
S2	6.50	26.8	23.7
S2 test 2	12.2	47.7	41.2
S3	10.4	39.7	35.4
S4	6.45	29.4	30.0
S4 test 2	12.6	42.1	39.5
S5	7.52	47.9	42.7
S5 test 2	12.2	57.9	50.3

Table 10 shows five samples with at least four of the samples tested with two crack lengths. As seen, the critical SERR is greater for greater crack lengths. In other words, these samples demonstrate a rising resistance curve. This rising R-curve behavior is likely the result from the greater impact of shear effects for shorter crack lengths. This only arises for the nominal thickness samples as they are the only samples thick enough for the relatively lower aspect ratio of the samples to cause non-negligible deviation in behavior from that of an idealized simple beam. Both sample-to-sample variation and the presence of a rising R-curve means the best way to interpret the dataset is through the shape of a normalized R-curve. As a result, straight SERR averages are not highlighted. Previous work by the authors reported for an equivalent dataset of the same batch of samples SERR averages of 54.0 J/m^2 and 47.7 J/m^2 analytically and numerically respectively.

The thinned EMC samples of the "T" and "V" sets displayed no rising R-curve behavior and returned very consistent results as shown in Table 11 and Table 12, respectively.

Table 11 - Monotonic SERR Results: "T" Samples

Thinned 0.774 mm thick EMC	Analytical SERR (J/m^2)	Numerical SERR (J/m^2)	Length (mm)
T1	33.6	30.5	5.51
T1 test 2	40.0	35.3	8.69
T2	36.0	32.1	7.02
T2 test 2	38.7	34.2	14.0
T3	38.2	35.1	5.32
T3 test 2	37.4	33.5	7.86
T4	36.7	32.7	6.82

T4 test 2	37.4	33.1	9.18
T5	40.0	36.5	6.96
T5 test 2	38.7	34.1	9.36
T6	37.1	33.7	6.14
T6 test 2	37.7	33.6	8.88
Average	**37.6**	**33.7**	

Table 12 - Monotonic SERR Results: "V" Samples

Thinned 0.554 mm thick EMC	Analytical SERR (J/m^2)	Numerical SERR (J/m^2)	Length (mm)
V1	47.5	41.2	6.90
V2	53.2	51.6	5.80
V3	58.2	53.3	5.00
V4	52.0	46.5	9.15
V5	49.2	43.6	9.92
V6	54.6	48.7	8.80
Average	**52.5**	**47.5**	

The nominal thickness samples were found to be distinct in that they presented a rising R-curve behavior whereas the thinned samples did not.

5.6.2 Fatigue

In previous work [38] the authors presented a compliance based approach towards the generation of a normalized Paris law. The methods in that work have been followed in generating Paris' laws for each of the three different thicknesses and thus three different mode-mixity conditions. The rising R-curves require that the results be normalized by the monotonic critical SERR prior to determining the Paris' law for the collapsed dataset. For the nominal test samples with an EMC thickness of 1.524 mm the raw crack propagation results are shown in Figure 42 while the collapsed dataset can be

seen in Figure 43 with the corresponding derived Paris' law. Both figures were adapted from those published in [38] with permission.

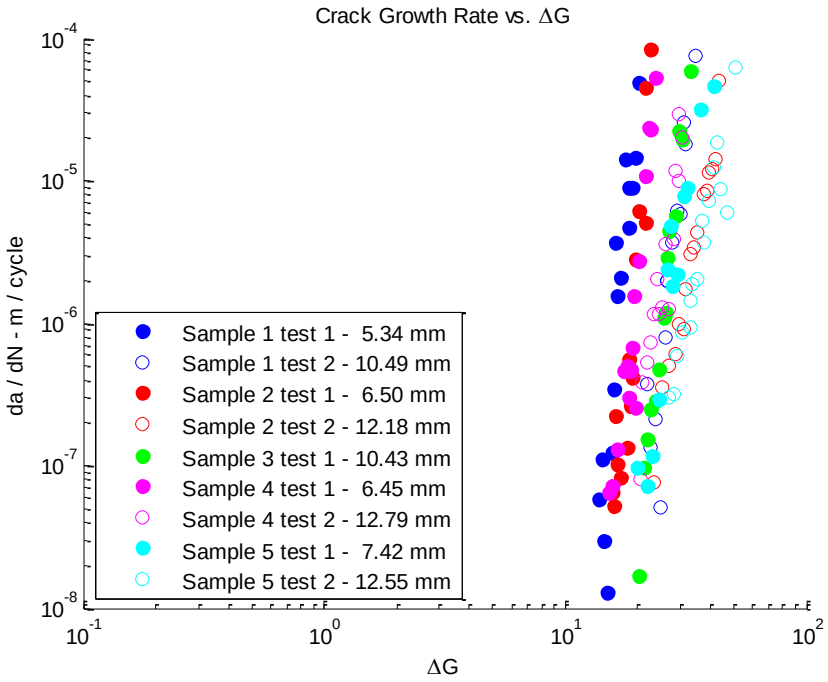

Figure 42 - Raw Paris' Law Data: Nominal Samples

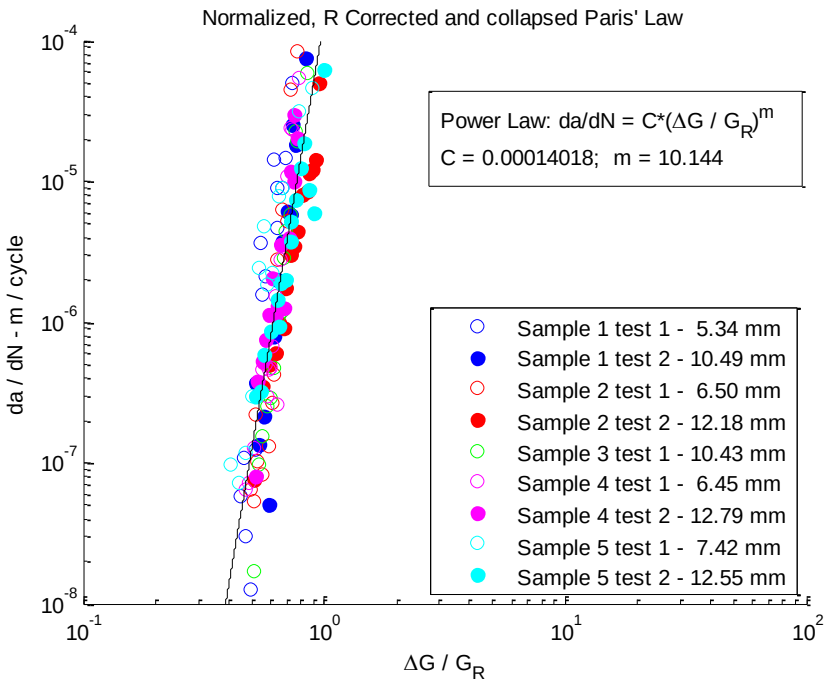

Figure 43 - Normalized Paris' Law Data: Nominal Samples

As discussed for the monotonic test results, no rising R-curve behavior was observed for the thinned "T" or "V" samples. Due to this, the results are consistent such that a Paris' law can be fit without normalization by the monotonic G_C values. The raw and normalized results for the thinned "T" samples of EMC thickness 0.774 mm are shown in Figure 44 and Figure 45.

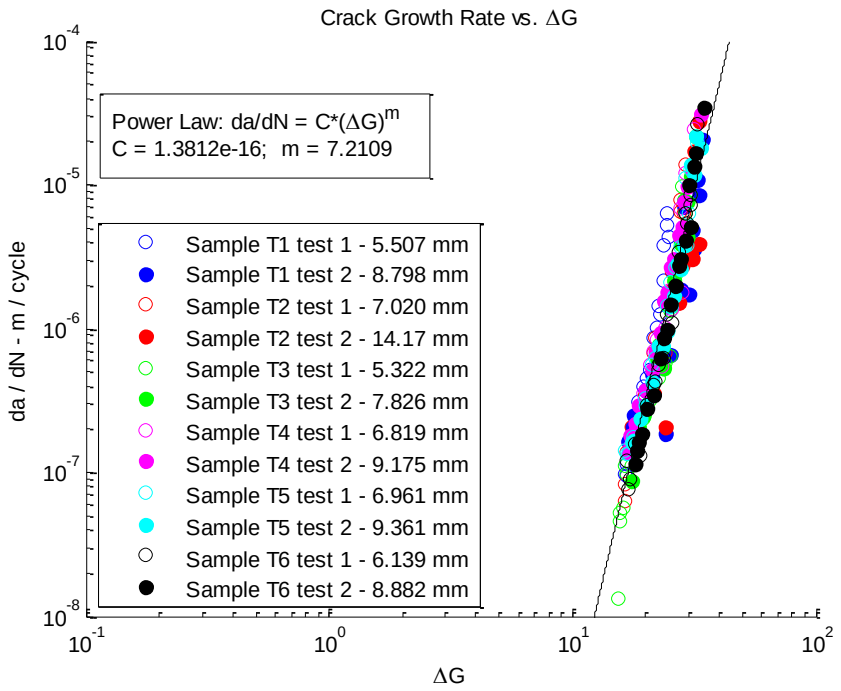

Figure 44 - Raw Paris' Law Data: "T" Samples

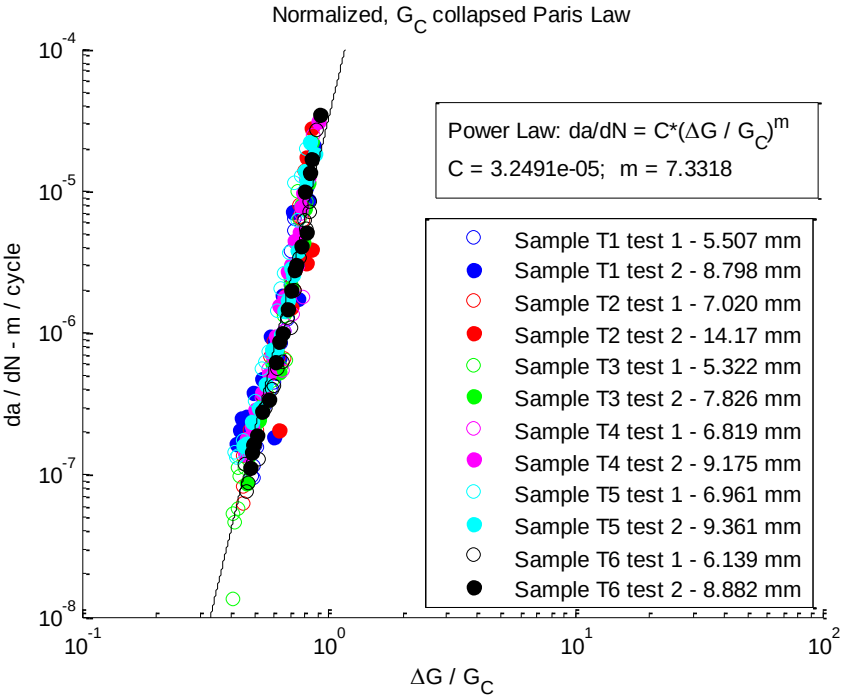

Figure 45 - Normalized Paris' Law Data: "T" Samples

It can be seen that both the raw and the normalized fitted curves are in good agreement for a relatively consistent Paris' law exponent: *m*. The differences in the m exponent are negligible, as would be expected when a constant value of G_c is used for normalization. The difference in the Paris' law coefficients corresponds to a translational shift in the log-log space resulting from the combined effects of the normalization factor (G_C) and the exponent *m*. It can also be observed that while the m exponent for the nominal samples of 1.524 mm EMC thickness have a Paris' law exponent of 10.144 the exponent in the case of the thinned "T" samples is lower at 7.332

The raw and normalzied results for the thinnest "V" samples are showin in Figure 46 and Figure 47.

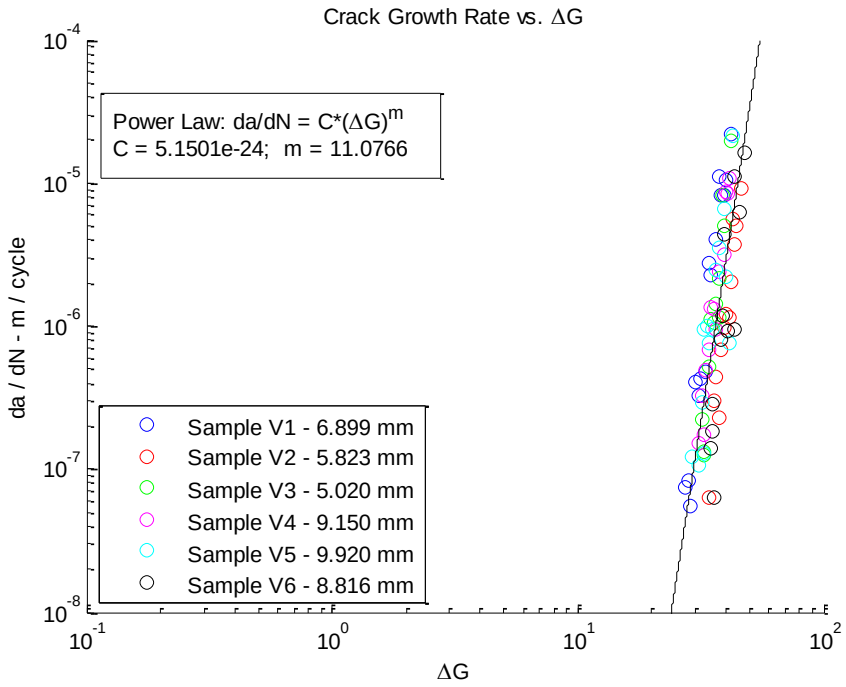

Figure 46 - Raw Paris' Law Data: "V" Samples

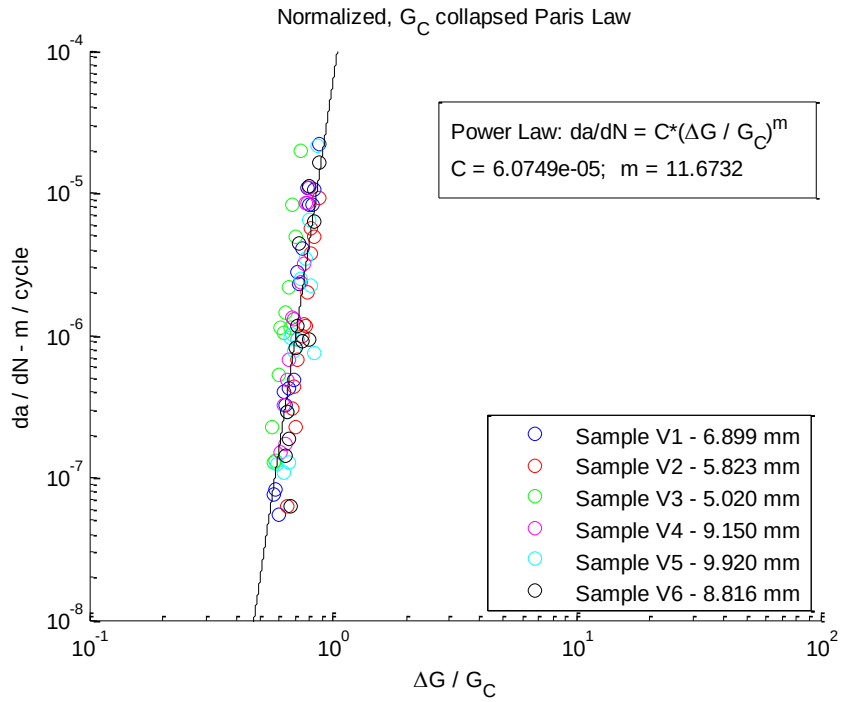

Figure 47 - Normalized Paris' Law Data: "V" Samples

The results for the thinnest "V" samples are similar to the "T" samples, and the difference in *m* between the mathematical fits for the raw and normalized results is negligible.

What is especially noteworthy is that the *m* exponent has increased in magnitude becoming similar to the m exponent for the R-curve corrected nominal sample thickness. The importance of this will be discussed in the following sections.

5.6.3 Influence on fatigue of mode-mixity

It is well established that the fracture of bimaterial interfaces is a function of mode-mixity. In case of the copper / EMC interface under study, results indicate that the SERR minimum as a function of mode-mixity occurs near the $\psi_G = 0$ condition as intuitively expected. G_C vs. ψ_G results for the average of the datasets (R-curve plateued values for the nominal sample set) are shown in Figure 48.

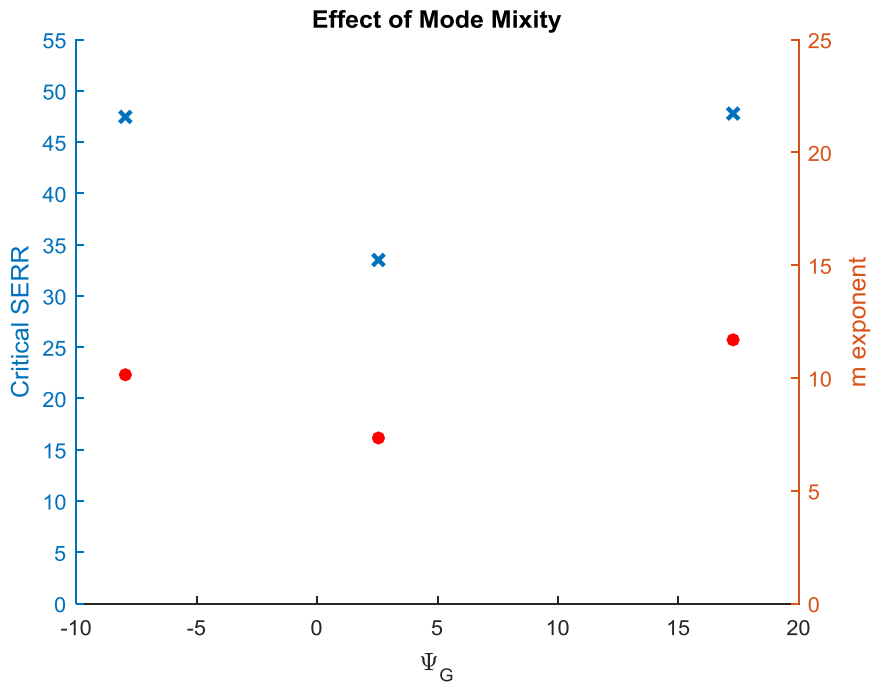

Figure 48 - Mode-Mixity Effects

Figure 48 also displays the results of the m exponent as ψ_G changes. In these experiments mode-mixity has been changed by varying the thickness of the EMC part of the bimaterial test samples. The changes in the sample assymetry rotates the crack tip stress field thus changing the mode-mixity. As can be seen the fatigue crack propagation exponent, m trends with the both the variation in monotonic critical SERR and the magnitude of the mode-mixity angle versus the pure tensile case.

5.6.4 Near-interface crack depth

Hutchinson and Suo [33] discussed at length the impact of mixed mode loading conditions, sample geometry, and material properties on the behavior of interfacial cracks, specifically whether they propagate parallel to or at the interface or progress in a direction not fully parallel. Figure 49, Figure 50, and Figure 51show SEM images taken

on a Hitachi SU8230 FE-SEM at the interface where fatigue crack propagation has occurred. Figure 52 shows the images of Figure 49-Figure 51 resized so that they are the same scale factor. It is clearly observable that that degree of residual EMC atop the copper surface varies for all three cases. The least amount of EMC is present on the "S" samples, an intermediate amount is present for the "T" samples and clearly the most residual EMC present atop the "V" samples. At this small scale the perspectives of continuum mechanics start to be less applicable as both the bond of the flown EMC and its cohesive behavior start to exhibit heterogeneity. It is still useful, however, to interpret the relative bareness or completeness of EMC coverage as linked with the "depth" of a near-interface crack until complete coverage is obtained. When considered in this fashion it can be observed that decreasing the mode-mixity by thinning the thickness of the EMC layer in the test sample results in a steady increase of the interfacial crack depth in the EMC. It is also worth noting how these features are only observable through the SEM imagine as the optical images shown in Figure 4 all appear to have bare exposed copper.

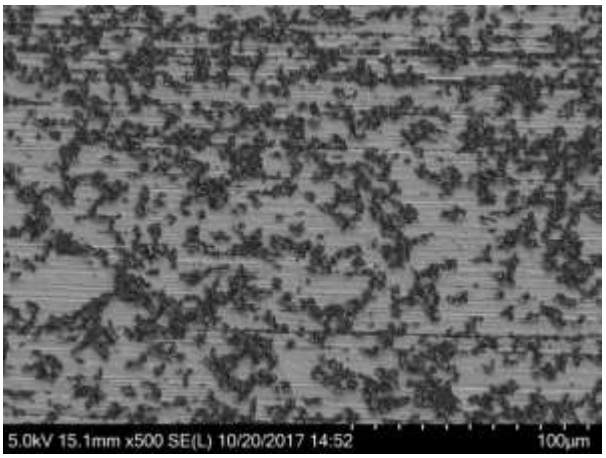

Figure 49 - SEM Image of Residual EMC on Copper Crack Surface: Nominal Sample

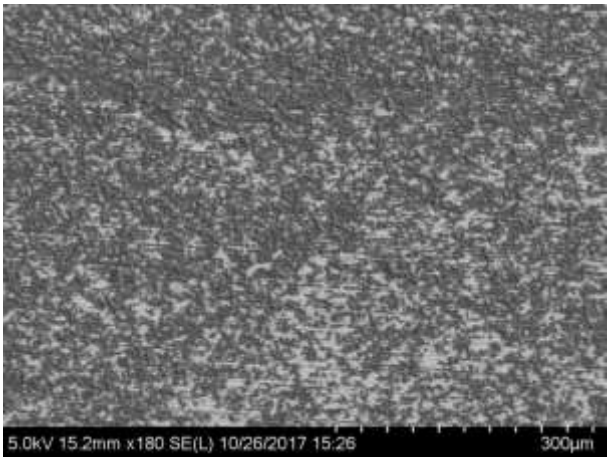

Figure 50 - SEM Image of Residual EMC on Copper Crack Surface: "T" Sample

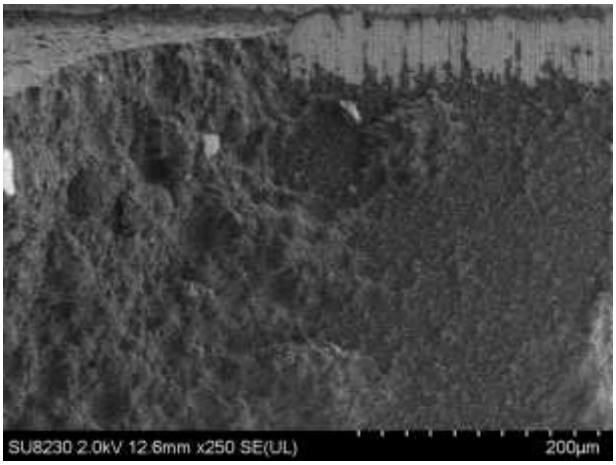

Figure 51 - SEM Image of Residual EMC on Copper Crack Surface: "V" Sample

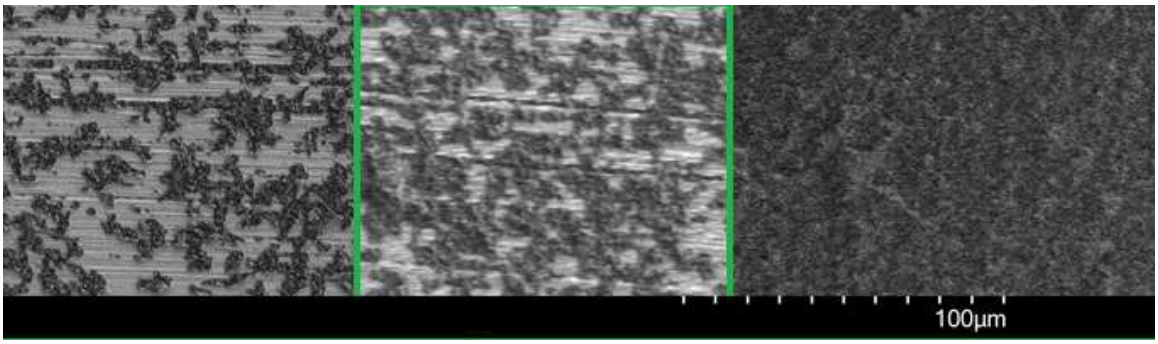

Figure 52 - SEM Comparison of Residual EMC

The observation of crack depth is especially noteworthy. By changing the EMC thickness both the depth of the near-interface crack and the mode-mixity have changed. It has been observed that the Paris' law exponent, *m*, trends with the change in mode-mixity as well. By noting that m increases in magnitude with mode-mixity in both directions while the interfacial crack depth monotonically increases as the stress fields are directed towards the EMC only, it can be seen that the fatigue exponent trends with mode-mixity but not interfacial depth. Simply put, changing the EMC thickness modifies both the mode-mixity and the interfacial depth, but the fatigue exponent is only correlated with the magnitude of the mode-mixity angle.

5.6.5 Mode-mixity as reflected by numerical model stress fields

The nominal 1.524 mm test samples experience loading with a mode-mixity of 17.3°. For the nominal samples the EMC is relatively rigid compared to the copper due to its much greater thickness resulting in the copper dominating the sample compliance. This also results in the orientation of the mixed mode stress field being directed preferentially towards the copper. Stresses for the nominal sample are shown in Figure 53. As shown in the figure, stresses σ_{yy} exbhibit the characteristic peanut shape around

the crack tip while τ_{xy} reflect the oscillatory nature of the stress fields. For the nominal samples just ahead of the crack tip the shear stresses are positive (to the left) in the EMC and negative (to the right) in the copper. This induces a counterclockwise shear loading which would result in a preference for the crack to be directed into the copper. With a ductile copper however resisting crack kinking, the crack propagates close to the interface.

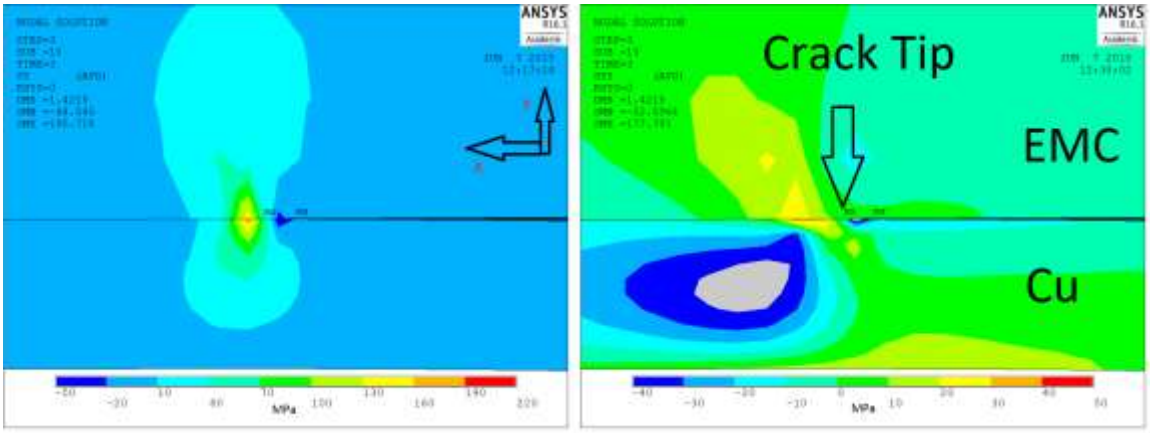

Figure 53 - σyy and τxy Crack Tip Stresses: Nominal Samples

In thinning the EMC to 0.774 mm for the "T" samples, the mode-mixity changes and equivalently the orientation of the stress fields. As can be seen in Figure 54, signs of the σ_{yy} and τ_{xy} are unchanged resulting in the same directional preference for the crack towards copper. For both the nominal "S" and the "T" samples this coincides with a positive mode-mixity angle. Additionally both the copper and EMC now contribute meaningfully to the overall compliance of the test sample.

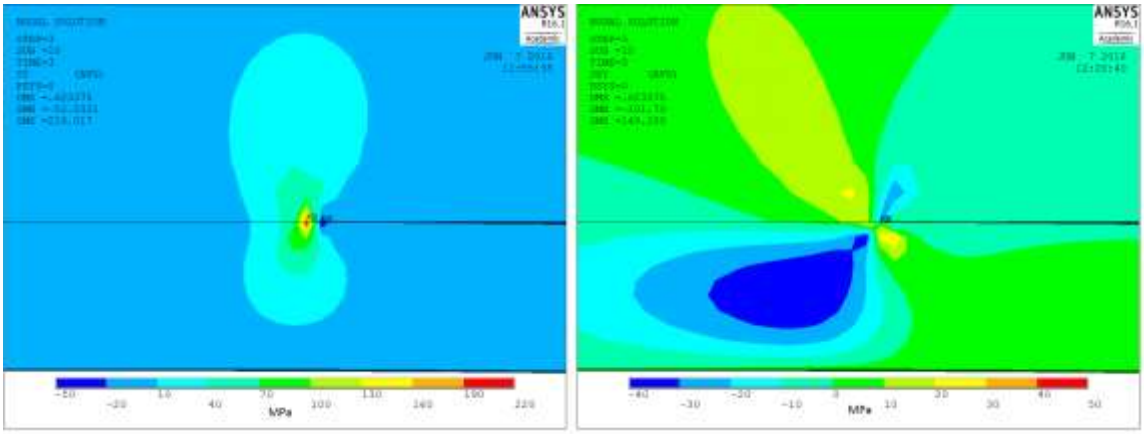

Figure 54 - σyy and τxy Component Crack Tip Stresses: "T" Samples

For the thinnest samples in set “V,” the stress field has been further rotated into the EMC as reflected by the negative mode-mixity values when calculated using a nodal displacement method. It can also be seen in Figure 55 that the sign of the shear stresses in the EMC and just ahead (left) of the crack tips have changed in sign. This coincides with a negative mode-mixity angle and the crack now has a preferential induction to crack into the EMC rather than the copper.

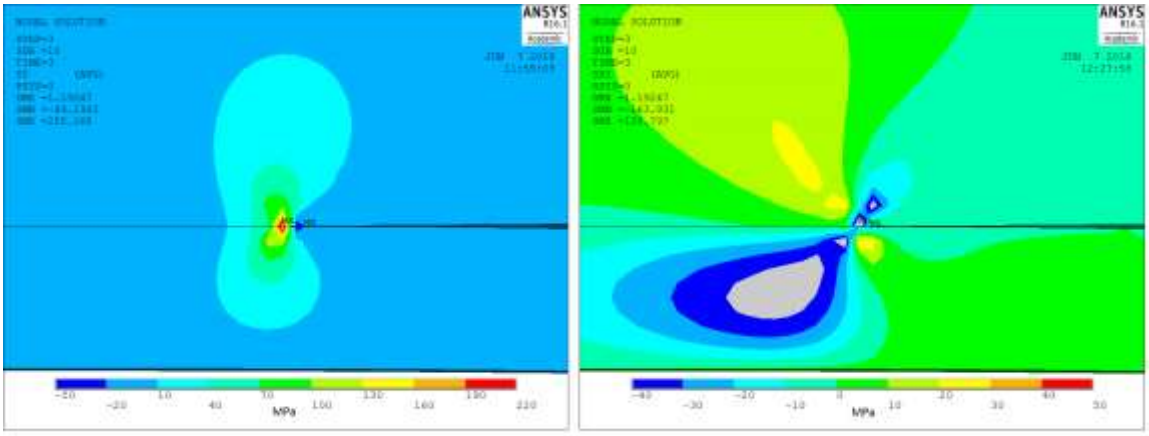

Figure 55 - σyy and τxy Component Crack Tip Stresses: "V" Samples

5.7 Practical Usage of Fatigue Data

If the mode-mixity for the interface being studied is known, choosing the presented Paris' law for the most similar mode-mixity condition and applying conservative design approaches would provide useful information even in the absence of on hand fatigue test results. For cases where the mode-mixity is unknown, it is useful to consider the entirety of the normalized crack propagation results. This information is presented in Figure 56.

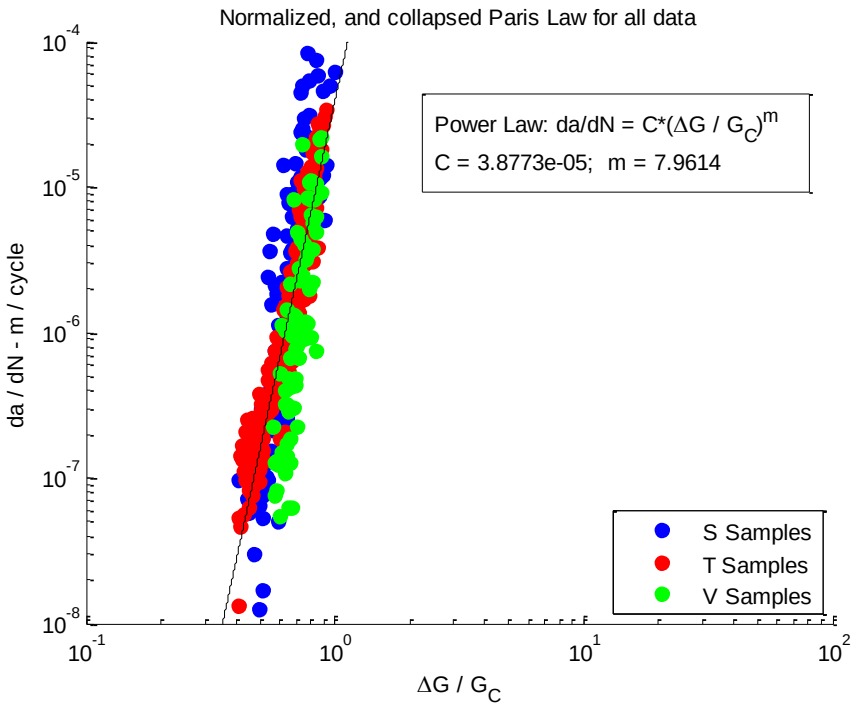

Figure 56 - Paris' Law Data: All Samples

The established results as shown in Figure 42-Figure 47 and summarized for the fatigue exponent, *m* in Figure 48 has been consolidated and a single fit established inFigure 56. The overall fit of the data is still good though, suboptimal as compared to the mode-mixity decomposed results. In particular it can be seen that the nominal test samples from set S, shown in blue are the farthest to the left and as such represent the

most conservative choice. As a result, the Paris' laws reported for both a best fit, and a conservative case for the S set samples, as described in detail in [38] and re-iterated below in Equations 37)37 and 38 can still be used as long as conservative design approaches are followed.

$$da/dN = C * \left(\Delta G/G_R\right)^m = 8.89 * 10^{-18} * \Delta G^{10.144} \quad (G_C = 20 \text{ J/m}^2 \quad \textbf{46)}$$

Conservative fit)

$$da/dN = C * \left(\Delta G/G_R\right)^m = 8.17 * 10^{-22} * \Delta G^{10.144} \quad (G_C = 50 \text{ J/m}^2) \quad \textbf{47)}$$

5.8 Conclusions

By varying the geometric asymmetry of a bimaterial DCB test specimen the local mode-mixity at the crack tip was able to be varied. Subsequent cyclic fatigue testing demonstrated that the resulting normalized Paris' laws are functions of the change in mode-mixity. Specifically the magnitude of the Paris' law exponent, *m*, varies along with the magnitude of the mode-mixity angle from the pure tensile case.

Subsequent SEM surface characterization of the liberated copper interface showed that the failure of the bimaterial interface under study varied from being very close to a true interfacial crack to a near-interface crack depending on the local mode-mixity of the test. These trends were further confirmed through the variation of the stress fields in the EMC as seen through numerical analysis.

This work demonstrates an explicit correlation between the mixed mode monotonic fracture behavior of a bimaterial interface and the fatigue characteristics of the interface. While subtly implied by Zhang and Shang [67], their work tended to focus more on the threshold of crack initiation rather than propagation dependencies. This work additionally compares the fatigue crack growth behavior for both positive and negative mode-mixities. The implications of this correlation are significant in that it may be possible to infer the variation of fatigue behavior for other mode-mixities from one set of fatigue behavior at a single mode-mixity and a collection of monotonic tests at various mode-mixities.

Future studies warrant two points of focus. First these observations should be confirmed through a greater experimental test base. The second focus should be on additional micromechanical characterization to determine the linking physics between the fatigue behavior and mode-mixity. Such understanding will also greatly impact the knowledge pertaining to the shape of the monotonic failure locus itself which also has important modeling ramifications.

CHAPTER 6. COHESIVE-ZONE PARAMETERS FOR A CYCLICALLY LOADED COPPER EPOXY MOLDING COMPOUND INTERFACE

Abstract — Bimaterial interfaces, like the one consisting of epoxy mold compound (EMC) cured over copper leadframe, are commonly present in microelectronic packages. Failure in such bimaterial interfaces can be simulated through the use of cohesive-zone modeling (CZM). To date, nearly all CZM modeling of bimaterial interfaces has been performed for monotonic loading conditions. However, most of the interfacial failures in microelectronic packages occur during operating conditions where repetitive or fatigue loading conditions are present. The CZM work for fatigue seen in literature utilizes methods which while demonstrably accurate, are data correlation schemes rather than derivations formulated from the underlying micromechanical behavior. Most proposed fatigue CZM models incorporate fatigue damage by decreasing the critical strain energy release rate (SERR), G_c, though a modified CZM damage parameter.

This work presents a new characterization approach which continuously modifies CZM parameters as fatigue loading occurs. This new characterization method offers the potential of higher predictive value as it requires no assumptions beyond that of energy conservation; an assumption already inherent to the formulation of cohesive-zone modeling. Through the addition of fatigue effects to CZM behavior, this method is capable of predicting and modeling crack propagation for loads below the monotonic critical level.

6.1 Contextualization Notes Regarding Fit into the Overall Work

The preceding chapters have discussed the study of mixed mode fracture for both monotonic and fatigue conditions for a variety of test geometries. These chapters also outlined the development of an experimental and analytical methodology for testing interfacial fatigue crack propagation as a function of mode-mixity. Once characterized a means of incorporating fatigue behavior into numerical simulations, such as ANSYS is required to obtain FEA models with utility towards interfacial fatigue at low computational cost.

The content of this chapter is from the work presented and published at the 2016 IEEE Electronic Components and Technology Conference in Las Vegas, NV. [71] This work describes and demonstrates in 2D a conceptual approach to build fatigue crack propagation into the existing cohesive-zone modeling (CZM) framework. For the 2D models demonstrated, this was done by writing additional APDL code which, in addition to running the ANSYS simulations, both extracted data from and populated model data with, information derived from the discussed approach. As such, the code acted as a wrapper to implement the approach. While feasible in 2D, this approach would become computationally unreasonable for 3D models. Implementation of this method in 3D will require the creation of a new user-defined FEA element type which will perform the required operations. This task was determined to be out of the scope of this work.

6.2 Background

Interfacial crack propagation for metal-polymer interfaces has been studied through fracture mechanics approaches over the years [e.g [23-26, 31, 45, 72-76]]. Cohesive-

zone modeling (CZM) is increasingly sought to study interfacial delamination due to the simplicity in implementation for crack initiation and propagation. Although CZM has been effective for studying delamination under monotonic loading, the development of CZM for fatigue interfacial delamination propagation has a long way to mature.

Most proposed fatigue cohesive-zone models incorporate fatigue damage by decreasing the critical strain energy release rate (SERR), Gc, through a modified CZM damage parameter [19, 61]. The modified damage parameter is typically made a function of a prescribed modified Paris Law correlation. This method results in simulations which return the expected fatigue crack growth behavior, but offer somewhat limited predictive capability as they are only applicable within the range of data used to define the incorporated correlations. The methods are data correlation schemes which utilize a variable, the damage parameter that is a modeling implementation formulation and has no direct equivalence to the underlying physics [21, 22].

The new characterization approach modifies the CZM parameters as fatigue loading occurs for the elements localized around the crack tip via energy methods.

6.3 Cohesive-Zone Modeling

Cohesive-zone modeling is an FEA method for simulating crack initiation and growth that does not require re-meshing. The inspiration for CZM was developed by Dugdale [10] and Barenblatt [11] in the early 60's but it has experienced renewed interest with improvements in computing power. Cohesive-zone modeling utilizes interfacial

elements that are governed by a traction-separation relationship. Multiple forms of traction-separation relationships exist, such as exponential, bi-linear and trapezoidal. The work contained herein incorporates the use of bi-linear CZM elements in ANSYS based upon the work by Alfano and Crisfield [14]. Through the use of a damage parameter, cohesive-zone elements can be damaged, effectively broken, and in the process create new surfaces. The area under the traction-separation law is equal to the critical SERR.

6.3.1 Monotonic Critical SERR Characterization for a Cu/EMC bi-material interface

For a two-dimension mixed-mode bi-linear CZM formulation, 6 parameters total (3 for each mode) are needed to define the necessary traction-separation laws. Previous work performed by Krieger et al. [37], Raghavan et al. [77, 78] and Kwatra et al. [32] utilized tests at different mode-mixities, DCB and 4PB, to calculate the necessary parameters. Results for each test include the critical SERR at the associated mode-mixity, the maximum load achieved, and the slope of the load/displacement data. The combination of these results provides the necessary information to define the mixed-mode traction-separation laws.

Utilizing the methods from Krieger the critical SERR for DCB and 4PB tests were measured to be 35.6 J/m^2 and 44.6 J/m^2 respectively. The mode-mixities of the DCB and 4PB tests were calculated to be 25.7° and 34.6°. This information is presented in Table 13. A G_c to mode-mixity relationship can then be fit based upon the Hutchinson and Suo model [33] per Equation 48.

Table 13 - Critical Strain Energy Release Rate Results for DCB and 4 PB Testing

Test	Critical Strain Energy Release Rates used for monotonic CZM parameters	
	G_c	ψ
DCB	35.6 Jm^2	25.7°
4PB	44.6 J/m^2	34.6°

$$G_C = G_{I,C}\left[1 + \tan^2\left(\psi(1 - \lambda_{HS})\right)\right] \quad 48)$$

These results were used to generate traction-separation laws for both Mode I and Mode II, as shown in Figure 57.

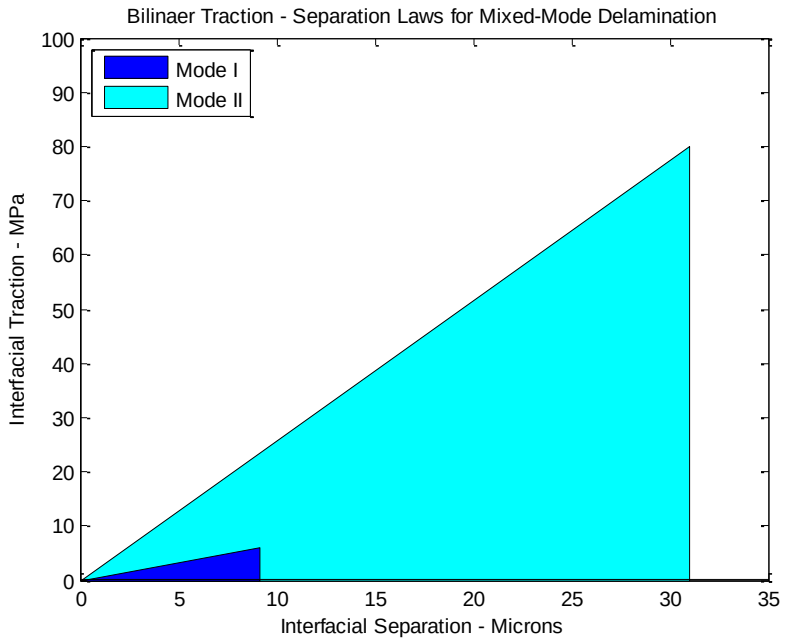

Figure 57 - Mixed Mode Bilinear Traction-Separation Laws

($\alpha = \delta^*/\ \delta_c = 0.99999$ were used for convenience) δ^* is the displacement at maximum traction while δ_c is the displacement when de-cohesion has completed and the element is fully damaged. The steep shape of the traction-separation law used benefited the energy decrement method to be described later in this work.

6.3.2 Effect of CZM Traction-Separation Law Shape

Theoretically, the effect of CZM traction-separation law shape should not influence the resulting global load/displacement data as long as the area under the traction-separation laws is equal to the appropriate modal critical SERR. In practice however, FEA spatial discretization of the crack tip stress singularity means that meshing has influence on the achievable global peak loads. This can be seen in Figure 58. Alfano discussed at length the practical impacts on how choosing CZM parameters will affect the results and performance of the model. [14] Ideally a refined mesh and sufficiently large maximum

traction would be possible and allow the effective re-creation of the crack tip singularity in agreement with LEFM perspectives and formulations. This approach however results in untenably high computation times and is not feasible. In practice, one of the benefits

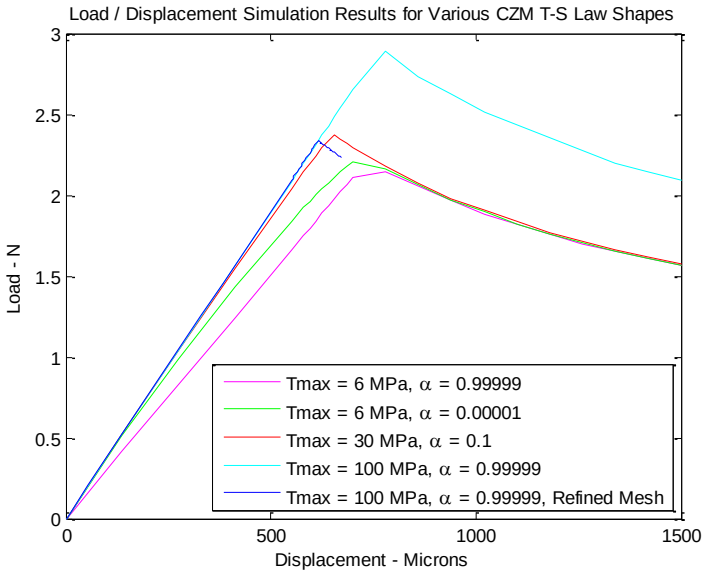

Figure 58 - Effect of Cohesive-Zone Traction-Separation Law Shape on Load / Displacement results

of FEA CZM implementations is that it is an energy-conservative method, given that energy measurements are only taken at the moment of the crack tip elements full de-cohesion. Instantaneous measurement of partial element energy via the damage parameter is not accurate as the damage parameter is formulated to transition from undamaged (D=0) to fully damaged (D=1) but is not necessarily accurate at every point through that transition due to its extreme nonlinearity and disconnect from the governing physics.

The traditional usage of CZM in FEA applications allows the accurate modeling of crack initiation and propagation via the energy conservative nature of the method, but in a fashion to alleviate the stress concentration around the crack tip and thus reduce

computation time. As a result, great care must be taken when making claims about the stress states in a CZM contact zone, and special care must be taken when addressing what the "true" crack length is for a CZM formulation. For example, for the purposes of estimating an applied G loading value, approximating the crack length as the distance to the first unbroken element, and thus the length of the cantilever beam is acceptable. But, for the purposes of making LEFM equivalent measurements of crack growth, a better calculation, and the one employed here, is to calculate the equivalent crack length via the calculated compliance from load/displacement data. It is though this "equivalent length" that an equivalent energy be calculated and facilitate comparisons between LEFM models and CZM.

Given the facts noted in the previous paragraph, the impact on CZM traction-separation law shape is dependent on mesh density. This dependency is due to the resulting discretization errors induced in loading and effective crack lengths. As long as mesh convergence is kept in mind, the CZM traction-separation law can be chosen based on convergence needs or other convenience factors.

6.4 Experimental Characterization of the Paris Law

Previous work, as described in Samet et. al. [79], demonstrated the derivation of a crack propagation Paris Law relationship through the combination of load/displacement

data from cyclic DCB tests with analytical formulations. The DCB test setup is shown in Figure 59 along with an illustrative schematic.

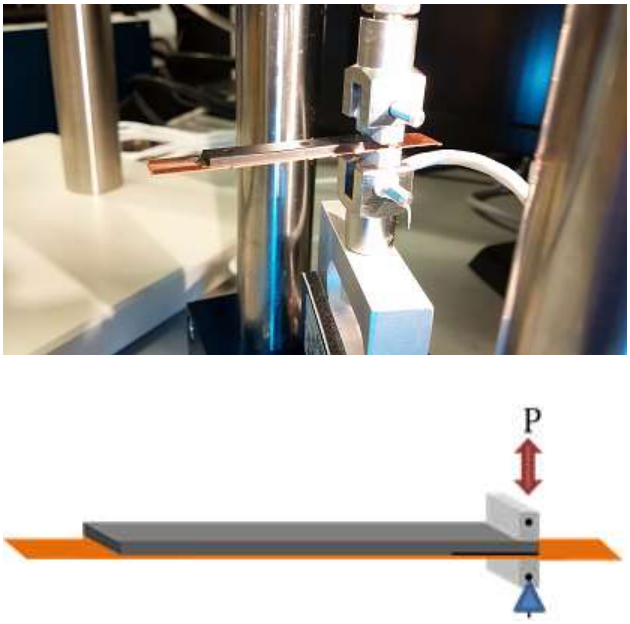

Figure 59 - DCB Experimental Test Setup and Schematic

That method was refined through the use of longer duration displacement control tests. After calculating the crack length from measured compliance and the G values from Soboyejo [4], the total G_c value was calculated from the $G_{I,C}$ and the mode-mixity.

$$da/dN = 2.2873 * 10^{-16} \Delta G^{6.7765} \quad 49)$$

This data was then used to determine the Paris Law crack propagation relationship as described in Equation 49 and shown in Figure 60.

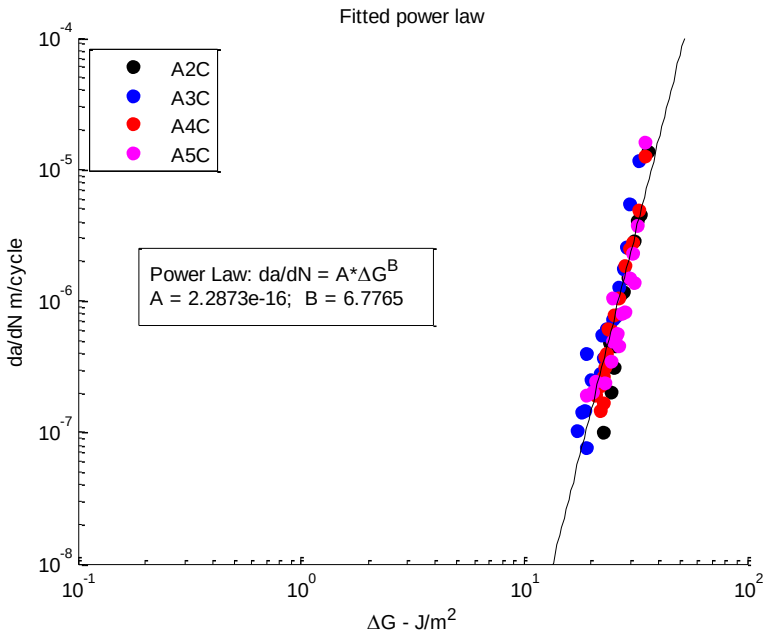

Figure 60 - Fitted Paris Law

This Paris law was calculated by dividing the test data into groups of cycles with minimal variation in the ΔG loading, but with enough cycles to see the resulting crack propagation rate. The data from these segmented linear approximations was then combined for multiple samples and used to fit the Paris law.

6.5 Energy Loss Characterization

Given that the standard CZM formulation is unable to accurately model fatigue, a method is needed to incorporate fatigue mechanics into the model to model fatigue crack propagation. Previous efforts to this end by de Moura and Goncalves [19, 61] and Roe and Siegmund [21] utilize a modified damage parameter based on a known Paris Law relationship, or some other damage mechanism such as void nucleation [22].

The method described in this work, uses the load / displacement data from experimental tests to calculate the energy lost to fatigue for a given cycle. The energy lost to each cycle for displacement-controlled tests can be calculated as the area between the load/displacement curves for sequential load cycles. This is described by Figure 61 and Equation 5050).

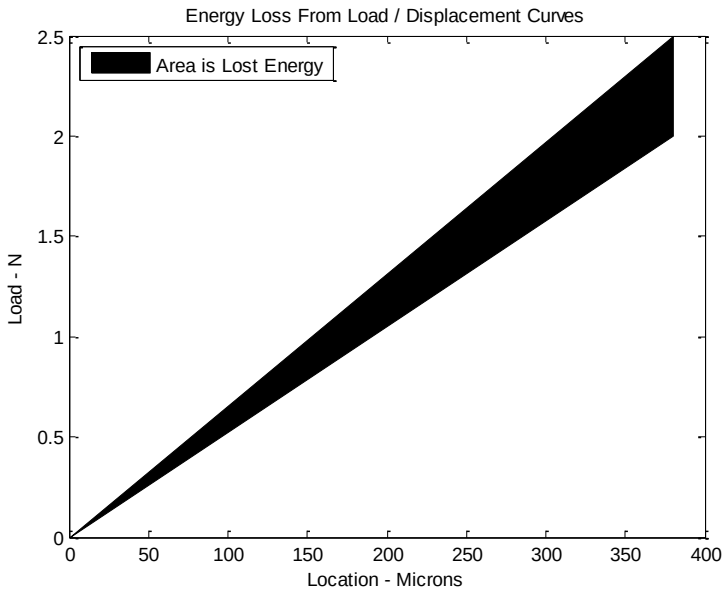

Figure 61 - Lost Energy as Determined from Load / Displacement Data

$$E_{Lost} = \frac{1}{2}(P_i - P_{i+1}) * displacement \quad 50)$$

This lost energy is equal to the amount of energy that must be extracted from the FEA model in order to propagate the crack for that cycle.

It is important to note that in order to apply this method, perfectly smooth data is required. Experimental load / displacement data cannot be used as the noise in the data would result in frequent calculations of negative energy loss. To overcome this issue, the Paris law previously derived, is applied in conjunction with a mathematical model of the test sample per classic Euler beam theory to produce a theoretical ideal crack length and load versus cycle history. The load history results of this and a comparison between the experimental data and the simulated crack length can be seen in Figure 62.

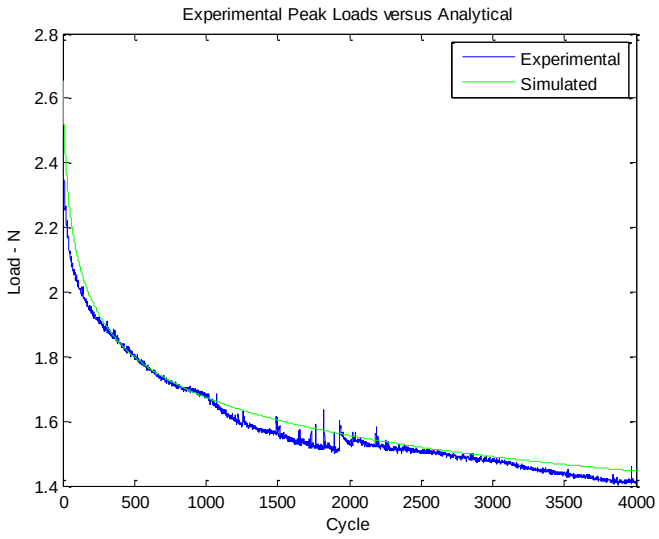

Figure 62 - Energy Lost from Fatigue vs. Applied Load

The maximum load data is then forward differenced and used to calculate the energy loss history per Equation 50.

6.5.1 Energy Loss vs. G Applied

With the energy loss as a function of cycles achieved, the applied SERR loading can then be used to obtain an energy loss to $G_{applied}$ relationship as both parameters are reported with respect to the loading cycle. This relationship is shown in Figure 63. A 4^{th} order polynomial provides an accurate fit to the data and is used in the ANSYS model to calculate the required extracted energy during a loading cycle. This polynomial is reported as Equation 51. This correlation provides some of the necessary information in order to calculate the appropriate cyclic energy loss for the modified FEA CZM.

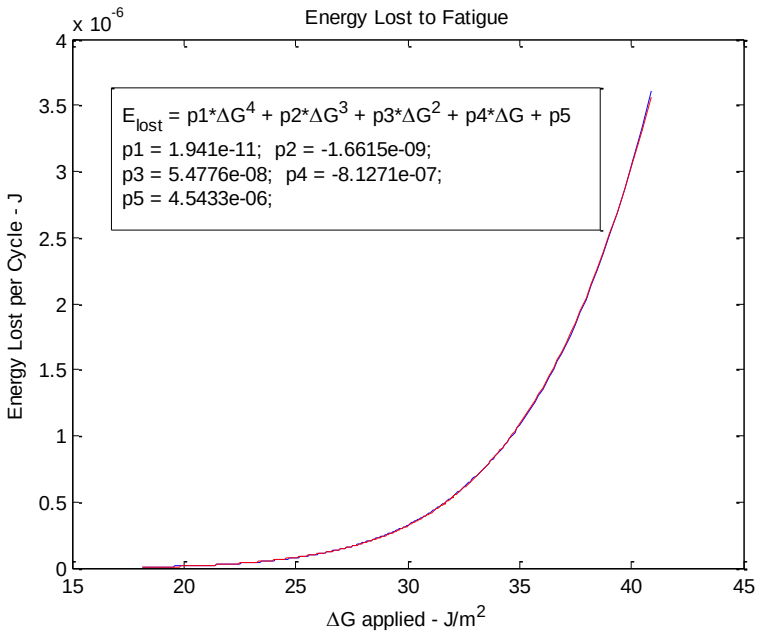

Figure 63 - Energy Lost from Fatigue vs. Energy Lost per Cycle

$$E_{Lost} = 1.941 * 10^{-11}\Delta G^4 - 1.6615 * 10^{-9}\Delta G^3 + 5.4776 * 10^{-8}\Delta G^2 - 8.127 * 10^{-7}\Delta G + 4.5433 * 10^{-6} \quad (51)$$

6.6 Energy Decrement Method

Cohesive-zone modeling has predictive value as it is an energy conservative method even though it may have localized inaccuracies due to the alleviation of the stress singularity predicted by LEFM. To model fatigue consistent with this underlying structure an energy decrement method has been developed.

With a known critical SERR, the energy density for a cohesive-zone element is known. With a known mesh size, the amount of energy required to completely de-bond a cohesive-zone element and propagate the crack by an amount equal to the element length can be calculated as shown in Equation 52. Element width and length are "w" and "l" respectively.

$$E_{CZM,element} = G_C * w_{element} * l_{element} \quad 52)$$

In the energy decrement method, a collection of "weakened" elements are used to modify cohesive-zone traction-separation laws. These elements are shown in Figure 64. For these elements, the maximum traction is reduced while all other parameters are kept constant. The area between the old CZM traction-separation law and the new traction-separation law for an element is equation to the energy extracted. When run for subsequent cycles, additional loading can finish de-cohesion of the element. Energy is removed from enough elements such that the sum of the removed energy from all elements modified during a load cycle, is equal to the required removed energy as calculated based on the load level. This is described in Equation 53. The starting degree of weakening (if any) for all elements is

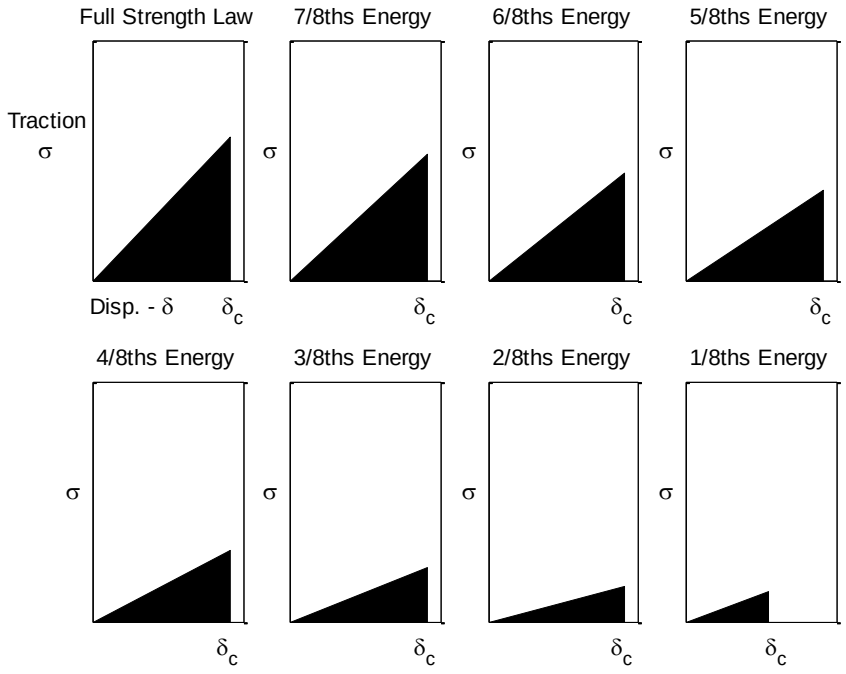

Figure 64 - Weakened Mode I Traction Separation Laws Used to Extract Energy Lost to Fatigue

$$E_{Lost,cycle} = \sum E_{before\ cycle} - E_{after\ cycle} \quad 53)$$

needed as the amount of energy which can be removed from a given element is based upon its starting strength. Previously weakened elements cannot be weakened as much as full strength elements. It is also of special note that the critical displacement for the weakest utilized element is intentionally made shorter than that of all other CZM traction-separation laws. This is to ensure that any subsequent loading results in complete de-bonding, which removes the remaining of the energy and propagates the crack. This method is necessitated by the fact that cohesive-zone elements cannot be forced to break

arbitrarily. This implementation achieves the same effective end while accommodating the code limitations currently present in ANSYS. The development of a customized element may be preferable as it may alleviate the previously described limitations, and/or improve computational efficiency and will be the subject of future investigations.

6.6.1 Results and Error of the Energy Decrement Method

Figure 65 shows a comparison of the results between a traditional CZM implementation and the method described in the previous section. The results illustrated are for identical loading conditions, loading cycle number and are presented with identical viewports and zoom factors. It can be clearly seen that the energy decrement method, described in the previous section, results in additional delamination and is capable of modeling fatigue crack propagation. To analyze the degree of error of the method a starter crack of approximately 9.7 mm was used. Figure 66 shows a comparison of the expected

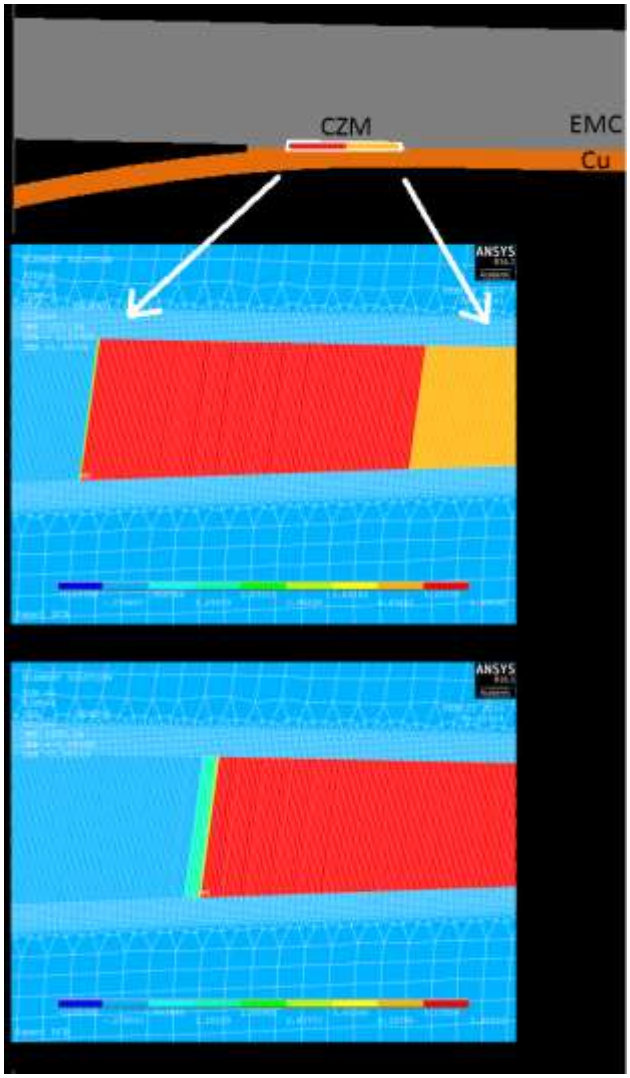

Figure 65 - FEA Comparison of Traditional CZM vs. The Energy Decrement Method

crack length calculated analytically via beam theory and the derived Paris law relationship to the crack lengths resulting from the FEA CZM simulation utilizing the energy decrement method.

It can be clearly seen that the energy decrement method is successful in introducing fatigue crack propagation. Figure 67 shows the calculated difference in the crack propagation rate for each cycle between the analytical and the FEA results. For this

example case, the maximum crack growth rate error for any individual cycle is approximately equal to 0.6 microns which was the simulation mesh density. While the error from any individual cycle is small, the effect is cumulative resulting in larger errors with increasing cycles. This error needs to be accounted for and will be the subject of future work. This error is believed to be the result of discretization as any inaccuracy of the predicted delamination due to fatigue will affect the load level of subsequent cycles. Subsequent cycles load levels impact the expected required energy decrement and thusly the crack propagation rate. As a result, this linked effect will continue to future cycles. Accommodating this integral error will be necessary in order to further the usefulness of the energy decrement method. However, despite the error's presence, it does not negate the fundamental effectiveness of the developed method.

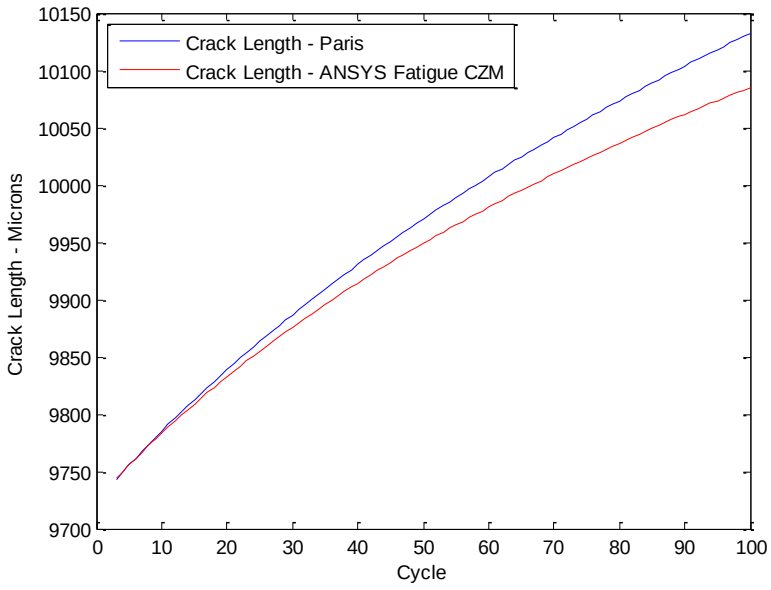

Figure 66 - Crack Length Comparison: Energy Decrement Method vs. Analytical Expected Results

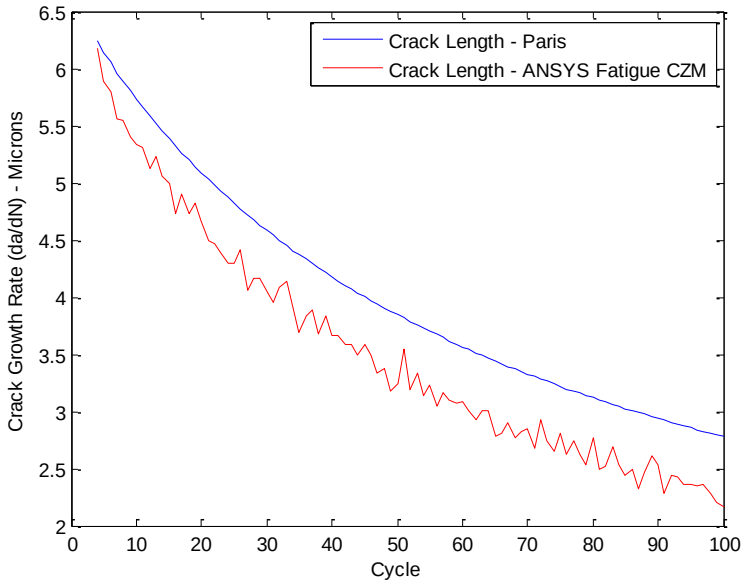

Figure 67 - Crack Length Growth Rate Comparison: Energy Decrement Method vs. Analytical Expected Results

6.7 Conclusion

A new method to model fatigue for CZM FEA implementations has been developed based upon energy conservation methods and experimental data. While the method is strictly speaking a data-correlation implementation to experimental results, the degree of mathematical abstraction has been reduced by employing energy methods as compared to other approaches. Additionally, compatibility with the related underlying derivations of CZM has been maximized. The named "Energy-Decrement Method" demonstrates the ability to model and predict fatigue crack propagation for subcritical load levels. The accuracy of the model can be improved moving forward, specifically by addressing the integral error incurred when observing expected crack length. It is worth noting that such an integral error is not unexpected as integral errors are typical when

modeling fatigue crack behavior due to the interplay between the accuracy of the incremental crack growth rate and the subsequent expected load level. A major point of development moving forward will be the implementation of this method accurately for larger numbers of cycles. To this end, methods similar to the "cycle jump" as described by de Moura [19] will be considered. While in certain conditions computationally expensive, the energy decrement method can be modified for the problem at hand. For example, it took approximately 6 hours on a traditional desktop workstation to run a displacement controlled fatigue simulation of 100 cycles. The simulation duration may be permissible for investigations of low-cycle-fatigue (LCF) on the order of 10^3 cycles, but it is too long for high-cycle-fatigue (HCF). With revisions and improvements to the implementation, the authors believe a path forward may exist to use this method for even HCF simulations.

6.8 Final Notes

Much of the information used to populate the Energy Decrement Method as described in this chapter was subsequently revised with additional data gathering. This is true for both critical SERR and mode-mixitiy. Figure 23 in Chapter 3 shows the revised data which should be used as the source data for the Energy Decrement Method. Additionally the mathematical form used to fit the critical SERR vs. ψ curve was that of Hutchinson and Suo rather than one of the forms which would be advocated for given the considerations described in Chapter 3. Figure 23 has been re-printed below in Figure 68 to highlight that the difference in the resulting failure loci between the Hutchinson and Suo model used here in Chapter 6 and the more appropriate elliptical criterion as discussed in Chapter 3 is negligible for our current dataset.

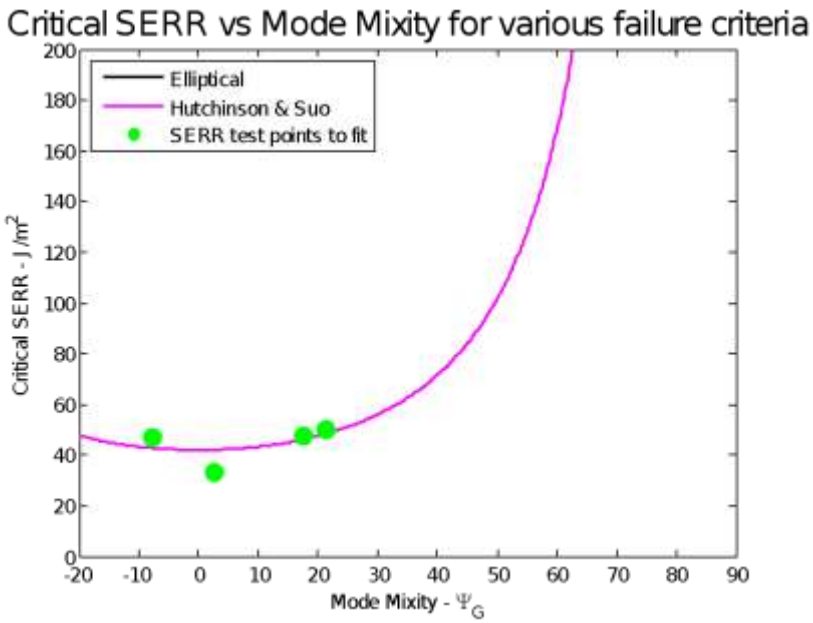

Figure 68 - Mathematical Forms of Mode-Mixity

Despite the need for following work to follow a CZM consistent failure locus as advocated in Chapter 3 the method as presented in Chapter 6 will still work for the refined datasets and remains a viable and potentially computationally affordable implementation approach for modelling fatigue crack propagation where the crack path is known to exist at a bimaterial interface.

In contrast with the element sizing used for the 2D models explored in this Chapter, extension of this method into 3D will require three primary considerations:

- The creation of a new 3D element type which directly incorporates the Energy Decrement Method. This is needed as the "wrapper" method pursued in 2D becomes computationally too expensive in 3D. Only a user defined custom element will be able to implement the method without substantially increasing computation time.

- The verification of the fatigue mode-mixity dependency as explored in Chapters 3 and 5 and incorporation into the 3D Energy Decrement Method user defined elements.

- Unlike in the 2D demonstration model, the 3D model should contain element sizes substantially large enough to minimize the number of elements required, possibly all the way to a single element, to extract the energy lost to fatigue. Additionally the distribution of the energy across the 3D crack front should be considered and as of this time, expected to be distributed consistent with energy minimization considerations.

CHAPTER 7. CONCLUSIONS, CONTRIBUTIONS AND FUTURE WORK

7.1 Conclusions

- The critical strain energy release rate of a copper / EMC bimaterial interface has been demonstrated to be a function of mode-mixity through DCB and 4PB tests.
- The DMMB test is inapplicable for our specimens due to invalidating degrees of plasticity
- An upper limit of testable mode-mixity may exist resulting from sample bulk fracture occurring prior to delamination for certain test geometries.
- Numerical and analytical formulations can be determined accurate to approximately 10%.
- The popular Hutchinson and Suo failure locus is inconsistent with FEA CZM formulations, though this incompatibility has yet to result in significant erroneous results as the differences are minor at low mode-mixites
- Fatigue crack length can be monitored through compliance-based approaches for delamination at the millimeter to microscale.
- Paris fatigue crack propagation relationships can be determined through compliance-based approaches.
- The Paris' law exponent of the normalized Paris' law has been observed to be a function of mode-mixity similarly to the way critical SERR is a function of mode-mixity.

- Changing the DCB sample thicknesses changes both the mode-mixity and the depth of the crack of the bimaterial interface. Only the Paris' law exponent trends with mode-mixity however eliminating crack interface depth as a potential causal factor of exponent variation.
- A new fatigue-compatible CZM modeling method, The Energy Decrement Method, has been developed and validated for fatigue crack propagation. This new method offers potential increased FEA utility at affordable computational cost.

7.2 Contributions

This work has contributed to the intellectual body of knowledge in the following ways:

- This work is one of the first works to systematically study the failure locus in GI and GII space and the transformation of such a locus in Gc vs. ψ_G space that is commonly employed in interfacial fracture studies. The obtained failure locus and the associated transformed curve are self-consistent with the cohesive-zone models employed to study interfacial delamination.
- By employing a wide range loading of loading conditions, this work has contributed to the modeling of interfacial crack propagation under fatigue loading as well as a method to determine increment in crack per cycle through compliance-based analysis. Such determinations of crack length

which increment in the range of 0.1 μm per cycle for mesoscale structures is another important contribution of this work.

- By performing interfacial crack propagation experiments under different load amplitudes and with different sample thicknesses and subsequently under different mode-mixities, this work has contributed toward the development of a unified interfacial crack propagation model.
- This work has developed an energy decrement approach to modify traction-separation cohesive-zone triangles under fatigue loading, and has employed such cohesive-zone models to study interfacial crack propagation. The developed approach is first of its kind.

7.3 Future Work

1) Actual delamination is 3D in nature; the loadings are combination of mode I, II, and III. There is a need for failure envelope for such mixed-mode loadings.
2) There is a need to develop test methods that can be employed at higher mode-mixities without resulting in the cohesive cracking of EMC. Also, there is a need to develop test methods for mode I and mode III combinations (currently the focus of Trilochan Rambhatla's Ph.D. work).
3) There is a need for more exhaustive study of the developed energy-decrement method and the associated changes in CZM triangles. Also, there is a need to validate such approaches against other experimental data.
4) Changes in CZM triangles should be explored in the context of in-situ measurements at different temperatures and humidity conditions, and such

studies need to be performed both under monotonic and fatigue loading conditions. (Existing work was not in-situ nor for fatigue.)

5) The current study has focused on obtaining various parameters and models using samples with simple geometries and configurations. For the models to be useful, they need to be tested against actual packages that are subjected to a combination of thermo-mechanical as well as mechanical loading conditions.
6) Future work should primarily be focused on the further verification of the mode-mixity trends observed and creation of a 3D Energy Decrement Method CZM model which is more of a computer science task rather than material science / mechanical engineering one and will likely require a dedicated researcher if not outside expertise.
7) Finally the potential to collapse all of the fatigue curves and the creation of a universal Paris' law through the making the C and m parameters functions of mode-mixity should be of significant focus.

REFERENCES

[1] P. Davidson and A. M. Waas, "Non-smooth mode I fracture of fibre-reinforced composites: an experimental, numerical and analytical study," *Philosophical Transactions of the Royal Society A: Mathematical, Physical and Engineering Sciences,* vol. 370, p. 1942, 2012.

[2] Z. Suo, G. Bao, and B. Fan, "Delamination R-curve phenomena due to damage," *Journal of the Mechanics and Physics of Solids,* vol. 40, pp. 1-16, 1992/01/01 1992.

[3] J. De Gracia, A. Boyano, A. Arrese, and F. Mujika, "A new approach for determining the R-curve in DCB tests without optical measurements," *Engineering Fracture Mechanics,* vol. 135, pp. 274-285, 2 2015.

[4] W. O. Soboyejo, G. Y. Lu, S. Chengalva, J. Zhang, and V. Kenner, "A modified mixed-mode bending specimen for the interfacial fracture testing of dissimilar materials," *Fatigue & Fracture of Engineering Materials & Structures,* vol. 22, pp. 799-810, Sep 1999.

[5] D. M. Parks, "The virtual crack extension method for nonlinear material behavior," *Computer Methods in Applied Mechanics and Engineering,* vol. 12, pp. 353-364, 12// 1977.

[6] E. F. Rybicki and M. F. Kanninen, "A finite element calculation of stress intensity factors by a modified crack closure integral," *Engineering Fracture Mechanics,* vol. 9, pp. 931-938, 1977/01/01 1977.

[7] I. S. Raju and K. N. Shivakumar, "An equivalent domain integral method in the two-dimensional analysis of mixed mode crack problems," *Engineering Fracture Mechanics,* vol. 37, pp. 707-725, 1990/01/01 1990.

[8] K. N. Shivakumar and I. S. Raju, "An equivalent domain integral method for three-dimensional mixed-mode fracture problems," *Engineering Fracture Mechanics,* vol. 42, pp. 935-959, 8// 1992.

[9] C. F. Shih, B. Moran, and T. Nakamura, "Energy release rate along a three-dimensional crack front in a thermally stressed body," *International Journal of Fracture,* vol. 30, pp. 79-102, 1986// 1986.

[10] D. S. Dugdale, "Yielding of steel sheets containing slits," *Journal of the Mechanics and Physics of Solids,* vol. 8, pp. 100-104, 1960/05/01 1960.

[11] G. I. Barenblatt, "The Mathematical Theory of Equilibrium Cracks in Brittle Fracture," in *Advances in Applied Mechanics*. vol. Volume 7, T. v. K. G. K. F. H. v. d. D. H.L. Dryden and L. Howarth, Eds., ed: Elsevier, 1962, pp. 55-129.

[12] X. P. Xu and A. Needleman, "Numerical simulations of fast crack-growth in brittle solids," *Journal of the Mechanics and Physics of Solids,* vol. 42, pp. 1397-&, Sep 1994.

[13] G. T. Camacho and M. Ortiz, "Computational modelling of impact damage in brittle materials," *International Journal of Solids and Structures,* vol. 33, pp. 2899-2938, 1996/08/01 1996.

[14] G. Alfano and M. A. Crisfield, "Finite element interface models for the delamination analysis of laminated composites: Mechanical and computational issues," *International Journal for Numerical Methods in Engineering,* vol. 50, pp. 1701-1736, Mar 2001.

[15] S. Li, M. D. Thouless, A. M. Waas, J. A. Schroeder, and P. D. Zavattieri, "Mixed-mode cohesive-zone models for fracture of an adhesively bonded polymer-matrix composite," *Engineering Fracture Mechanics,* vol. 73, pp. 64-78, Jan 2006.

[16] V. Tvergaard and J. W. Hutchinson, "The influence of plasticity on mixed mode interface toughness," *Journal of the Mechanics and Physics of Solids,* vol. 41, pp. 1119-1135, 1993/06/01 1993.

[17] J. Guzek, H. Azimi, and S. Suresh, "Fatigue crack propagation along polymer-metal interfaces in microelectronic packages," *IEEE Transactions on Components Packaging and Manufacturing Technology Part A,* vol. 20, pp. 496-504, Dec 1997.

[18] M. Manca, A. Quispitupa, C. Berggreen, and L. A. Carlsson, "Face/core debond fatigue crack growth characterization using the sandwich mixed mode bending specimen," *Composites Part a-Applied Science and Manufacturing,* vol. 43, pp. 2120-2127, Nov 2012.

[19] M. de Moura and J. P. M. Goncalves, "Cohesive zone model for high-cycle fatigue of adhesively bonded joints under mode I loading," *International Journal of Solids and Structures,* vol. 51, pp. 1123-1131, Mar 2014.

[20] M. de Moura and J. P. M. Goncalves, "Development of a cohesive zone model for fatigue/fracture characterization of composite bonded joints under mode II loading," *International Journal of Adhesion and Adhesives,* vol. 54, pp. 224-230, Oct 2014.

[21] K. L. Roe and T. Siegmund, "An irreversible cohesive zone model for interface fatigue crack growth simulation," *Engineering Fracture Mechanics,* vol. 70, pp. 209-232, Jan 2003.

[22] H. B. Chew, "Cohesive zone laws for fatigue crack growth: Numerical field projection of the micromechanical damage process in an elasto-plastic medium," *International Journal of Solids and Structures,* vol. 51, pp. 1410-1420, 3/15/ 2014.

[23] V. Sundararaman and S. K. Sitaraman, "Interfacial fracture toughness for delamination growth prediction in a novel peripheral away package," *IEEE Transactions on Components and Packaging Technologies,* vol. 24, pp. 265-270, Jun 2001.

[24] R. J. Harries and S. K. Sitaraman, "Numerical modeling of interfacial delamination propagation in a novel peripheral array package," *IEEE Transactions on Components and Packaging Technologies,* vol. 24, pp. 256-264, Jun 2001.

[25] W. D. Xie and S. K. Sitaraman, "Investigation of interfacial delamination of a copper-epoxy interface under monotonic and cyclic loading: Experimental characterization," *IEEE Transactions on Advanced Packaging,* vol. 26, pp. 447-452, Nov 2003.

[26] W. D. Xie and S. K. Sitaraman, "Investigation of interfacial, delamination of a copper-epoxy interface under monotonic and cyclic loading: Modeling and evaluation," *IEEE Transactions on Advanced Packaging,* vol. 26, pp. 441-446, Nov 2003.

[27] G. T. Ostrowicki, N. T. Fritz, R. I. Okereke, P. A. Kohl, and S. K. Sitaraman, "Domed and released thin-film construct—an approach for material characterization and compliant interconnects," *IEEE Transactions on Device and Materials Reliability,* vol. 12, pp. 15-23, 2012.

[28] G. T. Ostrowicki and S. K. Sitaraman, "Magnetically actuated peel test for thin films," *Thin Solid Films,* vol. 520, pp. 3987-3993, 3/30/ 2012.

[29] G. T. Ostrowicki, J. Williamson, V. Gupta, and S. P. Gurrum, "Thermal Cycling Reliability of Lead Free Solder Joints on Multi-Terminal Passive Components," presented at the ECTC, 2015.

[30] G. T. Ostrowicki and S. K. Sitaraman, "Cyclic magnetic actuation technique for thin film interfacial fatigue crack propagation," *Engineering Fracture Mechanics,* vol. 168, Part A, pp. 1-10, 12, 2016.

[31] H. T. Tran, M. H. Shirangi, X. Pang, and A. A. Volinsky, "Temperature, moisture and mode-mixity effects on copper leadframe/EMC interfacial fracture toughness," *International Journal of Fracture,* vol. 185, pp. 115-127, 2014.

[32] A. Kwatra, D. Samet, and S. K. Sitaraman, "Effect of thermal aging on cohesive zone models to study copper leadframe/mold compound interfacial delamination,"

in *Electronic Components and Technology Conference (ECTC) , 2015 IEEE 65th*, 2015, pp. 1531-1537.

[33] J. W. Hutchinson and Z. Suo, "Mixed Mode Cracking in Layered Materials," in *Advances in Applied Mechanics*. vol. Volume 29, W. H. John and Y. W. Theodore, Eds., ed: Elsevier, 1991, pp. 63-191.

[34] M. Charalambides, A. J. Kinloch, Y. Wang, and J. G. Williams, "On the analysis of mixed-mode failure," *International Journal of Fracture,* vol. 54, pp. 269-291, April 01 1992.

[35] A. Turon, J. Costa, P. P. Camanho, and C. G. Davila, "Simulation of delamination in composites under high-cycle fatigue," *Composites Part a-Applied Science and Manufacturing,* vol. 38, pp. 2270-2282, 2007.

[36] J. A. Pascoe, R. C. Alderliesten, and R. Benedictus, "Methods for the prediction of fatigue delamination growth in composites and adhesive bonds – A critical review," *Engineering Fracture Mechanics,* vol. 112–113, pp. 72-96, 11// 2013.

[37] W. E. R. Krieger, S. Raghavan, A. Kwatra, and S. K. Sitaraman, "Cohesive Zone Experiments for Copper/Mold Compound Delamination," presented at the ECTC, 2014.

[38] D. Samet, V. N. N. Trilochan Rambhatla, A. Kwatra, and S. K. Sitaraman, "A fatigue crack propagation model with resistance curve effects for an epoxy/copper interface," *Engineering Fracture Mechanics,* vol. 180, pp. 60-72, 2017.

[39] G. R. Irwin and J. A. Kies, "Critical Energy Release Rate Analysis of Fracture Strength," *Welding Journal, Research Supplement,* vol. 19, pp. 193-198, 1954.

[40] P. G. Charalambides, J. Lund, A. G. Evans, and R. M. McMeeking, "A test specimen for determining the fracture resistance of bimaterial interfaces," *Journal of Applied Mechanics-Transactions of the Asme,* vol. 56, pp. 77-82, Mar 1989.

[41] J. R. Rice, "A Path Independent Integral and the Approximate Analysis of Strain Concentration by Notches and Cracks," *J. Applied Mechanics,* vol. June, pp. 379-386, 1968.

[42] P. P. L. Matos, R. M. McMeeking, P. G. Charalambides, and M. D. Drory, "A method for calculating stress intensities in bimaterial fracture," *International Journal of Fracture,* vol. 40, pp. 235-254, 1989// 1989.

[43] G. Schlottig, "Reliability at the Chip Interfaces: Delaminating the Silicon Die from Molding Compound," Ph.D, MEchanics of Materials, Delft University of Technology, Delft, Netherlands, 2012.

[44] V. Mollón, J. Bonhomme, J. Viña, and A. Argüelles, "Theoretical and experimental analysis of carbon epoxy asymmetric dcb specimens to characterize mixed mode fracture toughness," *Polymer Testing,* vol. 29, pp. 766-770, 9// 2010.

[45] l. Sheng, M. Yuhai, and T. Y. Wu, "Bimaterial interfacial crack growth as a function of mode-mixity," *Components, Packaging, and Manufacturing Technology, Part A, IEEE Transactions on,* vol. 18, pp. 618-626, 1995.

[46] J. G. Williams, "Large Displacment and End Block Effects in the DCB Interlaminar Test in Mode-I and Mode-II," *Journal of Composite Materials,* vol. 21, pp. 330-347, Apr 1987.

[47] J. G. Williams, "End corrections for orthotropic DCB specimens," *Composites Science and Technology,* vol. 35, pp. 367-376, 1989.

[48] R. Olsson, "A simplified improved beam analysis of the DCB specimen," *Composites Science and Technology,* vol. 43, pp. 329-338, 1992/01/01 1992.

[49] M. M. Shokrieh, M. Heidari-Rarani, and M. R. Ayatollahi, "Interlaminar fracture toughness of unidirectional DCB specimens: A novel theoretical approach," *Polymer Testing,* vol. 31, pp. 68-75, 2 2012.

[50] M. M. Shokrieh, M. Heidari-Rarani, and M. R. Ayatollahi, "Delamination R-curve as a material property of unidirectional glass/epoxy composites," *Materials & Design,* vol. 34, pp. 211-218, 2 2012.

[51] W. E. R. Krieger, S. Raghavan, and S. K. Sitaraman, "Experiments for Obtaining Cohesive-Zone Parameters for Copper-Mold Compound Interfacial Delamination," *IEEE Transactions on Components, Packaging and Manufacturing Technology,* vol. 6, pp. 1389-1398, 2016.

[52] M. M. Abou-Hamda, M. M. Megahed, and M. M. I. Hammouda, "Fatigue crack growth in double cantilever beam specimen with an adhesive layer," *Engineering Fracture Mechanics,* vol. 60, pp. 605-614, Jul 1998.

[53] Z. Jiang, S. Wan, Z. Zhong, S. Li, and K. Shen, "Effect of curved delamination front on mode-I fracture toughness of adhesively bonded joints," *Engineering Fracture Mechanics,* vol. - 138, pp. - 91, 2015.

[54] C. T. Sun and S. Zheng, "Delamination Characteristics of Double-Cantilever Beam and End-Notched Flexure Composite Specimens," *Composites Science and Technology,* vol. 56, pp. 451 - 459, 1996.

[55] G. B. Murri, "Effect of data reduction and fiber-bridging on Mode I delamination characterization of unidirectional composites," *Journal of Composite Materials,* vol. 48, pp. 2413-2424, Aug 2014.

[56] R. Gutkin, M. L. Laffan, S. T. Pinho, P. Robinson, and P. T. Curtis, "Modelling the R-curve effect and its specimen-dependence," *International Journal of Solids and Structures,* vol. 48, pp. 1767-1777, 6/1/ 2011.

[57] M. V. Swain and L. R. F. Rose, "Strength Limitations of Transformation-Toughened Zirconia Alloys," *Journal of the American Ceramic Society,* vol. 69, pp. 511-518, 1986.

[58] P. J. Withers, "Fracture mechanics by three-dimensional crack-tip synchrotron X-ray microscopy," *Philosophical Transactions of the Royal Society A: Mathematical, Physical and Engineering Sciences,* vol. 373, 2015.

[59] A. G. Evans, M. Rühle, B. J. Dalgleish, and P. G. Charalambides, "The fracture energy of bimaterial interfaces," *Materials Science and Engineering: A,* vol. 126, pp. 53-64, 1990/06/15/ 1990.

[60] S. Maiti and P. H. Geubelle, "A cohesive model for fatigue failure of polymers," *Engineering Fracture Mechanics,* vol. 72, pp. 691-708, Mar 2005.

[61] M. de Moura and J. P. M. Goncalves, "Cohesive zone model for high-cycle fatigue of composite bonded joints under mixed-mode I plus II loading," *Engineering Fracture Mechanics,* vol. 140, pp. 31-42, May 2015.

[62] P. W. Harper and S. R. Hallett, "A fatigue degradation law for cohesive interface elements – Development and application to composite materials," *International Journal of Fatigue,* vol. 32, pp. 1774-1787, 11// 2010.

[63] C. Moriconi, G. Henaff, and D. Halm, "Cohesive zone modeling of fatigue crack propagation assisted by gaseous hydrogen in metals," *International Journal of Fatigue,* vol. 68, pp. 56-66, Nov 2014.

[64] S. Roth, G. Hutter, and M. Kuna, "Simulation of fatigue crack growth with a cyclic cohesive zone model," *International Journal of Fracture,* vol. 188, pp. 23-45, Jul 2014.

[65] S. Bhattacharya, I. V. Singh, B. K. Mishra, and T. Q. Bui, "Fatigue crack growth simulations of interfacial cracks in bi-layered FGMs using XFEM," *Computational Mechanics,* vol. 52, pp. 799-814, October 01 2013.

[66] K. Nasri and M. Zenasni, "Fatigue crack growth simulation in coated materials using X-FEM," *Comptes Rendus Mécanique,* vol. 345, pp. 271-280, 2017/04/01/ 2017.

[67] Z. Zhang and J. K. Shang, "Subcritical crack growth at bimaterial interfaces: Part III. shear-enhanced fatigue crack growth resistance at polymer/metal interface," *Metallurgical and Materials Transactions A,* vol. 27, p. 221, January 01 1996.

[68] D. Yao and J. K. Shang, "Effect of Load-Mix on Fatigue Crack Growth in 63Sn-37Pb Solder Joints," *Journal of Electronic Packaging,* vol. 119, pp. 114-118, 1997.

[69] D. Van Truong, V. Van Thanh, H. Hirakata, and T. Kitamura, "Interfacial fatigue fracture criterion of bimaterial in submicron scale," *Microelectronic Engineering,* vol. 140, pp. 23-28, 2015/06/01/ 2015.

[70] R. H. Rigby and M. H. Aliabadi, "Decomposition of the mixed-mode J-integral—revisited," *International Journal of Solids and Structures,* vol. 35, pp. 2073-2099, 6// 1998.

[71] D. Samet, A. Kwatra, and S. K. Sitaraman, "Cohesive Zone Parameters for a Cyclically Loaded Copper-Epoxy Molding Compound Interface," in *2016 IEEE 66th Electronic Components and Technology Conference (ECTC)*, 2016, pp. 1011-1018.

[72] S. Mahalingam, K. Goray, S. Tonapi, and S. K. Sitaraman, "Experimental characterization of monotonic and fatigue delamination of novel underfill materials," *Journal of Electronic Packaging,* vol. 128, pp. 405-411, Dec 2006.

[73] S. Mahalingam, A. Prabhakumar, S. Tonapi, and S. K. Sitaraman, "Theoretical Modeling and Prediction of Delamination in Flip Chip Assemblies With Nanofilled No-Flow Underfill Materials," *Journal of Electronic Packaging,* vol. 130, Dec 2008.

[74] A. A. O. Tay, Y. Ma, and S. H. Ong, "Failure of polymer-metal interfaces under hygrothermal loading," in *Design, Test, Integration, and Packaging of Mems/Moems, Proceedings*. vol. 4019, B. Courtois, S. B. Crary, K. J. Gabriel, J. M. Karam, K. Markus, and A. A. O. Tay, Eds., ed Bellingham: Spie-Int Soc Optical Engineering, 2000, pp. 471-481.

[75] W. K. Lam, T. S. Yeung, A. Teng, and M. M. F. Yuen, "A method for evaluating delamination between epoxy moulding compounds and different plated leadframes," in *Electronic Materials and Packaging, 2000. (EMAP 2000). International Symposium on*, 2000, pp. 214-219.

[76] L. Durix, M. Dreßler, D. Coutellier, and B. Wunderle, "On the development of a modified button shear specimen to characterize the mixed mode delamination toughness," *Engineering Fracture Mechanics,* vol. 84, pp. 25-40, 4// 2012.

[77] S. Raghavan, I. Schmadlak, G. Leal, and S. K. Sitaraman, "Framework to extract cohesive zone parameters using double cantilever beam and four-point bend fracture tests," in *Thermal, mechanical and multi-physics simulation and experiments in microelectronics and microsystems (eurosime), 2014 15th international conference on*, 2014, pp. 1-5.

[78] S. Raghavan, I. Schmadlak, G. Leal, and S. K. Sitaraman, "Mixed-mode cohesive zone parameters for sub-micron scale stacked layers to predict microelectronic device reliability," *Engineering Fracture Mechanics*, vol. 153, pp. 259-277, 3// 2016.

[79] D. Samet, A. Kwatra, and S. K. Sitaraman, "A Compliance-Based Approach to Study Fatigue Crack Propagation for a Copper-Epoxy Interface," in *ASME 2015 International Technical Conference and Exhibition on Packaging and Integration of Electronic and Photonic Microsystems collocated with the ASME 2015 13th International Conference on Nanochannels, Microchannels, and Minichannels*, 2015, pp. V002T01A012-V002T01A012.